Alma Mater Studiorum – Università di Bologna
in cotutela con Università Gustave Eiffel

DOTTORATO DI RICERCA IN

Ingegneria Elettronica, Telecomunicazioni e Tecnologie dell'Informazione

Ciclo XXXV

Settore Concorsuale: 09/F1 – Campi Elettromagnetici

Settore Scientifico Disciplinare: ING-INF/02 – Campi Elettromagnetici

Efficient Wireless Coverage of In-Building Environments with Low Electromagnetic Impact

Presentata da: Andrea Giovannini

Coordinatore Dottorato
Prof. Ing. Aldo Romani

Supervisore
Prof. Ing. Giovanni Tartarini

Supervisore
Prof. Ing. Jean-Marc Laheurte

Co-supervisore
Prof. Ing. Jean-Luc Polleux

Co-supervisore
Prof. Ing. Diego Masotti

Co-supervisore
Prof. Ing. Anne-Laure Billabert

Esame finale anno 2023

University of Bologna

ETIT Ph.D.

Electronics, Telecommunications and Information Technologies Engineering

Université Gustave Eiffel

École Doctorale MSTIC

Mathématiques, sciences et Technologies de l'Information et de la Communication

A joint Ph.D. Thesis between
University of Bologna and Université Gustave Eiffel:

Efficient Wireless Coverage of In-Building Environments with Low Electromagnetic Impact

Andrea GIOVANNINI

Thesis Directors:	Pr. Giovanni TARTARINI	DEI, University of Bologna (Italy)
	Pr. Jean-Marc LAHEURTE	ESYCOM-CNRS, Université Gustave Eiffel (France)
Thesis Supervisors:	Pr. Jean-Luc POLLEUX	ESYCOM-CNRS, Université Gustave Eiffel (France)
	Pr. Anne-Laure BILLABERT	ESYCOM-CNRS, UMR 9007 Le CNAM (France)
	Pr. Diego MASOTTI	DEI, University of Bologna (Italy)

Members of the JURY

Reviewers:	Pr. Angélique RISSONS	ISAE, Toulouse (France)
	Pr. Lorenzo POLI	University of Trento (Italy)
Examiners:	Pr. Stavros IEZEKIEL	University of Cyprus (Cyprus)
	Dr. Pierluigi DEBERNARDI	IEIIT, CNR (Italy)
	Pr. Gaetano BELLANCA	University of Ferrara (Italy)

Summary

List of Figures

List of Tables

Glossary

AC: Alternate Current

ADS: Advanced Design Systems (software by Keysight)

AF: Array Factor

ASF: Augmented Scalarization Function

BB-RoF: Baseband-over-Fiber

BiCMOS: Bipolar Complementary Metal-Oxide-Semiconductor

CMOS: Complementary Metal-Oxide-Semiconductor

DC: Direct Current

DFB: Distributed Feed-Back

DUT: Device Under Test

EEL: Edge Emitting Laser

ESYCOM: laboratoire d'Electronique, Systèmes de Communication et Microsystèmes (laboratory of Electronics, Communication Systems and Microsystems)

GND: Ground

GSG: Ground-Signal-Ground

HBT: Heterojunction Bipolar Transistor

HPT: Heterojunction Phototransistor

HS-HBT: High Speed Heterojunction Bipolar Transistor

HS-HPT: High Speed Heterojunction Phototransistor

HV-HBT: High Voltage Heterojunction Bipolar Transistor

HV-HPT: High Voltage Heterojunction Phototransistor

IBM: International Business Machines Corporation

iDAS: indoor Distributed Antenna System

IF: Intermediate Frequency

IF-RoF: Intermediate Frequency-over.Fiber

IIP_3: Input 3rd order Intercept Point

IMD_3: 3rd order Intermodulation Distortion

IP_3: 3rd order Intercept Point

IP_{1dB}: Input 1 dB compression Point

JLT: Journal of Lightwave Technology

LABSTICC: Laboratoire de Science et Techniques de l'Information, de la Communication et de la Connaissance (Laboratory of Information Science and Techniques, Communication and Knowledge)

LAN: Local Area Network

LIV: Light-Current-Voltage

MCDM: Multi Criteria Decision Making

MEXTRAM: Most Exquisite Transistor Model

MIMO: Multiple Input Multiple Output

MRD: Maximum Radiation Direction

NEP: Noise Equivalent Power

NL: Non-Linear

NSGA-II: Non-Dominated Sorting Genetic Algorithm 2

OM: Opto-Microwave

OOR: On-Off Ratio

ORIGIN: Optical Radio Infrastructure for Gigabit/s Indoor Network

OSA: Optical Spectrum Analyser

PCB: Printed Circuit Board

PD: Photodiode

PIN: Positive, Intrinsic, Negative

P_{1dB}: 1 dB compression Point

RF: Radio Frequency

RF-RoF: Radio Frequency-over-Fiber

RIN: Relative Intensity Noise

RoF: Radio-over-Fiber

SA: Spectrum Analyser

SCR: Space Charge Region

SG : Signal Generator

SIC: Selectively Collector Implantation

SM: Single Mode

SMA: SubMiniature version A connector

SNR: Signal to Noise Ratio

SOI: Silicon On Insulator

TDK: Tōkyō Denki Kagaku Kōgyō

TIA: Trans-Impedance Amplifier

TMA: Time Modulated Array

TRoF: Radio-over-Fiber Transceiver

TSMC: Taiwan Semiconductor Manufacturing Company

VCSEL: Vertical Cavity Surface Emitting Laser

VNA: Vector Network Analyser

WiFi: Wireless Fidelity protocol

3T: 3 Terminals

4G: 4^{th} Generation network

5G: 5^{th} Generation network

Chapter 1: Introduction

1.1. Context

The objective of this project is to combine Radio-over-Fiber (RoF) and Time Modulated Array (TMA) technologies in a single system to distribute RF signals in indoor environments. RoF is already widely used in the distribution of signals thanks to the advantages of the optical fiber over copper wires and other types of connections. In particular, the costs, easiness of deployment and high data-rates made RoF ideal for indoor applications such as indoor Distributed Antenna Systems (iDAS) [1]-[4], radioastronomy [5]-[13] and the distribution of mobile radio signals (RoF) [14]-[16]. In addition, using Vertical Cavity Surface Emitting Lasers (VCSELs) in the RoF links would furtherly improve the system thanks to the lower costs and to the better coupling characteristics of such devices. On the other hand, TMA and beamforming techniques in general allow to transmit signals only in the necessary directions and, more importantly, to adapt dynamically the transmission to the situation. Suppose to have a space which is uniformly crowded during a certain period of time, while at a different time the same space presents people gathering in specific places. In the first scenario, to guarantee coverage for everyone it would be necessary to radiate uniformly in all directions, while in the second scenario it is sufficient to transmit only in specific directions. A beamforming system is capable of adapting to different situations like the one just described while guaranteeing the same quality of service in both situations. Beamforming systems optimize the use of power, avoiding power waste and reducing the overall amount of radiation, thus leading to healthier environments in terms of radiation [17], [18]. The choice of TMA as the beamforming technique to be implemented is determined mainly by the costs and simplicity of such solution. Since it is based on the periodic On-Off switching of the antenna elements, the TMA cost relies mainly on the cost of the switching elements, which are normally cheap and easily available.

We propose to combine RoF and TMA to create a novel and low-cost system to face the challenges related to near-future and future networks. For instance, 5G networks are limited in the penetration of in-building environments at mm wave frequencies (i.e. beyond 30 GHz) [19]-[21]. A solution is the installation of systems spreading RF signals in such environments, equipped with beamforming antennas to ensure adaptation to the obstacles which could be present. The use of optical fiber ensures also a “future-proof” system, in the sense that optical fiber’s capacity and data-rates are so high that the same system is much likely to be used also in next generation networks. The applications we foresee for this system are mainly related to the distribution of RF signals in in-building environments. This includes for example WiFi signals, 4G and 5G signals, iDAS applications and Local Area Networks (LANs). The focus on keeping the system’s costs low is reflected also on the choices of the laser source and of the photodetector material. VCSELs’ fabrication process allows them to have a lower cost compared to other solutions. Regarding the photodetector, we chose to focus on SiGe for its compatibility with CMOS technology and lower cost, since it is a technology based on Si wafers.

Fig. 1.1 represents a block scheme of the system envisaged within the project. The RF signal related to the target application is brought inside a building, where is sent to the different areas to be covered by a RoF link. The RoF link internal structure is also summarized for clarity and is explained more in detail in chapter 3. In particular, any RoF link is composed of a light source converting the signal from electrical to optical, an optical fiber transporting the signal and a photodetector converting back the signal to electrical. The RF signal is then distributed to the users inside the building by a beamforming antenna system block. The beamforming array allows to cover specific areas corresponding to the location of the final users, thus optimizing the radiated power.

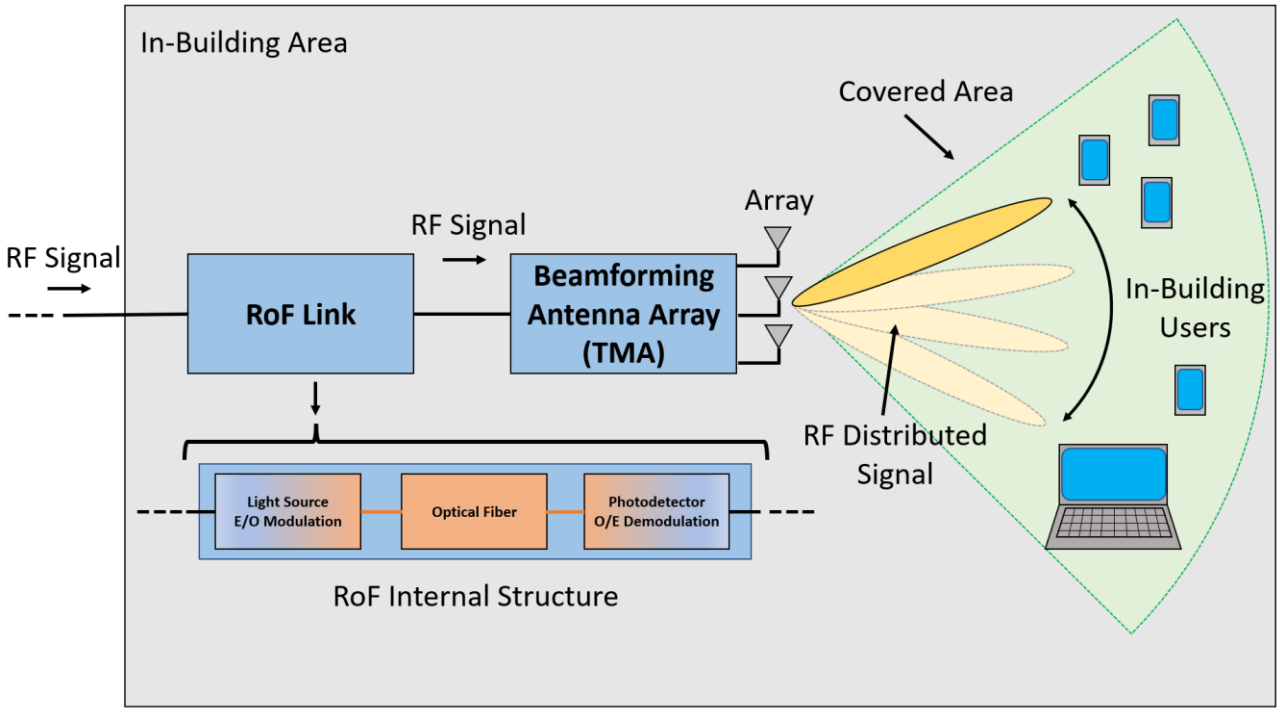

Fig. 1.1: Block scheme of the PhD project representing the proposed RoF-TMA system.

1.2. Thesis structure

The present PhD thesis is organised in the following structure:

- Chapter 1 presents the context of this PhD thesis and describes the structure of the document.
- Chapter 2 gives a state of the art on TMAs and RoF systems. The first part focuses on the evolution and applications of TMAs. The second part starts with an overview on optical fiber's advantages and RoF links. Then, a detailed description of the RoF link's main figures of merit is given and finally the chapter gives the state of the art of the single components of a RoF link, focusing in particular on Vertical Cavity Surface Emitting Lasers (VCSELs) and photodetecting devices.
- Chapter 3 focuses on TMAs. Firstly, TMA systems theory is explained in detail and the core concept of combining RoF and TMA in a single system is shown, followed by an experimental validation of the proposed RoF-TMA system. Then, the analysis of the effects of unwanted phase shifts on the system is presented and demonstrated

through measurements. Finally, an optimization algorithm aiming at determining the modulating sequences of TMA and mitigating the effects of phase shifts is presented.

- Chapter 4 describes the modelling of RoF links, focusing on lasers and heterojunction phototransistors (HPTs). The chapter starts recalling the RoF link model used to present its main figures of merit. It follows a presentation of a behavioural model aimed at modelling with precision the behaviour and main non linearities of lasers and is validated through simulations. Finally, an analysis of the HPT behaviour as a switching component in TMA systems, resulting in the definition of the requirements that the HPT must satisfy to be employed in a TMA.
- Chapter 5 describes the steps taken in the design, fabrication, characterization and packaging of HPTs. The chapter starts with an explanation of the design rules that needed to be followed in the realization of the HPTs' chip. Then, the chapter shows the set-ups and results of the characterization of the HPTs in both frequency and time domains. Finally, a description of the packaging of the HPT is given. This last part focuses on the design of a PCB with an integrated bias-tee that will host the HPT. The chapter ends with perspectives on the measurements and characterizations of the RoF-TMA system prototype that will employ the packaged HPT.
- Chapter 6 presents the conclusions and perspectives of this PhD thesis.

Chapter 2: State of the art

2.1. Introduction

This chapter presents the state of the art of Time Modulated Array (TMA) and Radio-over-Fiber (RoF) systems. The first part defines TMAs and focuses on their evolution, applications and challenges related to this kind of systems. The second part presents and defines RoF systems in terms of their composition, main applications and motivations behind their use in this project, with also a minor focus on the technological development of this technology. This is followed by the definition of the RoF link model in which every component is identified with an equivalent electrical quadrupole. This is important as quantities defined for purely electrical components, such as the gain, cannot be blindly attributed to electro-optical components. Further sections dedicated to lasers and photodetectors follow, focusing especially on Vertical Cavity Surface Emitting Lasers (VCSELs) and Heterojunction Phototransitors (HPT), which are the components we wish to use for this PhD project.

We highlight that our research on RoF for radioastronomy applications led to the following publications: [5]-[13].

2.2. Time Modulated Arrays

At present, beamforming and beamsteering antenna systems are gaining increasing interest due to their ability to redirect dynamically the radiating lobes in a desired direction. In the very first attempts at controlling the direction of radiation, antennas were steered mechanically and repositioned to obtain different interference patterns. However, this solution is expensive, slower compared to other techniques and requires higher maintenance, especially for the moving parts. Especially in RF communications, mechanical steering was soon abandoned in favour of beamforming based solutions. The basic principle behind beamforming is to change the phase of each antenna current in order to control the constructive and destructive interference between the radiating elements. One simple technique is the Phased Array [22]-[24], in which a phase shifter is added before each antenna and controlled externally, as in Fig. 2.1. Although very simple, this solution is rather costly due to the need of a high number of phase shifters and of their calibration, which often consists in a nonlinear map bias vs. phase shift. This is one of the main reasons why research looked for cheaper and effective solutions, such as the TMA. TMAs are also called four-dimensional arrays, as they introduce time as an additional dimension for the generation of radiation patterns.

A TMA is an antenna array where each antenna is periodically switched On and Off. The switching produces a modulation of the antenna currents that allows to change and control the radiation pattern emitted by the array. At the same time, the array emits at several frequencies rather than only at the carrier frequency. The details on the theory behind TMAs is given in Chapter 3. The TMA main advantages are its low cost and easy implementation due to the use of simple switches or square wave modulators in place of the phase shifter of a Phased Array, and the unique capability to radiate at an almost infinite number of close frequencies, produced by the combination of the carrier frequency with the (smaller) frequency adopted for the periodic switching. TMAs were first studied for beam scanning in

radars [25] and in all their early applications, TMAs' multiple frequency radiation was considered an undesired feature. Therefore, subsequent research works focused mainly on Sideband Radiation Suppression [26]- [31], reaching values of Sidelobe Radiation levels below -20 dB and also Sidelobe Ratios below -30 dB. With the evolution of communication systems, the multiple frequency radiation property of TMAs started to be exploited rather than suppressed. Some applications exploiting this include Adaptive Nulling [32], Harmonic Beamforming and Beamsteering [33]-[39], Direction Finding [40], [41], Wireless Power Transfer [45]-[48], MIMO [49]-[51] and wireless communication [52]-[54].

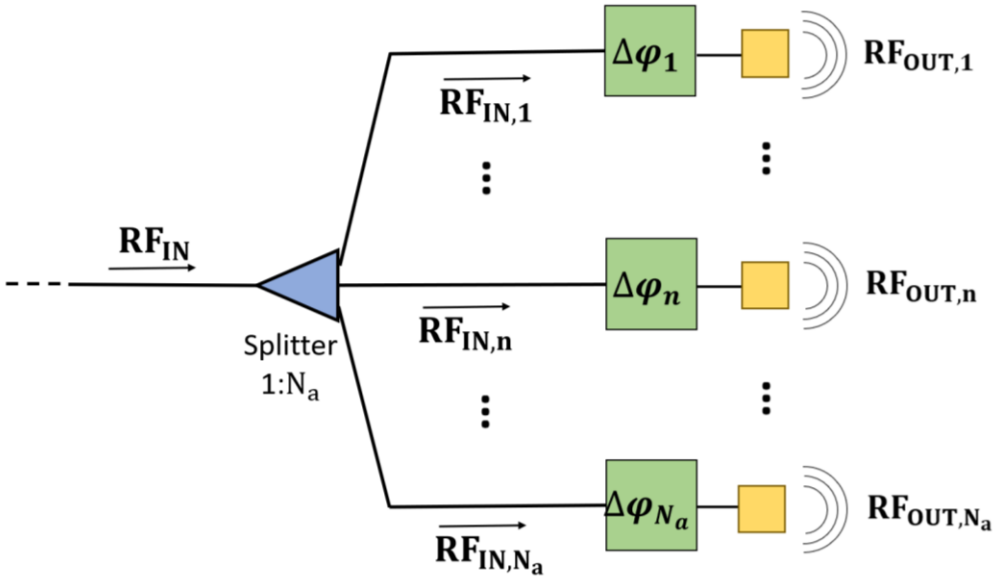

Fig. 2.1: Phased array system employing phase shifters.

The main drawback of the TMA is power efficiency, due to the switching. In fact, the available power is spread between the radiating frequencies or also wasted when the antennas are completely switched off. To overcome this issue, multiple solutions were proposed, as in [59], where two complementary arrays of antennas are modulated with a symmetric square wave, thus exchanging the role of On and Off states for the two complementary switching patterns. Furthermore, great improvements have been achieved by employing optimization algorithms in the definition of the driving sequences of the switches. This includes evolutionary algorithms such as differential evolution [60], simulated annealing [61], genetic algorithms [62] and particle swarm optimization [63].

2.3. Radio over Fiber systems

A RoF system has the purpose of transmitting radio RF signals through an optical fiber. The optical fiber offers many advantages compared to copper wires or other guides:

- Low cost: optical fibers are mainly made from silica, which is a very common and cheap material.
- Low attenuation: electromagnetic fields propagating through an optical fiber experience very low attenuation, in the order of 0.2 dB/km at a 1500 nm wavelength.
- Size: optical fibers are much lighter in weight and thinner, with their 125 μm diameter, compared to copper wire. This allows them to be easy to install and valuable for

connections in aircraft, spacecraft and other applications where the weight of the structure plays an important role.

- Electromagnetic interference: optical fibers are naturally immune to electromagnetic interference. This nullifies the cross-talk interference between transmission lines and allows the fiber to be used in environments characterized by the presence of strong electromagnetic fields.
- Future proof: optical fibers have very high capacity and present networks' data-rate requirements are largely met by them. So it is expected that near-future networks' data-rate requirements will be met as well by optical fibers.

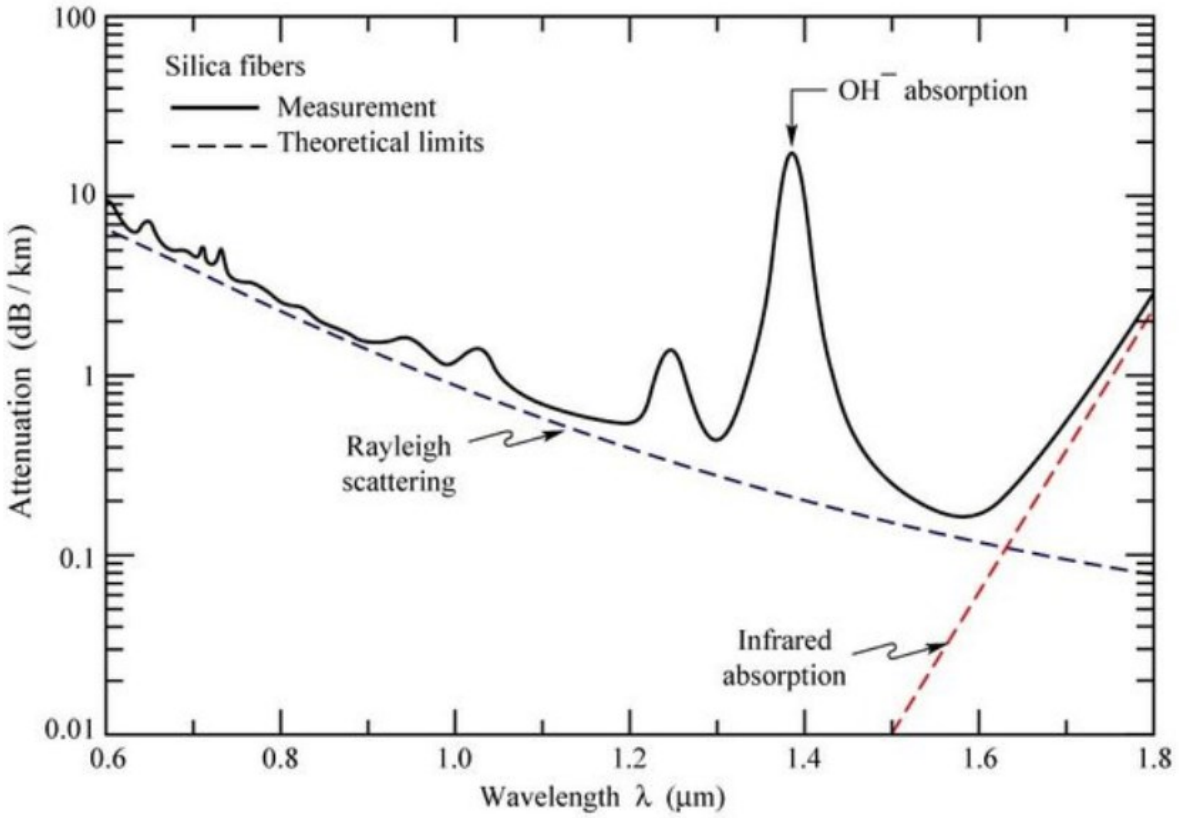

Fig. 2.2: Attenuation spectrum of optical fibers (continuous) with OH ions absorption peaks highlighted. Dashed lines are Rayleigh scattering(black) and infrared absorption (red).

Fig. 2.2 shows the attenuation spectrum of optical fibers, highlighting the main sources of attenuation: infrared absorption and Rayleigh scattering. Infrared absorption is related to the intrinsic characteristics of the material, in this case silica, and is caused by vibrational resonance. Extrinsic absorption (i.e. the OH ions peaks in the curve) is due to impurities present in the silica. The main residuals that cause attenuation peaks are water vapours that remain trapped in silica during its processing. A vibrational resonance of the OH ion occurs near 2.73 μm. Its harmonic and combination tones with silica produce absorption at the 1.39 μm, 1.24 μm and 0.95 μm wavelengths. The spectral peaks seen in the absorption spectrum of the fiber occur near these wavelengths and are due to the presence of residual water vapour in silica. There exist also fabrication processes capable of removing the majority of water vapours inside silica, leading to the so-called dry fibers.

Finally, Rayleigh scattering is a loss mechanism caused by density fluctuations in the fiber. Since silica is an amorphous material, when it solidifies after being molten it does not have a homogenous lattice, but rather an inhomogeneous structure. This leads to the formation of microscopic zones, or particles, with different density, causing small variations in the index of refraction of material and subsequently causing a loss. The entity of Rayleigh backscattering does not depend on the material but depends only on the dimensions of the particles relative to the wavelength. Therefore, smaller wavelengths are associated with a higher Rayleigh scattering loss. The absorption spectrum of optical fibers allows to isolate different transmitting wavelength windows, located respectively around 850 nm, 1310 nm and 1550 nm.

Fig. 2.3 shows the working principle of RoF: an RF signal modulates a light emitting source, usually a laser, which is coupled to the optical fiber. Finally, a photodetector coupled to the other end of the fiber demodulates the RF signal contained in the envelope of the impinging light signal.

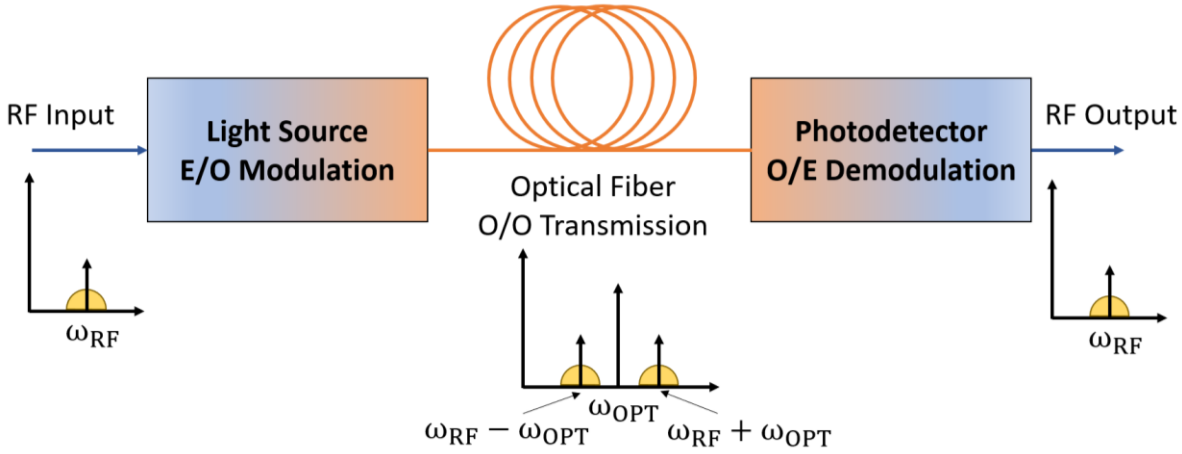

Fig. 2.3: Schematic of a RoF link. An RF input signal modulates a light source which converts the signal from electrical to optical. The signal is transmitted through the optical fiber and converted back to an electrical signal by a photodetector.

RoF is subdivided into three categories:

- RF-over-Fiber (RF-RoF): the RF signal directly modulates the light source, without the need of up and down conversion circuits. This kind of RoF link offers a simple architecture but requires faster light sources and photodetectors as the frequency increases, increasing the cost of the link.
- IF-over-Fiber (IF-RoF): the RF signal is first transposed to an Intermediate Frequency (IF) before modulating the light source. This system is more relaxed in terms of optoelectronic components' speed, but the architecture is more complex in turn.
- Baseband-over-Fiber (BB-RoF): the baseband radio signal is transmitted as it is through the fiber and upconverted to RF frequency at the end.

The next subsection describes how the principal opto-microwave (OM) figures of merit are defined for a RoF link, followed by two dedicated subsections to VCSEL lasers and HPT photodetectors.

2.4. Figures of Merit in a RoF link

Defining the figures of merit of optoelectronic devices is necessary but not as easy as it seems. In fact, there exist multiple ways to define them and therefore there is not a universal convention. Purely electric devices are defined by their electrical ports so that the device itself is treated as a black box and its behaviour is defined by a transfer function linking input and output ports. For optoelectronic devices, which include all the elements of a RoF link (light sources, optical fibers and photodetectors), the main issue is the impossibility to define ports on the "optical side" of these devices. This is a problem common also to waveguides for which the definition of port can be extended, but not without complications. The aim is to define equivalent RF two-ports representing the optoelectronic devices. In this way, it would be possible to model a RoF system as a cascade of two-port networks and to implement optoelectronic blocks in simulation programs such as Keysight ADS. The model we apply was developed by the ESYCOM team, shown in the works [64]-[69] and took inspiration from previous works such as [70]-[75].

The first step is to consider that the modulated optical signal has the RF information component encapsulated in its envelope. Therefore, if the modulated optical signal is received by an ideal photodiode with unitary responsivity (i.e. 1 A/W) we would obtain an electrical current equivalent to the initial RF signal. We call this current I_{opt} (equivalent optical current of the optoelectronic device) and define it as

$$I_{opt} = \alpha_C P_{opt} = 1\ {}^{A}/_{W}\, P_{opt} \tag{2.1}$$

where α_C is the conversion coefficient of the optical power P_{opt} to the equivalent optical current I_{opt}. This means that the optical power is represented by the output current of an ideal photodiode with responsivity 1 A/W. The next step is to define the opto-microwave (OM) power P_{OM} to later define the figures of merit of the optoelectronic device. P_{OM} is defined as the power generated by a virtual probe, which is a theoretical photodiode with responsivity $\mathcal{R}_{pd,probe} = 1$ A/W connected to a 50 Ω load. To be noted that the photodiode of the virtual probe is different from the photodiode related to the definition of I_{opt}, as the latter was mentioned as a parallelism to introduce the conversion factor α_C. So the OM power is defined as

$$P_{OM} = \frac{1}{2} R_0 I_{opt}^2 = \frac{1}{2} R_0 \left(\frac{\alpha_C P_{opt}}{\mathcal{R}_{pd,probe}} \right)^2 = \frac{1}{2} R_0 P_{opt}^2 \left(\frac{\alpha_C}{\mathcal{R}_{pd,probe}} \right)^2 \tag{2.2}$$

This expression is general and can be used regardless of the values of $\mathcal{R}_{pd,probe}$ and α_C. However, in our case it is $\mathcal{R}_{pd,probe} = \alpha_C = 1$ A/W. Fig. 2.4 shows a representation of the equivalent two-ports composing a RoF link. While the laser's input port and the photodiode's output port are conventional electrical ports, all the other ports are equivalent optical ports defined with our convention. For instance, the laser's output port is substituted by a current generator with internal load R_0 (50 Ω) providing the equivalent optical current I_{opt} feeding a matched load R_0 in the optical fiber's input port.

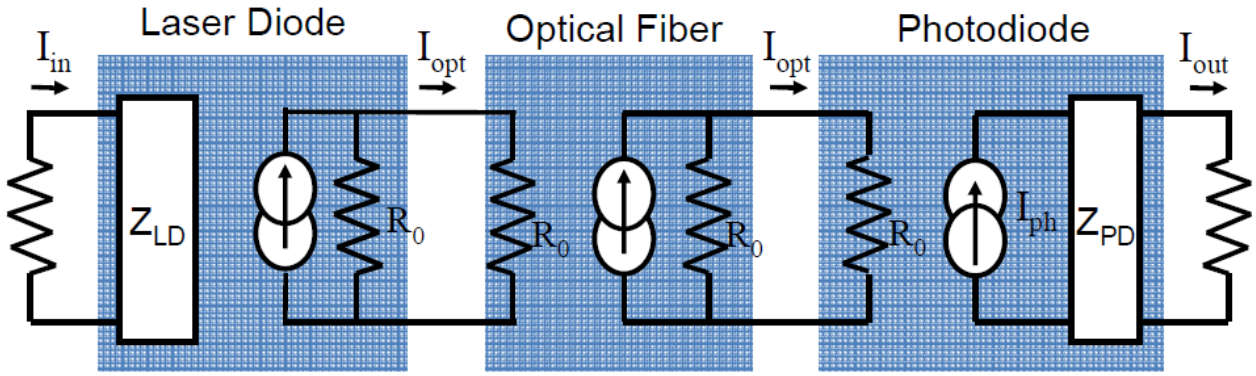

Fig. 2.4: RoF link equivalent two-port network.

The following step is to define the OM gain and noise figures of merit for each element of a RoF link. Starting from the photodiode, the OM gain is defined as the ratio between the output electrical power and the equivalent OM power. The photodiode impedance Z_{PD} is considered equal to R_0.

$$G_{PD}^{OM} = \frac{\frac{1}{2}R_0 I_{out}^2}{\frac{1}{2}R_0 I_{opt}^2} = \left(\frac{I_{out}}{\alpha_C P_{opt}}\right)^2 = |S_{21}^{OM}|^2 = \left(\frac{\mathcal{R}_{PD}}{\alpha_C}\right)^2 = \mathcal{R}_{PD}^2 \tag{2.3}$$

where $\mathcal{R}_{PD}$ is the photodiode's responsivity. A symmetrical reasoning applied to the laser and considering Z_{LD} to be 50 Ω yields an OM gain

$$G_{LD}^{OM} = |S_{21}^{OM}|^2 = \left(\frac{S_{LD}}{\alpha_C}\right)^2 = S_{LD}^2 \tag{2.4}$$

with S_{LD} being the laser's slope efficiency. Regarding the optical fiber, we consider A_{FB} as the related optical losses with the attenuation on the RoF signal included due to modal and/or chromatic dispersion [74]. In this thesis the employed fibers are short enough to be considered as linear attenuators. Although the linear losses of the fiber can be modelled with an equivalent impedance, the presented block model is more general. In particular, it allows to take into account the non-linearities of the fiber and model them through the generator of the output port. In addition, the structure of the blocks is the same for each component and allows an easier implementation on simulation programs. The final OM gain of the whole RoF link results to be:

$$G_{LINK}^{OM} = (S_{LD} A_{FB} \mathcal{R}_{PD})^2 \tag{2.5}$$

and we recall that both the laser and the photodiode are matched to 50 Ω. The proposed modelling of the RoF components gain aims at keeping the definition of gain between homogeneous quantities and to maintain the fact that the optical beams envelope behaves as a current.

For completeness, we also define the noise figures of merit related to the optoelectronic components of the link. The laser and photodiode noise factor can be determined by typical signal to noise ratio (SNR) between the OM input and the OM output power:

$$F_{LD,PD}^{OM} = \frac{SNR_{in}^{OM}}{SNR_{out}^{OM}} = 1 + \frac{N_{LD,PD}^{OM}}{G_{LD,PD}^{OM} kT} \tag{2.6}$$

where $N_{LD,PD}^{OM}$ is the OM noise spectral power density of the laser or the photodiode, k is the Boltzmann's constant and T is the temperature in Kelvins. The laser's main noise source is related to its Relative Intensity Noise (RIN), which is defined as the ratio between the power spectral density of the optical intensity fluctuations and the average intensity emitted by the laser. RIN is frequency dependent (i.e. not white) and its measurements are always referred to a certain noise bandwidth B_N, be it finite or normalized to 1 Hz. Thus we define the N_{LD}^{OM} of the laser as:

$$N_{LD}^{OM} = \langle I_{opt} \rangle^2 R_L = \langle \alpha_C P_{opt} \rangle^2 R_L = \left(\alpha_C \overline{P_{opt}}\right)^2 RIN\ R_L \tag{2.7}$$

where $\langle \cdot \rangle$ denotes the power spectral density operator, R_L is the load resistor and P_{opt} is the time varying power due to intensity noise. $\overline{P_{opt}}$ is the average power emitted by the laser. Therefore, the laser's OM noise factor becomes:

$$F_{LD}^{OM} = 1 + \frac{\left(\alpha_C \overline{P_{opt}}\right)^2 RIN\ R_L}{G_{LD}^{OM} kT} \tag{2.8}$$

Concerning the photodiode, its main noise sources are the shot noise, produced by the quantum nature of the received photons and dependent on the incident power, and the thermal noise, power independent and constant in frequency. The thermal noise of a photodiode is usually defined by the Noise Equivalent Power (NEP) which is defined as the optical input power needed to produce an additional output power identical to that noise and is given by:

$$NEP = \frac{1}{\mathcal{R}_{PD}} \sqrt{B_N \frac{N_{TH\_PD}}{R_L}} \tag{2.9}$$

where $\mathcal{R}_{PD}$ is the photodiode's responsivity, B_N is the noise bandwidth R_L is the photodiode's load and N_{TH_PD} is the photodiode's thermal noise. Considering both noise sources (i.e. NEP and shot noise), the photodiode's OM noise factor becomes:

$$F_{PD}^{OM} = 1 + \frac{2qI_{ph}R_L + (NEP\ \mathcal{R}_{PD})^2 R_L}{G_{PD}^{OM} kT} \tag{2.10}$$

with q being the elementary charge and I_{ph} being the DC photocurrent generated by the photodiode. With this the model of the RoF link is complete and exploitable for simulations.

2.5. Vertical Cavity Surface Emitting Lasers

Vertical Cavity Surface Emitting Lasers (VCSELs) were firstly introduced in 1978 as a new class of monolithically fabricated semiconductor based lasers and at present are gaining importance in applications such as data centres and Local Area Networks (LAN) links. What distinguishes VCSEL from the other lasers, in particular from the Edge Emitting Lasers (EEL) is their design. VCSELs are fabricated so that their optical aperture develops vertically instead

of horizontally. This allows to test the lasers directly on the wafer at early stages of fabrication, while EEL need to be cut before being tested. The structure of most VCSELs consists of a thin quantum well active layer between two parallel reflectors with high reflectivity (higher than 99.9%). The p-doped and n-doped layers around the active layer have Bragg reflectors to have single frequency emission. The structure and cross section of a typical VCSEL is shown in Fig. 2.5. The thin active layer and small volume of the cavity of VCSELs do not allow them to reach high output powers compared to EELs, however they are advantageous due to the low power consumption, single mode (SM) operation and high optical efficiency. Other than on-wafer testability, VCSELs have also a small footprint, allowing for a denser wafer integration. Their good optical efficiency is due to the circular and low divergent shape of the cavity, which allows a better coupling and an easier alignment and packaging into the optical fiber.

At present, GaAlAs/GaAs surface-emitting lasers emitting in the near-infrared-red band, including 850 nm, are available on the market, with modulation bandwidths greater than 28 GHz [76], [77]. State of the art VCSELs for operation at 980 nm and attaining a modulation bandwidth up to 37 GHz have been manufactured and tested [78]. The emission wavelengths of VCSELs are not only limited by the values mentioned before. Wavelengths range from shorter values such as 650, 750, 850, 980 and 1100 nm to longer values such as 1300 and 1550 nm. However, the technology complexity and the fabrication costs of VCSELs increase with the wavelength. State of the art VCSELs operating at 1550 nm achieved modulation bandwidth up to 17 GHz [79], [80]. Therefore, VCSELs operating at shorter wavelengths have lower costs and are the more interesting in the perspective of realizing a low cost system.

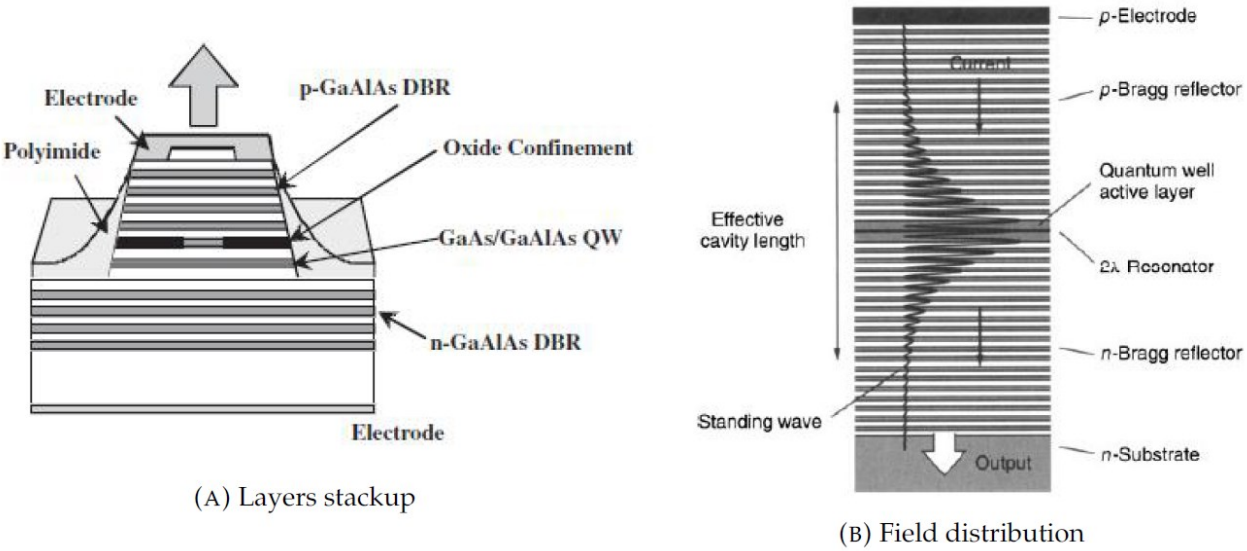

(A) Layers stackup

(B) Field distribution

Fig. 2.5: Cross-section of a typical 850 nm GaAs based VCSEL along with the field distribution in the structure due to the Bragg reflectors [81].

2.6. Photodetecting devices

2.6.1. General characteristics

An important aspect of this project is the photodetector. In the perspective of realizing a RF-RoF link without up or down conversion, the photodetector must be fast enough to detect RF signals in the GHz order or even beyond. In particular, we mainly made use of two photodetectors: p-i-n photodiodes and SiGe heterojunction phototransistors (HPT). To give a general knowledge of the materials employed for photodetectors, we can categorize semiconductors based on the wavelength and application of the system [65], as summarized in Tab. 2.1 and Fig. 2.6.

Application	Material	Characteristics
Long-haul communication systems at 1550 nm	InGaAs	Grown on InP substrate
	AlGaSb	Grown on GaSb substrate, less competitive compared to InP
LAN communication at 1550 nm	AlGaAs	Mature technology, low cost, compatible with AlGaAs lasers, excellent substrate availability
	Si	Mature technology, low cost, excellent substrate availability
LAN and long haul detectors	Si-based	Wavelength range: 400 nm up to 1000 nm
	Ge-based	Wavelength range: 400 nm up to 1550 nm. Mature technology at a medium cost, good substrate availability
	SiGe	Possibility to build high-speed photodetectors integrated with Si-based infrastructures, with higher range compared to pure Si. The 3dB bandwidth can reach values up to 15 GHz for surface illuminated photodetectors [65].

Tab. 2.1: Most common semiconductors employed for photodetectors for the listed applications.

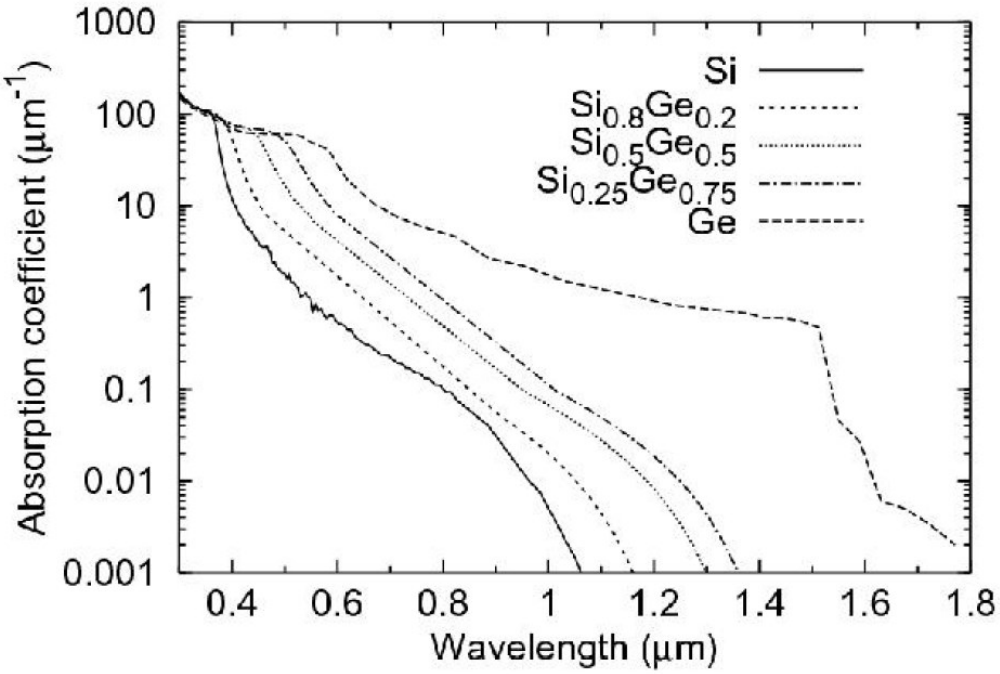

Fig. 2.6: Comparison between the absorption spectrum of Silicon, Germanium and compound materials [82].

At present, a lot of effort is being directed into development of high speed and high efficiency photodetectors based on Silicon, due to its abundance and the level of maturity of the correspondent fabrication technology. This would allow low cost production and direct integration with high speed electronic circuits. In addition, the use of Germanium [83], [84] and SiGe based devices [85] allows to enlarge the spectral response of Silicon. That is why integrated SiGe/Si technologies gained attention from research teams working in this field.

This research aims to fabricate devices with high level of responsivity without incurring in speed limitations which impair the bandwidth of the device. An important figure of merit characterizing the high-speed photodetectors is the bandwidth-efficiency product. Usually, a trade-off arises between these two parameters: increasing the quantum efficiency requires an increase in the absorption layer thickness, however this reduces the bandwidth as well.

The most common sources of bandwidth limitation are the carrier transit time and the RC time constant. The former is the time taken by the photo-generated carriers to travel across the intrinsic region of the device. The latter is given by the equivalent circuit parameters of the photodiode and load circuit: capacitive effects are due to the p-n junctions of the device or by external/parasitic capacitances.

Another parameter to be considered in high-speed photodetectors is saturation current, which needs to be as high as possible. This leads to a second trade-off with the bandwidth of the device: to obtain high-speed devices it is necessary to decrease the absorption layer volume, thus increasing the optical power density into the photodetector and leading to a lower saturation level [65]. Different device topologies have been researched over the years to find optimal solutions to the afore-mentioned trade-offs. We will focus mainly on p-i-n photodiodes and SiGe phototransistors in the following subsections.

2.6.2. *Positive-Intrinsic-Negative (PIN) photodiodes*

A p-i-n photodiode is composed of a p and n doped regions separated by an intrinsic (i.e. low doping) region. When light impinges on the intrinsic region, electron-hole pairs are created from the absorption of photons (i.e. photoelectric effect). These charge carriers do not recombine immediately as it would happen in the depletion region of a p-n diode, thanks to the lower concentration of free electrons and holes. Photodiodes operate in reverse biasing, so that, when the electric field inside the photodiode is strong enough, the carriers generated in the intrinsic region drift towards the n region (electrons) and the p region (holes), thus generating a current as summarized in Fig. 2.7. In some cases a double heterostructure can help improving the bandwidth if the n and p regions are realized with a transparent material (e.g. InP) and if the carriers are only generated in the intrinsic layer (e.g. using InGaAs). In the determination of the bandwidth of p-i-n devices, the transit time effect is the dominant parameter due to the wideness of the depletion region. This parameter is determined by the slowest moving carrier (usually holes).

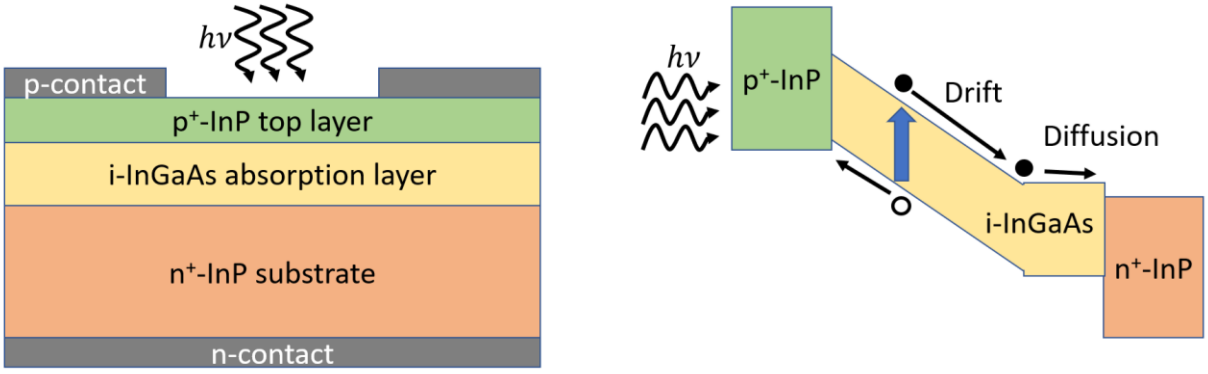

(a) (b)

Fig. 2.7: Lateral view (a) and band diagram (b) of a p-i-n diode [86].

For operations at 850 nm, a variety of different p-i-n photodetectors exists, including:

- Germanium on Silicon-on-Insulator (SOI) lateral p-i-n photodetector with interdigitated fingers [87], achieving a 34% quantum efficiency, responsivity around 234 mA/W and 29 GHz -3dB bandwidth.
- Planar silicon p-i-n photodiodes fabricated on SOI [88], achieving 12.5% quantum efficiency, responsivity around 86 mA/W and 2 GHz -3dB bandwidth.
- Standard bipolar process compliant p-i-n detectors fabricated on SOI [89] with DC responsivity of 0.09 A/W and -3dB bandwidth above 1 GHz.

Other works obtained interesting results at different wavelengths with similar structures: for instance, the SiGe p-i-n photodetector with "W structure" achieving a 489 µA/W responsivity at 1300 nm and 780 MHz -3dB bandwidth [85]. Also, Ge/Si heterojunction photodetectors achieving 2 GHz -3dB bandwidth and a 30% quantum efficiency at wavelengths between 1200 nm and 1700 nm, with a responsivity around 377 mA/W, have been shown in [83].

2.6.3. Heterojunction Phototransistors

Heterojunction Bipolar Phototransistors (HPTs) are three terminal devices based on the structure of Heterojunction Bipolar Transistors (HBTs) where layout modifications are performed to accommodate an optical window to allow the light signal to enter the device and interact with the optical absorbing material, mainly at the level of the base-collector junction. The main advantage in using HPTs as photodetectors is their internal current gain and the absence of the extensive noise levels characteristic of other high responsivity devices such as avalanche photodiodes [90]. Their three terminals structure allows them to be used in different and creative ways, such as optical mixing and injected oscillators [75], [91]. The fabrication process of HPTs is facilitated by their compatibility with HBTs, which benefit from mature technology and substrate availability. This compatibility also allows the integration of the optical receiver with the front-end circuitry, thus reducing the parasitic effects of interconnections. The vertical illumination of HPTs requires a modification of the metal contacts, while other options for illumination include lateral illumination [92] and backside illumination. The latter solution allows to improve the coupling efficiency-bandwidth trade-off: optical absorption takes place in the active region without losses of optical power and the absorption layer can be kept thin to guarantee short transit times [65]. Different semiconductors have been used in the fabrication of HPTs including: AlGaAs/GaAs [93], InGaP/GaAs [94], InGaAsInP [95], pure Si [96], SiGe/Si [97]. In this work we focus particularly on SiGe/Si HPTs so more details are given only on this kind of HPT.

SiGe HPTs have first been introduced in [97] for 940 nm operations. These devices were based on an abrupt profile SiGe HBT technology developed within Atmel, Temic and Telefunken foundries with 80 GHz f_T/f_{max} (i.e. ratio transit frequency-maximum oscillation frequency) HBT [98]. A detector with a 10x10 μm^2 optical window and abrupt profile of Ge concentration was realized, as shown in Fig. 2.8, achieving a 1.49 A/W responsivity and a -3dB bandwidth of 0.4 GHz. Further device optimization in the commercially available Telefunken technology led to an optical transition frequency of 6.5 GHz and 0.26 A/W responsivity for 850 nm operations [99], [100]. In [101], [102] HPTs realized in TSMC technology attained a responsivity of 0.43 A/W and a -3dB bandwidth of 3 GHz thanks to the introduction of trap centres removing the excess carriers.

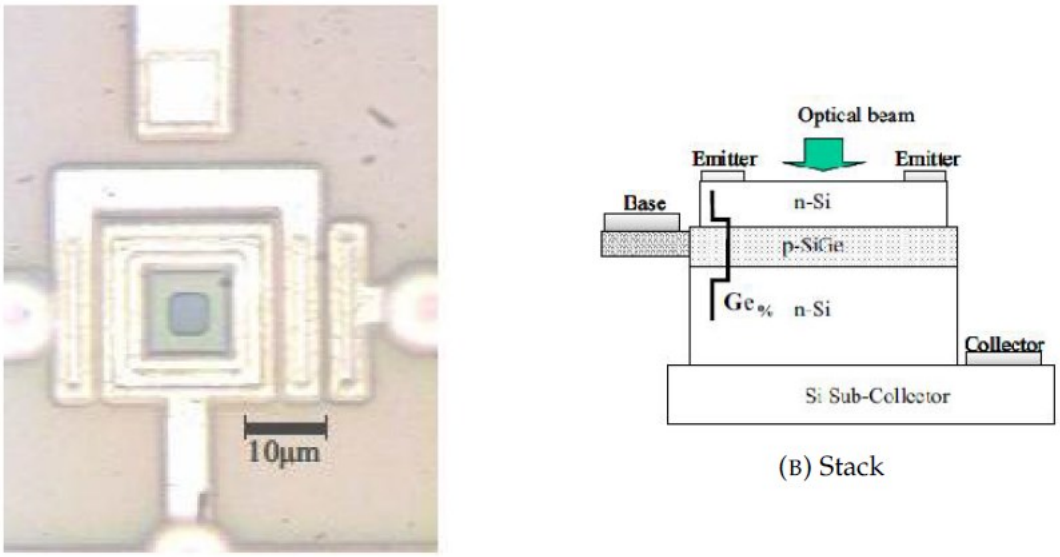

(A) Top view

(B) Stack

Fig. 2.8: Photograph of the top-view (a) and sketch of the vertical stack (b) of the first SiGe HPT [97].

Other attempts to improve the responsivity and increase the cut-off wavelength have been realized by inserting Si/SiGe multi-quantum wells between the base and the collector of the HPT, thus increasing the light absorption thanks to the smaller band-gap of Germanium. A device with 550 MHz -3dB bandwidth and 1.3 A/W responsivity has been obtained in [103]. Similar structures have reached responsivities as high as 17.5 A/W, which anyway significantly impaired the frequency response of the device [102], [104]. Finally, in [105] the results obtained with an HPT with 6x10 μm^2 optical window, fabricated in IBM 0.25 μm BiCMOS process, achieved a responsivity of 2.7 A/W and a 2 GHz bandwidth.

Previous research works conducted by the ESYCOM group have focused on the design and characterization of Si/SiGe HPTs in a Telefunken GmbH SiGe Bipolar commercial technological process. This process technology exhibits transition frequency up to 80 GHz and maximum frequency up to 90 GHz, presenting high values of Germanium content in the range of 20% - 25%, almost flat across the base. The process is a 0.8 μm lithography double polysilicon heterojunction bipolar technology [65]. The design of the SiGe/Si HPTs proposed in this project complies with the fabrication rules of standard SiGe BiCMOS technology SG13S by *IHP GmbH – Leibniz Institute for High Performance Microelectronics*. The HPTs are obtained modifying the layout of SiGe HBTs by extending the active area and removing the metal contacts and the Salicide layer (employed to lessen the resistivity in the contact area but found to impair the responsivity of the devices) from its top surface. This creates an optical window for the passage of light. SG13S is a high-performance 0.13 m BiCMOS technology, with a library containing different npn-HBTs and whose detailed description is given in [106]. This technology offers two variants of the basic HBT from which the HPTs are obtained:

- The High Speed HBT **npn13pl2**: also referred as HS-HBT, this device shows a typical maximum transit frequency of 230 GHz and a maximum oscillation frequency of 340 GHz when sized to minimum dimensions. The base-collector breakdown voltage is typically of 4.8 V.

- The High Voltage HBT **npn13v2**: also referred as HV-HBT, this device shows a typical maximum transit frequency of 50 GHz and a maximum oscillation frequency of 165 GHz when sized to minimum dimensions. The base-collector breakdown voltage is typically of 16 V.

Differences between the two devices lie within the collector region's doping: the collector of the HV-HBT is formed by the deep N-well of the CMOS process and shows low doping levels with a sheet resistance of 350 Ω/square. The HS-HBT has instead a heavily-doped collector well, formed by ion implantation, with a sheet resistance of 50 Ω/square; this doping is increased below the emitter region thanks to the Selectively Collector Implantation (SIC) which takes place after the opening of the bipolar region. An example of the doping profiles is given in Fig. 2.9. This step makes use of a dedicated mask and can be avoided in the fabrication of high voltage devices [106], [107]. The SIC limits the downwards extension of the space charge region (SCR) of the base-collector junction, thus reducing the transit time of the photogenerated carriers crossing this area and speeding up the transistor.

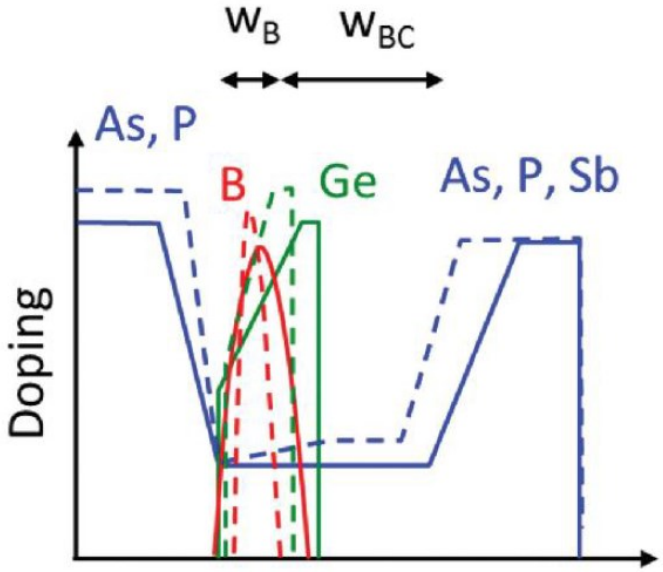

Fig. 2.9: Cross section of the device with dopant concentration. Donors are represented by the blue line and acceptors by the red line. Germanium concentration is sketched in green. The dashed lines indicate a scaled profile for enhanced frequency performance [108].

Further differences are in the emitter and collector contact regions: these are separated by a shallow trench isolation for the HV-HBT, while they are formed in the same active area for the HS-HBT, thus resulting in low collector resistance and small collector-substrate junction areas. The base resistance of both devices is lowered thanks to elevated extrinsic base regions self-aligned to the emitter. The peak Ge concentration of the graded Ge profile of the base is 25%, with a light (0.2%) Carbon doping concentration to suppress the diffusion of Boron, allowing thinner base layers [106]. A representation of the cross-section differences between the high speed and high voltage HPTs is given in Fig. 2.10.

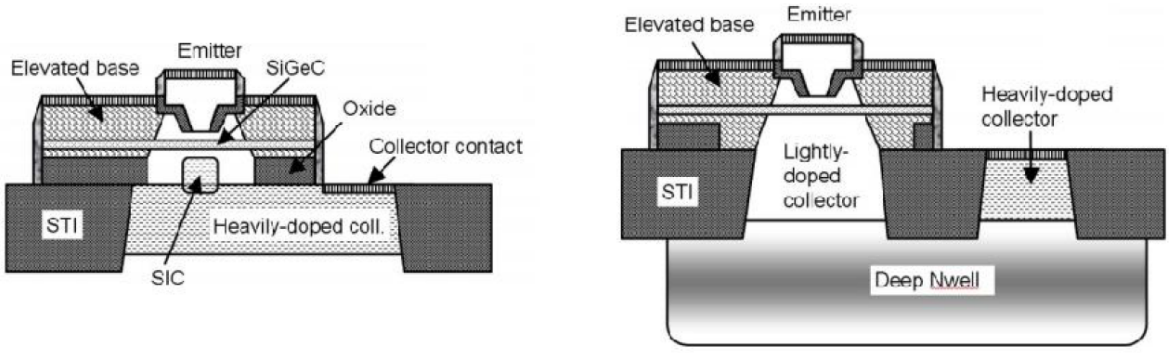

(A) High speed (B) High voltage

Fig. 2.10: Cross sections of the high speed and high voltage HPT devices realized in SG13S IHP-technology [106].

A complete physical model for phonon assisted absorption in strained-SiGe is given in [109], while an opto-electronic model for Si/SiGe HPTs is described in [110]. This model allows to attain the maximum opto-microwave (OM) gain as a function of the base-emitter and the collector-emitter loads, thus enabling comparisons to be done between devices in different materials and exploiting different configurations. The non-linear equivalent circuit is shown in Fig. 2.11. This model has been expanded in [111] to consider the distributed nature of the photogenerated sources by dividing the device into one optically activated sub-transistor and two symmetric lateral sub-transistors mostly electrically driven. In [112] the model is completed by considering the 2-dimensional carrier flow effect due to the partial lateral spreading of the active area, which differently affects the frequency behaviour of HPTs of different size.

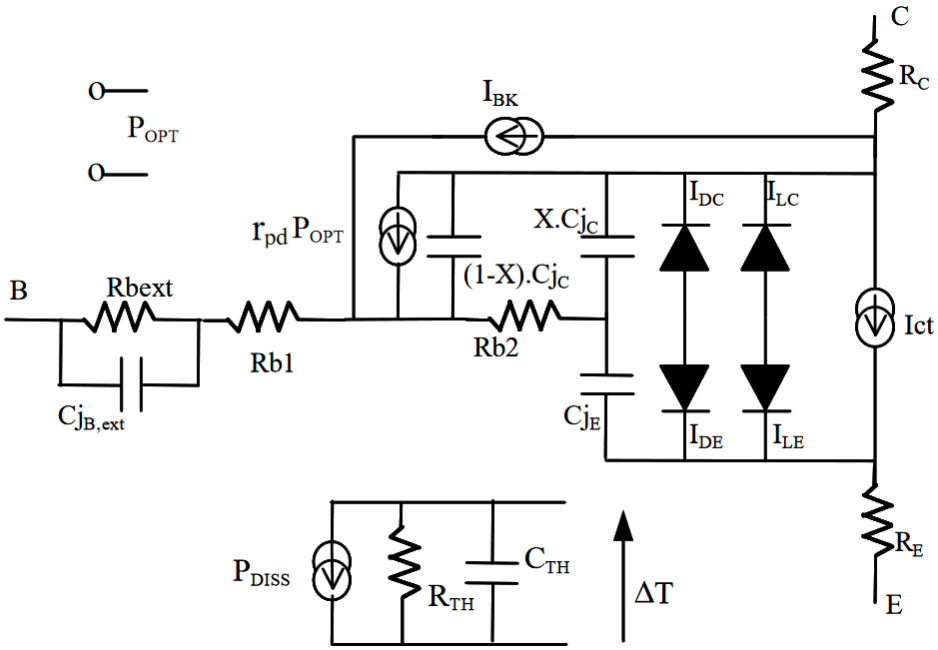

Fig. 2.11: Non linear equivalent circuit of the HPT [110].

The equivalent OM circuit proposed in [110] is shown in Fig. 2.12. As the HPT is represented as a 3-port device, its OM gain G_{OM} is represented by:

$$G_{OM} = \frac{\frac{1}{2}R_0 I_S^2}{\frac{1}{2}R_0 I_{opt}^2} = \frac{I_S^2}{I_{opt}^2} = \frac{I_S^2}{\alpha_C^2 P_{opt}^2} = |S_{32}|^2 = R_{HPT}^2 \quad (2.11)$$

where S_{32} is the S parameter linking the reflected power wave at port 3 to the incident power wave at port 2, while R_{HPT} is the HPT's responsivity. This model allowed the simulation of the small-signal OM gain at different bias voltages and load conditions. A purely reactive load on the base was found to maximize the G_{OM} of the HPT. Further models for the integration of the photodetector with electrical circuits have been proposed. In [104] a modified MEXTRAM model for the HPT simulations is given. This model includes the current sources to model the photo-generated current at the base-collector and collector-substrate junctions, early voltage reduction under constant illumination, the extra photo-gain induced by impact ionization, breakdown voltage and avalanche effect and finally the substrate contact effect to model the impulse response of the HPT.

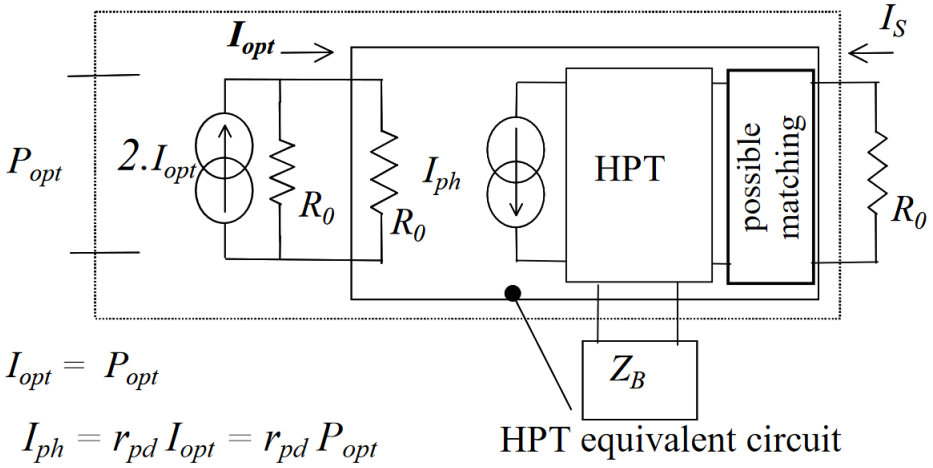

Fig. 2.12: Equivalent OM circuit of the HPT [110].

The OM gain of the HPT is limited in frequency by the junction capacitances and the carriers transit times characterizing its response. The analytical formula of the optical transition frequency, defined as the frequency at which the OM gain of the device in phototransistor mode (i.e. common emitter topology with base-emitter junction forward-polarized and base-collector junction reverse-polarized) equals its own low frequency gain in photodiode mode, once the substrate effect has been filtered out, is given by [98]:

$$f_{T-opt} = \frac{1}{2\pi\tau_{EC-opt}} = \frac{1}{2\pi\left[\frac{kT}{qI_C}\left(C_{EC} + C_{EC-opt}\right) + \tau_F + \tau_{F-opt}\right]} \quad (2.12)$$

where $g_m = \frac{kT}{qI_C}$ is the intrinsic trans-conductance at low injection, τ_F is the electrical forward transit time from emitter to collector, C_{EC} is the emitter-base and collector-base electrical junction capacitance, C_{EC-opt} is the OM capacitance increase of the emitter-base and collector-base junction due to optical illumination and τ_{F-opt} is the optical forward transit time increase from emitter to collector, which is given by:

$$\tau_{F-opt} = C_{BC-opt}(R_E + R_C) + \tau_{B-opt} + \tau_{E-opt} + \tau_{BC-opt} \quad (2.13)$$

where R_E and R_C are the dynamic emitter and collector resistances, τ_{B-opt}, τ_{E-opt} and τ_{BC-opt} are the base transit time, the emitter transit time and the base-collector depletion time delay respectively [65]. To improve the f_{T-opt} in a SiGe HPT, the forward transit times must be decreased by using a combination of vertical profile scaling as well as Ge grading across the base. The capacitive terms can also be reduced by scaling the in-plane dimensions of the device, though this negatively impacts on the coupling efficiency.

An application example of SiGe HPTs is the ORIGIN (Optical Radio Infrastructure for Gigabit/s Indoor Network) project, which was a national project dedicated to increasing the data rate and the radio coverage inside the home combining the 60 GHz wireless communication technology and RoF technology. The concept is shown in Fig. 2.13, representing a wireless communication network with different services and devices. A home network concept is created using optical fiber infrastructure to interconnect the different rooms of the house. Antennas collect the wireless signal and feed RoF transceivers to distribute the signal to each room simultaneously. At the other end of the fiber, another RoF transceiver (TRoF) converts the modulated optical signal and radiates it into the air.

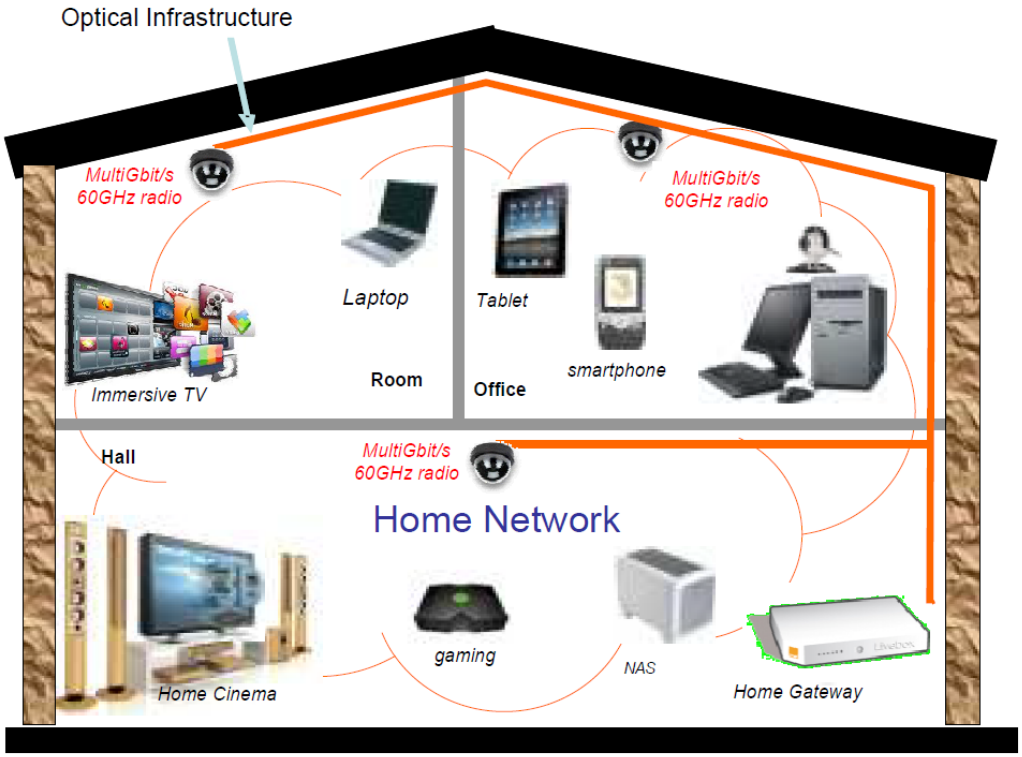

Fig. 2.13: ORIGIN project concept illustration.

The ORIGIN project started in January 2010 and finished in July 2013. It was composed of different teams of industrial and academic background collaborating. The ESYCOM team was involved in the manufacture of photonic components and their work led to the fabrication of wafers including different devices and HPT. The main interest in the ORIGIN project is that some of the developed devices are used in this thesis. In particular, the 10SQxEBC HPT is of interest for the project. The name of the HPT states that it has a square optical window of dimensions 10x10 μm^2 (10SQ) and a topology of type EBC (xEBC), meaning that all

terminals, Base, Collector and Emitter, are accessible separately. In fact, the EBC topology also means that the HPT is integrated in Common Emitter (CE) topology, therefore acting as a current amplifier.

2.7. Conclusions

This chapter presented the state-of.the-art of the components of TMA and RoF systems. The first part focused on giving an overview of the evolution and the different applications involving TMAs. The second part showed firstly the evolution of the development of the block scheme model of a RoF link, along with the definitions of the main quantities and figures of merit of its components. Then, it focused on the state-of-the-art of its single components, especially lasers and photodetectors. Lasers of VCSEL type have mainly been considered due to the interest in employing them in this thesis. For photodetectors, it showed a general description of their characteristics and provided a state-of-the-art on PIN photodiodes and HPTs, along with their main figures of merit, fabrication characteristics and models.

Chapter 3: Concept and realization of a Radio over Fiber-Time Modulated Array system.

3.1. Introduction

This chapter focuses on showing the main idea and realization of the system combining Radio-over-Fiber (RoF) and Time Modulate Array (TMA) technologies, along with sections dedicated to TMA-related challenges that have been considered and tackled. The interest in TMA as a beamforming technique is mainly due to the simplicity and low cost of the system, which relies on an On-Off switching mechanism to achieve beamforming. Although TMA systems prove to be challenging, especially in terms of efficiency, they also offer new application perspectives and a great degree of flexibility. Firstly, an accurate analysis of the TMA working principles is given. The state-of-the-art related to TMAs along with their fields of application can be found in chapter 1. Afterwards, the explanation of the concept of the RoF-TMA system, followed by a proof-of-concept of such system done by measuring the radiation pattern emitted by the system and comparing the results with software simulations. It follows a section on the analysis of the effects of unwanted phase shifts on TMA systems with measurements supporting the found results. Finally, a section on the optimization of TMA modulating sequences and the challenges related to piloting TMA systems.

The results of this chapter led to the publication of two conference papers [117] and [118] and a journal paper [119].

3.2. TMA theory and RoF-TMA system concept

3.2.1. *TMA theory*

Let us consider a generic linear array with N_a identical antennas with resonance frequency f_0. The antennas are aligned along the y-axis and are equally spaced by a fixed length D. A TMA is an antenna array where each antenna current is switched On and Off periodically with a certain pattern, called modulating sequence $U_n(t)$. All sequences are normalized between 0 and 1 and have the same frequency f_M but they have different initial delay and duty cycle. We consider a simple TMA realized by placing RF switches which periodically switch on and off the antenna currents, as shown in Fig. 3.1. The far field radiated by such system in the x-y plane is:

$$E(\theta,t) = E_0(\theta)e^{j2\pi f_0 t}\sum_{n=1}^{N_a} A_n e^{j\varphi_n} U_n(t) e^{jk(n-1)D\,sin(\theta)} \tag{3.1}$$

where $E_0(\theta)$ is the field radiated by the single element (i.e. the Element Factor), A_n and φ_n are the amplitude and phase of the n-th antenna static excitation and k is the wavenumber (i.e. $2\pi/\lambda$). The overall effect is that each antenna current is modulated by $U_n(t)$. The reference system with the antenna array and θ is shown in Fig. 3.2 to ease the understanding of the subject.

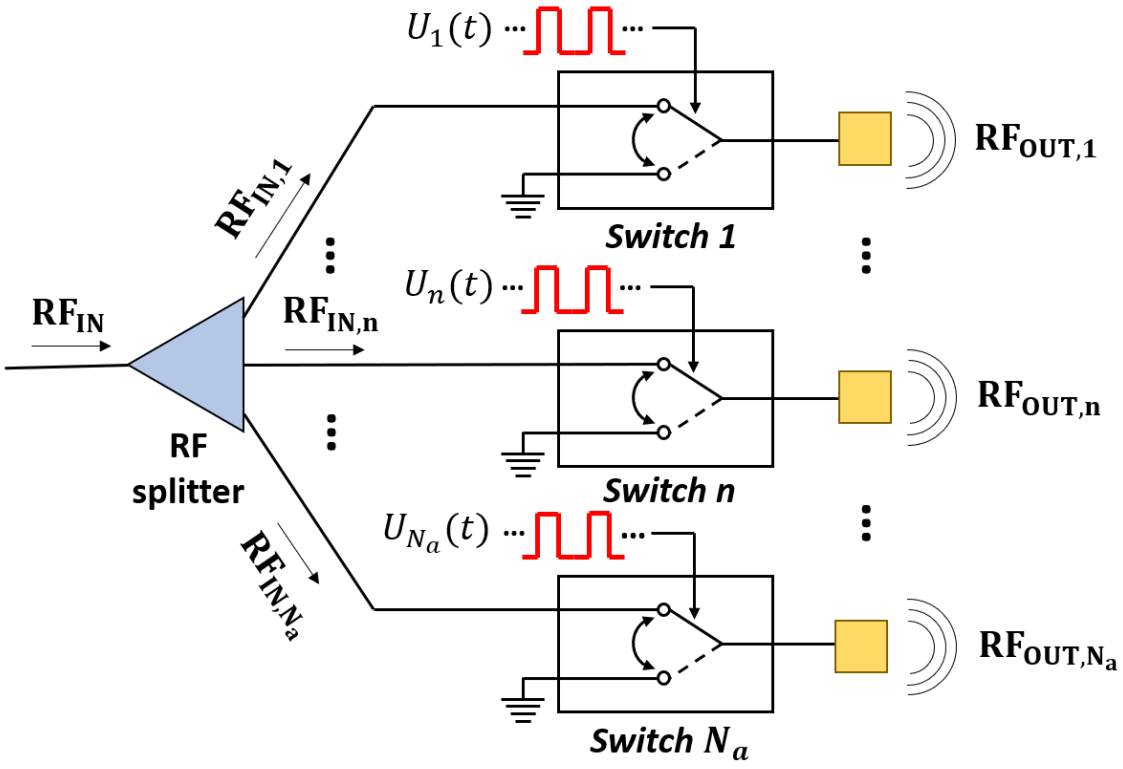

Fig. 3.1: Common scheme of an RF TMA.

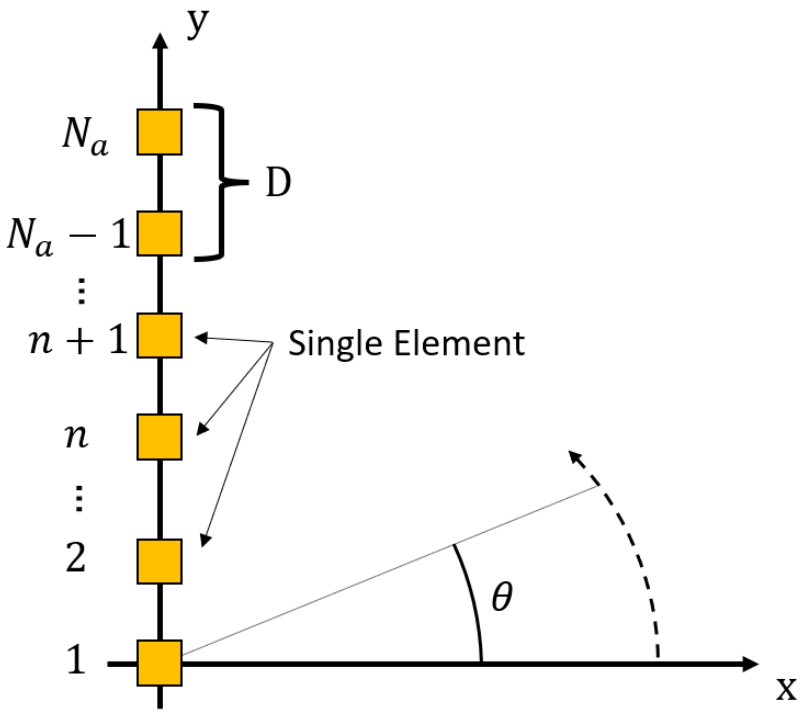

Fig. 3.2: TMA reference system.

As mentioned before, all modulating sequences have the same frequency, in other words the same period $T_M = 1/f_M$. The generic modulating sequence $U_n(t)$ is represented in Fig.

3.3, with c_n being the duty cycle and $c_{i,n}$ being the initial delay, both expressed as percentages of T_M. Given its periodicity, we write $U_n(t)$ as the Fourier series

$$U_n(t) = \sum_{h=-\infty}^{+\infty} u_{hn} e^{j2\pi h f_M t} \tag{3.2}$$

where u_{hn} denotes the h-th Fourier series coefficient. This is computed in a few simple steps: we first consider the Fourier transform of a square pulse $R(f)$ centred in 0 with a width equal to $c_n T_M$ and unitary amplitude; then, we exploit the time shift property of the Fourier Transform to shift the pulse of the quantity $\frac{c_n}{2} T_M + c_{i,n} T_M$, thus obtaining the Fourier Transform aperiodic signal $R_s(f)$; finally, the Fourier coefficient u_{hn} is equal to the Fourier Transform of the aperiodic signal evaluated in hf_M and divided by T_M.

$$R(f) = c_n T_M sinc(\pi f c_n T_M) \tag{3.3}$$

$$R_s(f) = c_n T_M sinc(\pi f c_n T_M) e^{-j2\pi f T_M \left(\frac{c_n}{2} + c_{i,n}\right)} \tag{3.4}$$

$$u_{hn} = \frac{1}{T_M} \int_0^{T_M} U_n(t) e^{-j2\pi h f_M t} dt = \frac{R_s(h f_M)}{T_M} = c_n sinc(h\pi c_n) e^{-jh\pi(c_n + 2c_{i,n})} \tag{3.5}$$

Now, by combining Eq. (3.1), Eq. (3.2) and Eq. (3.5) we obtain the following expression:

$$E(\theta, t) = E_0(\theta) \sum_{h=-\infty}^{+\infty} \sum_{n=1}^{N_a} A_n e^{j\varphi_n} c_n sinc(h\pi c_n) e^{-jh\pi(c_n + 2c_{i,n})} e^{jk(n-1)D\, sin(\theta)}\, e^{j2\pi(f_0 + h f_M)t} \tag{3.6}$$

The overall effect of the modulation is the following: the array radiates at multiple frequencies $f_0 + hf_M$, each characterized by a different radiation pattern. These patterns depend on the modulating sequences, in particular the duty cycle and the initial delay of each. Therefore, the unique feature of the simultaneous multiple beamforming in a TMA is done by tuning the modulating sequences in order to obtain a desired radiation pattern.

Under the assumption of identical array elements, the pattern multiplication principle is valid, i.e. the emitted far field of an antenna array is the product between the Element Factor and the so-called Array Factor (AF). The AF describes the interference interaction between the array elements, considered as ideal isotropic antennas, and depends on the geometry of the array. In other words, the AF represents the far field emitted by an array of ideal isotropic

antennas placed in the exact positions of the original non-ideal array elements. It is important to note that the Element Factor is an independent variable and only the AF is influenced by the sequences. Normally, a standard linear array radiates at a single frequency, with the AF depending only on the antenna spacing, the antenna excitation and on the radiation frequency. In a TMA instead, the radiation happens at multiple frequencies, thus there is a different AF for each frequency $f_0 + hf_M$:

$$AF(\theta, f_0 + hf_M) = AF_h(\theta) = \sum_{n=1}^{N_a} A_n e^{j\varphi_n} c_n sinc(h\pi c_n) e^{-jh\pi(c_n + 2c_{i,n})} e^{jk(n-1)D\ sin(\theta)} \tag{3.7}$$

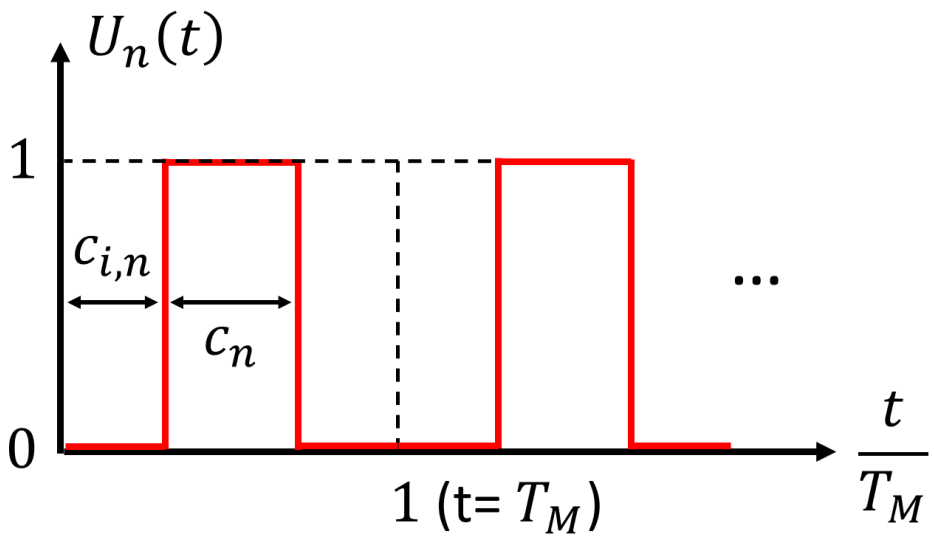

Fig. 3.3: Generic modulating sequence $U_n(t)$.

The time dependency from the complex exponential $e^{j2\pi(f_0+hf_M)t}$ has been given as implied in Eq. (3.7) and will be considered implicitly whenever referring to a radiation at a certain frequency. It can be furtherly noted that, at the carrier frequency f_0, the AF depends on c_n but not on $c_{i,n}$. In addition, c_n does not affect the phase of the AF as shown in Eq. (3.8):

$$AF_0(\theta) = \sum_{n=1}^{N_a} A_n e^{j\varphi_n} c_n e^{jk(n-1)D\ sin(\theta)} \tag{3.8}$$

This indicates that in a TMA it is not possible to do beamsteering at f_0, which is the least interesting frequency in such a kind of system. This fact along with the on-off switching of antennas poses many problems in terms of radiation efficiency. Firstly, a part of the power is wasted on frequencies that we do not wish to use, especially the carrier f_0, apart from the case where a broadside radiation is always needed. Secondly, a switched off antenna does not contribute to radiation, thus the power that it could potentially emit is wasted. Some research work aiming at improving the power efficiency of the TMA has been proposed during the years [113]-[116]. For instance, the carrier frequency radiation can be suppressed by

employing symmetric modulating waves (i.e. the modulating square wave varies between 1 and -1 instead of 1 and 0) [59].

In conclusion, the TMA beamforming results to be an easily realizable and flexible solution thanks to the modulating sequences which can be dynamically changed. These advantages come with some drawbacks, mainly related to the power efficiency and to the fact that the modulating sequences usually need to be designed with optimization tools and algorithms.

3.2.2. Structure of the system proposed

The aim of this thesis is to combine Radio-over-Fiber (RoF) technology with the TMA. The proposed system is shown in Fig. 3.4. The RF signal is converted to an optical one by a laser and coupled through an optical fiber. The fiber is then split into N_a paths by an optical splitter and each path terminates on a photodetector, which converts the optical signal back to RF. The switching/modulation necessary for the TMA is also performed by the photodetector. Finally, the modulated RF signal is sent directly to the antennas.

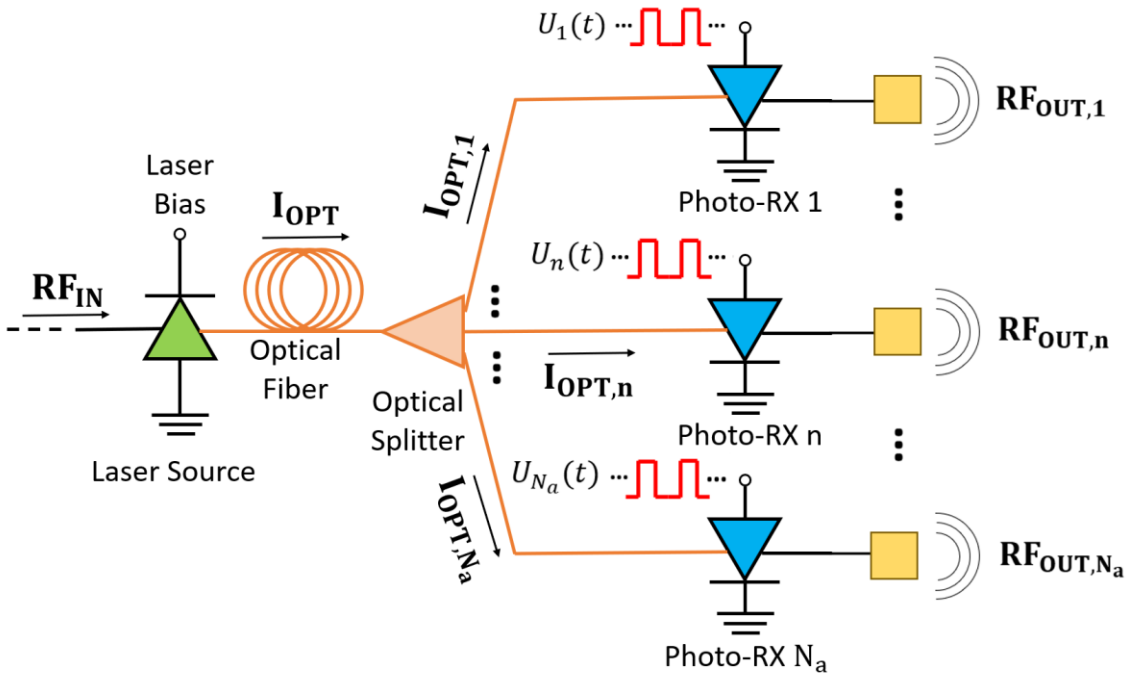

Fig. 3.4: RoF-TMA system outline.

The main differences between this system and the purely RF-TMA system presented before are that the splitting is done at optical level instead of the RF level and the square wave modulation is performed by the photodetector instead of a switch. The optical splitting implies the possibility to have high phase shifts φ_n between the different antenna currents. In fact, the phase of propagating light changes significantly within very short distances, due to the optical frequencies being much higher than the RF ones. Consequently, small length differences between the optical paths can lead to unwanted high phase shifts in the antenna currents. Therefore, it is important to analyse the impact of phase shifts φ_n on the behaviour of the system. For this reason, a study on the conditions of tolerance of unwanted phase shifts is presented in section 3.4.

The double role of the photodetector, i.e. photodetection and TMA modulation, may be covered by different devices. In this project we chose to test and study as possible solutions Photodiodes (PD) and Heterojunction Phototransistors (HPT). Sections 3.3 and 3.4 show system implementations using PDs as photodetectors. To obtain a TMA behaviour, the PDs are switched On and Off periodically by acting on their bias voltage. This causes the PDs to switch between non-polarised mode and photoconductive mode, thus modulating the photocurrent with a square wave equivalent to the switching bias.

3.3. Theoretical and experimental analysis of the RoF-TMA system

In order to prove the beamsteering capabilities of the combined RoF-TMA, we realize a small prototype and test a modulating sequence with known effects on the radiation pattern. The experimental set-up, shown in Fig. 3.6, employs a 2-element TMA realized with planar square patch antennas resonant at f_0=2.45 GHz and a RoF link composed of: a Distributed Feed-Back (DFB) laser, G652 single mode fiber as a medium, a balanced optical splitter and PIN PDs as photoreceivers. The TMA is realized with planar square patch antennas, shown in Fig. 3.5, with the following characteristics: length and width of 31.3 mm, feeding point located at 6.5 mm from the center, substrate Rogers RO4350B with thickness 1.524 mm and dielectric constant 3.48. The PDs are integrated with a Trans-Impedance Amplifier (TIA) which amplifies the generated photocurrent, but the modulating sequence is still applied only on the PD bias. The antenna spacing D is fixed to $\lambda/2$, such that $kD = \pi$. The modulating sequences are generated by an evaluation board *STM32VLDiscovery* and have a period of T_M=0.1 ms (frequency f_M=10 kHz). The choice for a low frequency modulation is not related to a particular application, but it is due to the board limitations.

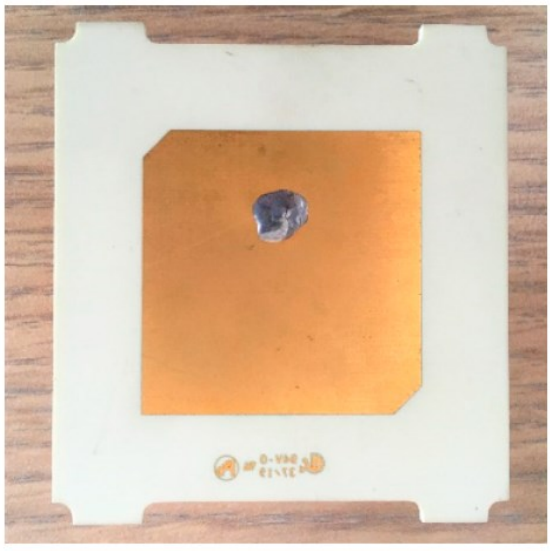

Fig. 3.5: Planar square patch antenna resonant at 2.45 GHz.

The receiving part of the system consists of a narrow beam horn antenna (i.e. very high directivity in the broadside direction) connected to a spectrum analyser (SA). The aim is to measure the radiation diagram on the xy-plane of the array at the frequencies f_0, $(f_0 + f_M)$ and $(f_0 - f_M)$. To do so, the TMA is installed on a rotating support, while the receiving horn antenna is kept fixed and aligned on the same plane. In this way, we scan the radiation diagram

of the TMA by rotating it and measuring the received power at the frequencies of interest, as shown in Fig. 3.7. The emitted field is evaluated only for θ between 90° and -90° (i.e. the half-xy-plane with positive x) due to the fact that the patch antennas radiate only in the half-plane they are facing. To better understand this choice, the radiation diagram of the single element is shown in Fig. 3.8.

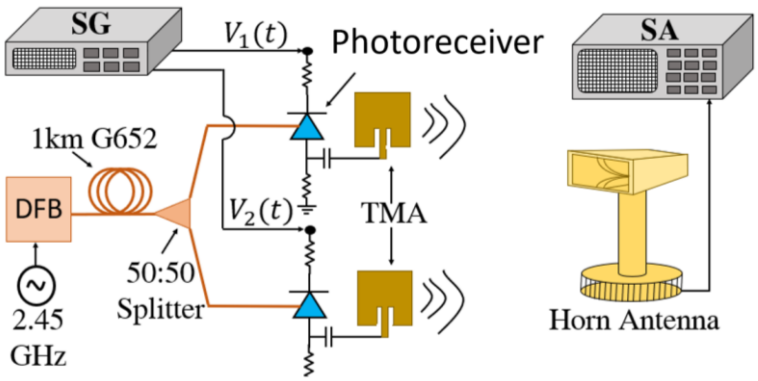

Fig. 3.6: Experimental set-up for testing the TMA beamsteering.

The resulting measurement are then compared with TMA simulations done with the software Advanced Design System (ADS) by Keysight and Matlab. The simulations did not consider the array elements as isotropic but implemented the measured radiation diagram of the single antenna shown in Fig. 3.8.

The chosen modulating sequences, depicted in Fig. 3.9, have the same amplitude (i.e. the resulting current amplitudes are the same $A_1 = A_2$), the same duty cycle and are shaped by the parameter d, so that the duty cycles are given by $c_n = 50\% - d$ and the initial delays are respectively $c_{i,1} = 0\%$ and $c_{i,2} = 50\% + d$. Therefore, both sequences are determined only by the parameter d, which determines the steering of the radiating beams.

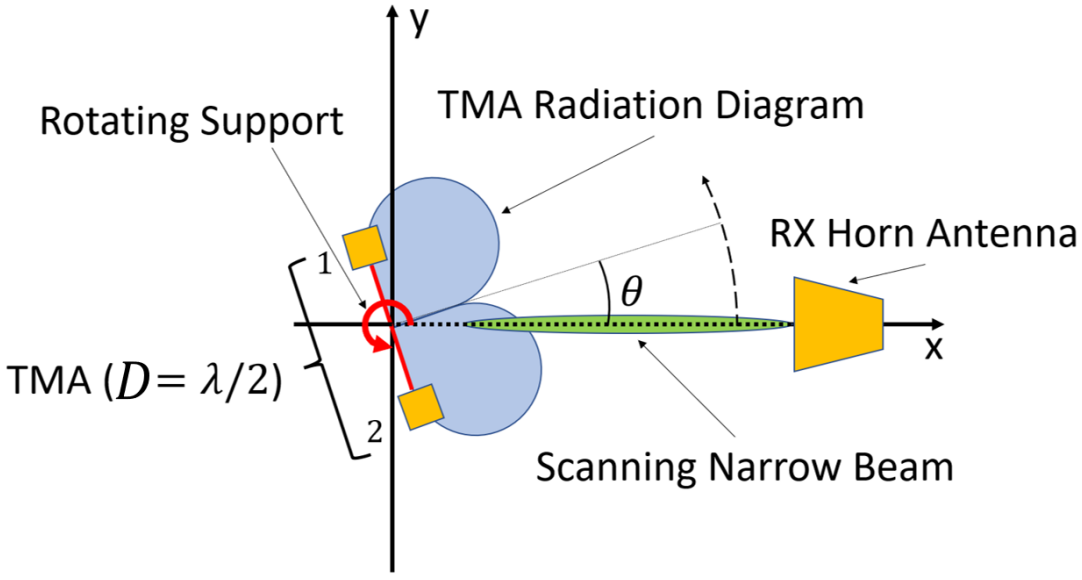

Fig. 3.7: Representation of the TMA radiation pattern scanning measurement.

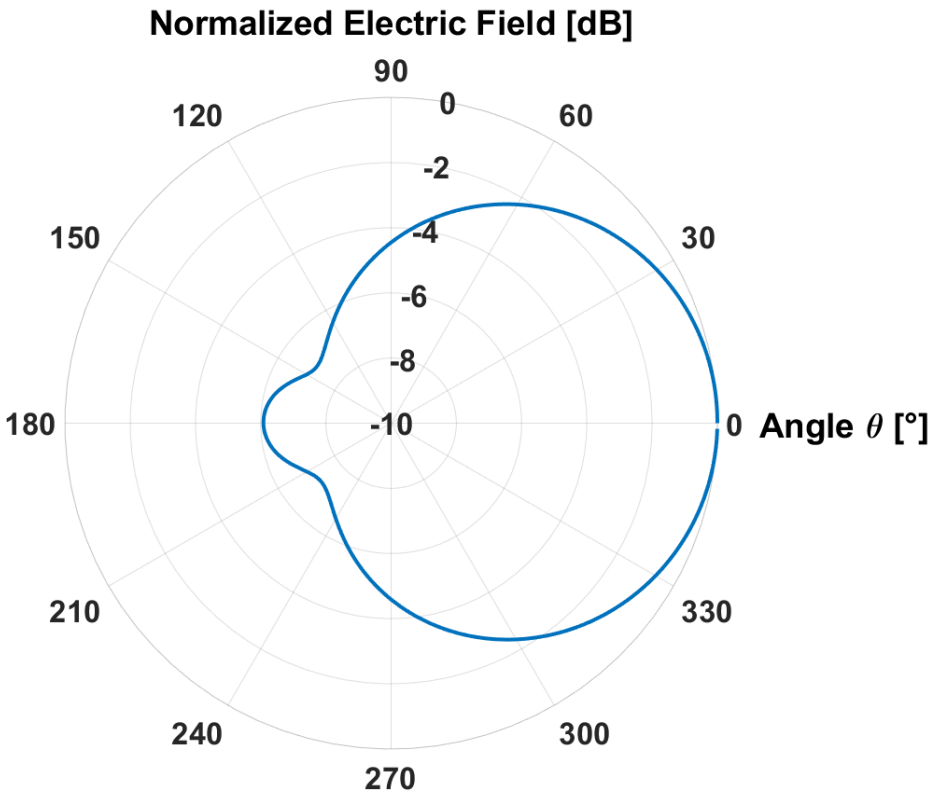

Fig. 3.8: Radiation diagram of the single element over the xy-plane

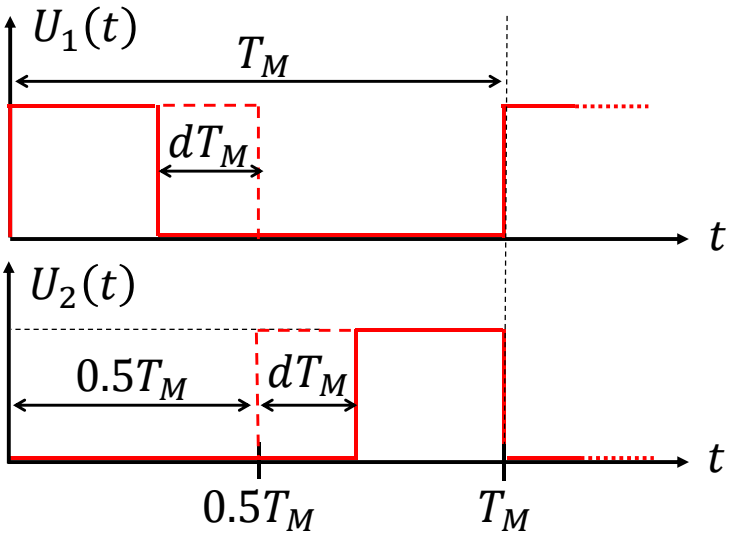

Fig. 3.9: TMA sequences $U_1(t)$ and $U_2(t)$ utilized for $N_a = 2$,with $c_1 = c_2 = 0.5 - d$, $c_{i_1} = 0$ and $c_{i_2} = (0.5 + d)T_M$.

Since the TMA has just 2 elements, the radiated patterns in the half-plane $-90° \leq \theta \leq 90°$ will have at most a single zero direction, excluding the directions $\theta = \pm 90°$, appearing when the antennas are in phase opposition with respect to the carrier. Since this zero direction can be determined with higher precision with respect to the maximum radiation direction, it is more useful to track the former and to relate it to the steering caused by d. It is important to note that the overall behaviour of the TMA is independent of the modulating frequency or the

carrier frequency, so if the RoF-TMA system is validated in a simple example scenario, it will also be for frequencies related to a specific application.

The reference situation corresponds to the modulating sequence determined by $d = 0\%$, shown in Fig. 3.10, where at the carrier frequency f_0 there is a maximum in the broadside direction, while at frequencies $f_0 \pm f_M$ there is a zero in the broadside direction. A slight asymmetry with respect to $\theta = 0°$ is observed in all the radiation patterns curves. This is in contrast with the expected behaviour at $d = 0\%$, where all curves should be symmetrical. In fact, the asymmetry is due to the presence of phase shifts φ_1 and φ_2 in the system, with φ_1 and φ_2 being the phase shifts of the first and second antenna currents. This assessment is backed up by ADS simulations implementing the phase shifts and proving the resulting asymmetry in the resulting radiation patterns. In particular, the ADS simulations were based on co-simulation, a feature allowing to combine basic circuit simulation with ADS' electromagnetic simulation engine Momentum. In this way, ADS firstly computes the modulated antenna currents in time domain through the circuit simulation tool. Then, Momentum performs the electromagnetic simulation of the TMA using the previously computed antenna currents, thus obtaining an accurate simulation of the whole system. As a convention, the phase shifts will be considered with respect to φ_1, so that $\varphi_1 = 0°$ always and $\varphi_n = \varphi_n^{measured} - \varphi_1^{measured}$.

The phase shifts have been measured with a Vector Network Analyser (VNA) by considering the phase of the S_{21} parameter between the DFB input and each photodiode's output and their value is $\varphi_1 = 0°$ and $\varphi_2 = 10°$. The phase shift stems mainly from the length difference between the optical fiber's branches after the splitter. To be noted that the length difference is small enough to not cause appreciable losses, but at the considered envelope frequency (2.45 GHz) it is sufficient a difference of 2 mm to cause a 10° phase shift.

In this case, the phase shifts are so small that they do not impact negatively on the expected behaviour of the system. A better analysis of the impact of phase shifts on the system behaviour is presented in the section 3.4, where a 3-element array is considered.

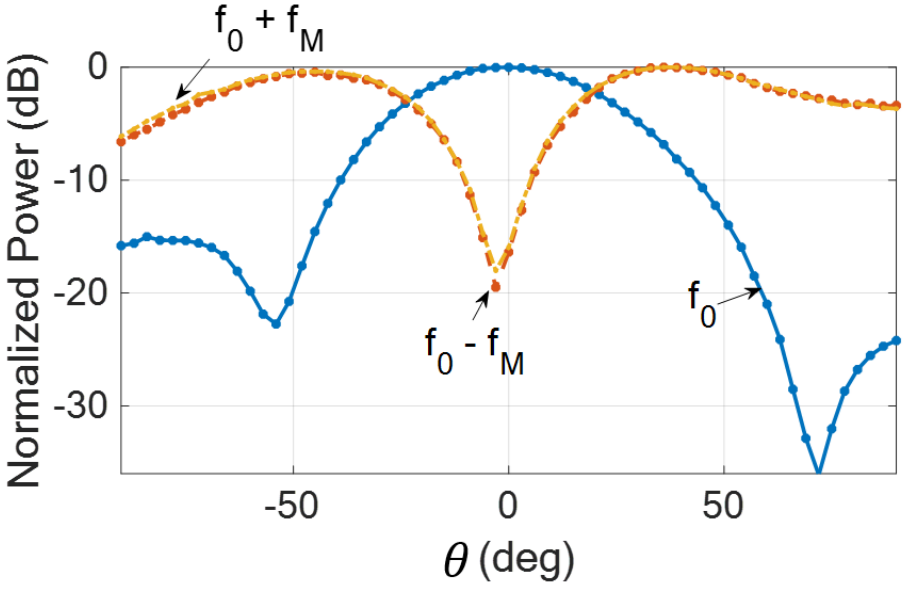

Fig. 3.10: Measurements of the radiation diagram for the carrier frequency f_0=2.45GHz and the side frequencies $f_0 + f_M$ and $f_0 - f_M$ in case $d = 0\%$ and f_M=10kHz.

By increasing d, the radiation's minima at $f_0 \pm f_M$ (and consequently the maxima) steer in opposite directions. In particular, the steering is towards +90° for $f_0 + f_M$ and -90° for $f_0 - f_M$. This is highlighted by the radiation patterns shown in Fig. 3.11(a) and Fig. 3.11(b), both relative to the case $d = 15\%$. The former image refers to the $f_0 + f_M$ frequency and shows that the zero direction is shifted of -12° with respect to the $d = 0\%$ case of Fig. 3.10, while the main beam direction moved from 39° to 27°. The latter image refers to the $f_0 - f_M$ frequency and, in the same manner, shows that the minimum shifted of +15°, while the main beam moved from -45° to -33°. In both cases, the measurements are in good agreement with the simulation results.

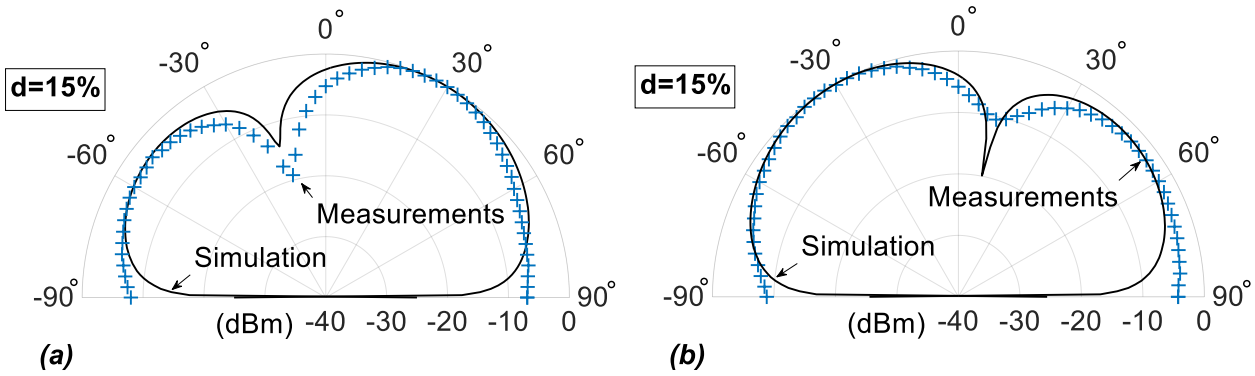

Fig. 3.11: Measurements and simulations of the radiation diagram behaviour for (a) $f_0 + f_M$ and (b) $f_0 - f_M$ in case $d = 15\%$, at f_0=2.45GHz and f_M =10kHz.

The trends of the measured maximum and minimum directions as functions of the parameter d are given in Fig. 3.12, where they are compared to the simulation results. The inset in each plot depicts Fig. 3.11(a) and Fig. 3.11(b) respectively, with the maximum and minimum points highlighted. Fig. 3.12(a) refers to the frequency $f_0 + f_M$, while Fig. 3.12(b) refers to $f_0 - f_M$. In both cases, the simulations fit well with the measurements, with the maximum registered error between the two of them being of 7°, thus demonstrating that the beamsteering in a RoF-TMA system behaves as an equivalent simulated TMA.

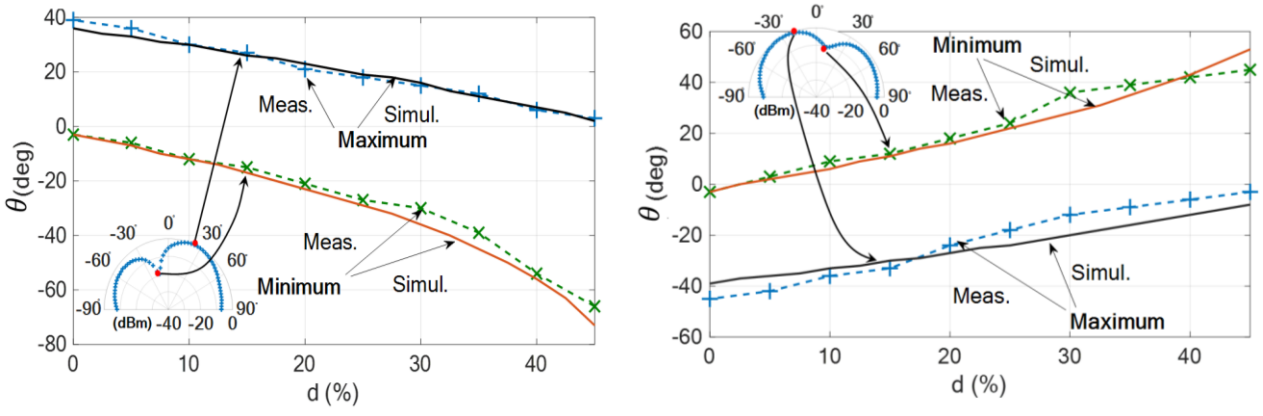

Fig. 3.12: Measurements and simulations of maximum and minimum radiation directions with respect to d for $f_0 + f_M$ (a) and $f_0 - f_M$ (b) at f_0=2.45GHz and f_M =10kHz.

The obtained results are compliant with the theory of purely RF TMA systems, thus proving that the modulation can effectively be performed at the photodetector level and validating the concept of a RoF-TMA system. In particular, the obtained performances are comparable to those shown in [42]. This work led to the publication of the conference papers [117] and [118].

3.4. Effects of unwanted phase shifts on a few-elements RoF-TMA system

3.4.1. *Analysis of the phase shift effects on a 3-element TMA*

A TMA system in ideal condition usually has uniform excitation currents and without constant phase shifts (i.e., $A_n = A$ and $\varphi_n = 0$ for every n). It is important to keep the excitation balanced and to avoid unwanted phase shifts because these parameters cannot be controlled by the modulating sequences. In presence of unbalanced excitation or unwanted phase shifts it is more difficult to control the behaviour of the TMA system and applying blindly a modulating sequence could easily lead to unexpected results. In a RoF-TMA system it is easy to avoid non-uniform excitation, due to the low losses of the fiber. On the other hand, it is easier to have unwanted phase shifts, caused by the length difference between the fibers' branches of the optical splitter. If these phase shifts are very low, they do not affect too much the system's behaviour. Furthermore, it is possible to modify the modulating sequences to decrease the negative effects of the phase shifts, but it is not easy to determine how they should be changed.

The objective of this chapter is to show how the phase shifts negatively affect the AF and to define an appropriate tolerance of this unwanted effect. To simplify the analysis of the phenomenon, let us consider the following assumptions:

- The duty cycles c_n and the coefficients A_n are constant, so that $c_n = C$ and $A_n = A$ for every n.
- We fix $c_{i,1} = 0\%$ and $\varphi_1 = 0°$.
- c_n and $c_{i,n}$ are chosen so that for every frequency of interest $f_0 + hf_M$, in the direction of the desired Maximum Radiation Direction (MRD) $\theta = \theta_0$, the complex vectors $u_{hn}e^{jknd\ sin(\theta_0)}$ of the Array Factor have all the same phase for every n (i.e. fixed h, $\langle u_{h1}e^{jkd\ sin(\theta_0)} = \langle u_{h2}e^{j2kd\ sin(\theta_0)} = \cdots = \langle u_{hn}e^{jknd\ sin(\theta_0)}$, where $\langle \cdot$ denotes the phase of the number).
- The antenna array is made of 3 antennas ($N_a = 3$) with antenna spacing D equal to $\lambda/2$, so that $kD = \pi$.

The first condition limits the choice pool of the sequences, because the duty cycles are fixed. At the same time, this allows an easier analytical formulation of the problem. The second condition fixes the first antenna as the reference for phase shifts and initial delays. These quantities can always be defined relatively to a fixed reference since they are both related to the antenna currents phases, which are periodic. The third condition states that, fixed a frequency $f_0 + hf_M$, the complex vectors composing the AF have the same phase in θ_0, leading to the expression

$$AF_h(\theta_0) = AC\ sinc(h\pi C)e^{-j\pi(hC-sin(\theta_0))}\sum_{n=1}^{3} e^{j\varphi_n} \tag{3.9}$$

Equation (3.9) is directly derived from Eq. (3.7) by applying all the assumptions described before and considering $n = 1$ for the phase of $u_{hn}e^{jknD\ sin(\theta_0)}$ (i.e., since the vectors are all in-phase by assumption, they all have the same value). The next step is to determine which modulating sequences satisfy the condition of phase alignment, which can be found by solving the following system:

$$\begin{cases} -h\pi(c_1 + 2c_{i,1}) + kDsin(\theta_0) = -h\pi(c_2 + 2c_{i,2}) + 2kD\ sin(\theta_0) + 2\pi m_1 \\ -h\pi(c_1 + 2c_{i,1}) + kDsin(\theta_0) = -h\pi(c_3 + 2c_{i,3}) + 3kD\ sin(\theta_0) + 2\pi m_2 \\ -h\pi(c_2 + 2c_{i,2}) + 2kDsin(\theta_0) = -h\pi(c_3 + 2c_{i,3}) + 3kD\ sin(\theta_0) + 2\pi m_3 \end{cases}$$

$$\rightarrow$$

$$\rightarrow \begin{cases} -h\pi C + \pi\ sin(\theta_0) = -h\pi(C + 2c_{i,2}) + 2\pi\ sin(\theta_0) + 2\pi m_1 \\ -h\pi C + \pi\ sin(\theta_0) = -h\pi(C + 2c_{i,3}) + 3\pi\ sin(\theta_0) + 2\pi m_2 \\ -h\pi(C + 2c_{i,2}) + 2\pi\ sin(\theta_0) = -h\pi(C + 2c_{i,3}) + 3\pi\ sin(\theta_0) + 2\pi m_3 \end{cases} \tag{3.10}$$

$$\rightarrow \begin{cases} sin(\theta_0) = 2hc_{i,2} - 2m_1 \\ sin(\theta_0) = hc_{i,3} - m_2 \\ sin(\theta_0) = 2h(c_{i,3} - c_{i,2}) - 2m_3 \end{cases}$$

The system is obtained by equalling the phases of all the pairs of vectors (i.e., the arguments of the complex exponentials) and the final expressions are found by applying the previous assumptions. The $2\pi m_1$, $2\pi m_2$ and $2\pi m_3$ terms, with m_1, m_2 and m_3 integers, are added due to the 2π periodicity of the phases. Solving Eq. (3.10) brings to

$$\begin{cases} sin(\theta_0) = 2hc_{i,2} - 2m_1 \\ h(2c_{i,2} - c_{i,3}) = 2m_1 - m_2 \rightarrow h(2c_{i,2} - c_{i,3}) \in \mathbb{Z} \\ h(2c_{i,2} - c_{i,3}) = m_2 - 2m_3 \end{cases} \tag{3.11}$$

If all equations in (3.11) are satisfied at the same time, then at $f_0 + hf_M$ the MRD is located at θ_0 and this maximum is guaranteed to have the highest possible value. It is important to note that the second and third equations in (3.11) imply that the quantity $h(2c_{i,2} - c_{i,3})$ must be an integer. This is because m_1, m_2 are m_3 are integers by definition, so the right-hand part of the equations is always an integer. Since only $c_{i,2}$ and $c_{i,3}$ are real quantities, there are different possible outcomes depending on their values:

- If $(2c_{i,2} - c_{i,3}) \in \mathbb{Z}$ (i.e., it is an integer), then the phase alignment assumption is met at all frequencies $f_0 + hf_M$.
- If $(2c_{i,2} - c_{i,3}) \in \mathbb{Q}\backslash\mathbb{Z}$ (i.e., it is not an integer but is rational), then the phase alignment assumption is met only for specific values of h.
- If $(2c_{i,2} - c_{i,3}) \in \mathbb{R}\backslash\mathbb{Q}$ (i.e., it is irrational), then the phase alignment assumption is never met.

Once a proper modulating sequence is chosen, the next step is to analyse how the phase shifts impact on the Array Factor, the core quantity of a TMA. The power radiated by the array is proportional to the absolute squared value of the electric field it emits, $|E(\theta,t)|^2$, which in turn is the product between Element Factor and Array Factor. Therefore, the power at frequency $f_0 + hf_M$ is proportional to

$$|AF_h(\theta)|^2 = A^2C^2 sinc^2(h\pi C)\left|\sum_{n=1}^{3} e^{j\varphi_n} e^{-jh\pi\left(C-2c_{i,n}\right)} e^{j(n-1)\pi\, sin(\theta)}\right|^2 \tag{3.12}$$

This equation can be furtherly extended by exploiting the following property of complex numbers:

$$\begin{aligned}\left|\sum_{n=1}^{N} X_n\right|^2 &= \sum_{n=1}^{N}\sum_{m=1}^{N} \Re e\{X_n X_m^*\} = \sum_{n=1}^{N}\sum_{m=1}^{N} |X_n||X_m|\cos\left(\langle X_n - \langle X_m\right) \\ &= \sum_{n=1}^{N} |X_n|^2 + \sum_{n=2}^{N}\sum_{m=1}^{n-1} 2|X_n||X_m|\cos\left(\langle X_n - \langle X_m\right)\end{aligned} \tag{3.13}$$

with X_n complex numbers. Applying (3.10) and (3.13) to (3.12) leads to the following expression for the squared modulus sum

$$\begin{aligned}&\left|\sum_{n=1}^{3} e^{j\varphi_n} e^{-jh\pi\left(C-2c_{i,n}\right)} e^{j(n-1)\pi\, sin(\theta)}\right|^2 = \\ &= 3 + 2\Re e\left\{e^{j\left(\pi\, sin(\theta_0) - \pi\, sin(\theta) - \frac{\varphi_3}{2}\right)}\left(2cos\left(\varphi_2 - \frac{\varphi_3}{2}\right)\right.\right. \\ &\qquad \left.\left. + e^{j\left(\pi\, sin(\theta_0) - \pi\, sin(\theta) - \frac{\varphi_3}{2}\right)}\right)\right\}\end{aligned} \tag{3.14}$$

This last expression is very important as it expresses how the unwanted phase shifts φ_2 and φ_3 affect the AF. Let us analyse how the MRD depends on the phase shifts values and define the general MRD as θ_{max}. It is important to distinguish θ_0 and θ_{max} conceptually: the former is the wanted MRD, while the latter is the general MRD. In other words, θ_0 is the MRD when $\varphi_n = 0$, while θ_{max} is the MRD when $\varphi_n \neq 0$. For fixed values of φ_2 and φ_3, the value of θ_{max} depends on the sign of $cos\left(\varphi_2 - \frac{\varphi_3}{2}\right)$. The two different scenarios are given by the following expressions:

$$\begin{aligned}\theta_{max} &= arcsin\left(sin(\theta_0) - \frac{\varphi_3}{2\pi} - 2m\right) = \Theta, if\ cos\left(\varphi_2 - \frac{\varphi_3}{2}\right) > 0 \\ \theta_{max} &= arcsin\left(sin(\theta_0) - \frac{\varphi_3}{2\pi} - (2m+1)\right) = \Psi, if\ cos\left(\varphi_2 - \frac{\varphi_3}{2}\right) < 0\end{aligned} \tag{3.15}$$

where m is an arbitrary integer value to keep the arcsin argument in its domain [-1;1]. The two expressions have been labelled Θ and Ψ for later use. Equations (3.15) explain how the phase shifts affect the MRD. In particular, a change in φ_3 always modifies θ_{max}, while a change in φ_2 does not affect the MRD, unless the sign of $cos\left(\varphi_2 - \frac{\varphi_3}{2}\right)$ is switched. The

system's tolerance to unwanted phase shifts is evaluated in terms of the angle deviation from the desired MRD θ_0. By defining a maximum deviation threshold θ_{th}, we want to find the allowed phase shifts domains $\varphi_3 \in [\varphi_{3,max}^-; \varphi_{3,max}^+]$ and $\varphi_2 \in [\varphi_{2,max}^-; \varphi_{2,max}^+]$ such that $\theta_0 - \theta_{th} \leq \theta_{max} \leq \theta_0 + \theta_{th}$. In the following, we will consider a θ_{th} equal to 5°.

Let us fix φ_2 for the moment, such that θ_{max} is given by Θ in (3.15). Regarding φ_3, the domain extremes $\varphi_{3,max}^+$ and $\varphi_{3,max}^-$ are the values of φ_3 for which $\theta_{max} = \theta_0 \pm \theta_{th}$:

$$\varphi_{3,max}^{+,-} = 2\pi\big(sin(\theta_0) - sin(\theta_0 \pm \theta_{th})\big) \tag{3.16}$$

So, the first outcome of this analysis is that the values $\varphi_{3,max}^{+,-}$ depend on θ_0. The closer θ_0 is to $\pm 90°$ and the lower the interval $\varphi_{3,max}^+ - \varphi_{3,max}^-$ (i.e., the interval of the allowed values of φ_3) becomes, as shown in Fig. 3.13.

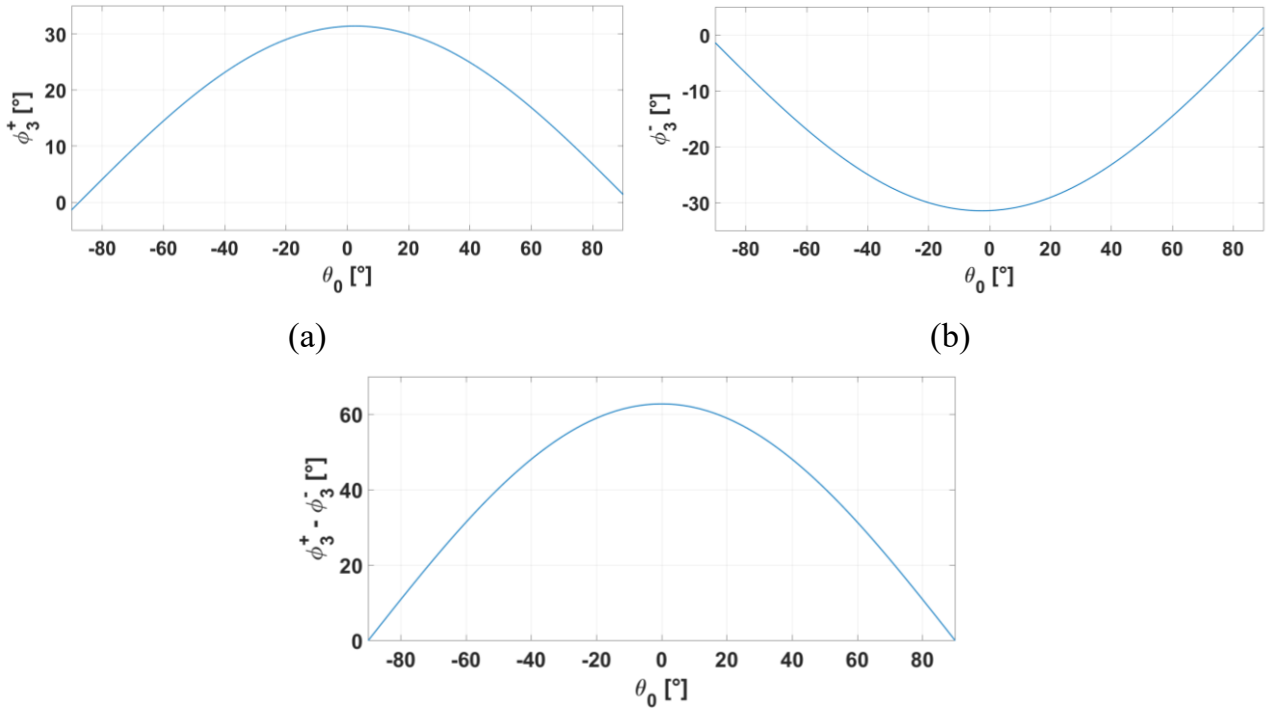

Fig. 3.13: Behaviour of $\varphi_{3,max}^+$ (a) and $\varphi_{3,max}^-$ (b) when $\theta_{th} = 5°$. (c) depicts the difference $\varphi_{3,max}^+ - \varphi_{3,max}^-$.

The next step is to define a proper tolerance interval also for φ_2. The main idea is to consider the interval of positivity of $cos\left(\varphi_2 - \frac{\varphi_3}{2}\right)$, leading to

$$\frac{\varphi_3 - \pi}{2} \leq \varphi_2 \leq \frac{\varphi_3 + \pi}{2} \tag{3.17}$$

where the boundaries of the interval correspond to $cos\left(\varphi_2 - \frac{\varphi_3}{2}\right) = 0$. In these two limit cases, Eq. (3.12) has the same value in both directions Θ and Ψ, defined in (3.15), meaning that the array radiates the same power in two different directions. Having in mind that the objective is to find phase shifts intervals for which the received radiation pattern does not

differ much from the ideal case, it is natural to consider the limit cases of Eq. (3.17) as too much different. This means that the domain of φ_2 in (3.17) must be restricted to a smaller interval.

To do this, we first consider the ratio of $|AF_h(\theta)|^2$ evaluated in the directions Θ and Ψ. In fact, we already observed that by changing φ_2 there is an exchange of power between Θ and Ψ. These directions correspond to two lobes, where Θ is the desired main lobe direction, while Ψ is a desired secondary lobe. The lobe ratio expression between Θ and Ψ is then:

$$\frac{|AF_h(\Theta)|^2}{|AF_h(\Psi)|^2} = \frac{5 + 4\,cos\left(\varphi_2 - \frac{\varphi_3}{2}\right)}{5 - 4\,cos\left(\varphi_2 - \frac{\varphi_3}{2}\right)} \tag{3.18}$$

The range of (3.18) is [1/9; 9] and its shape is represented in Fig. 3.14. This quantity represents the threshold tolerance parameter associated to φ_2, like θ_{th} is the threshold tolerance parameter associated to φ_3. For instance, the interval shown in (3.17) corresponds to a value of (3.18) equal to 1, meaning that the maximum acceptable values of φ_2 are such that the ratio between the main lobe and the secondary lobe levels is equal to 1. We arbitrarily fix (3.18) to a value of 4.5, meaning that we want the power in Θ to be at least 4.5 times more than the power in Ψ. This corresponds to an interval of φ_2 approximately equal to $\frac{\varphi_3}{2} - 37° \leq \varphi_2 \leq \frac{\varphi_3}{2} + 37°$.

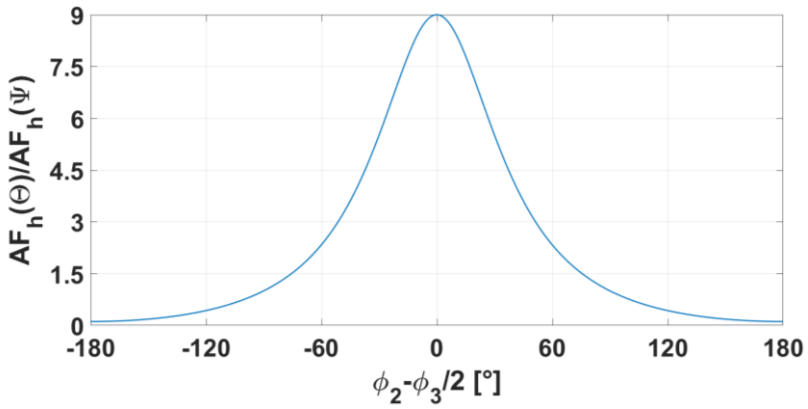

Fig. 3.14: Behaviour of $\frac{|AF_h(\Theta)|^2}{|AF_h(\Psi)|^2}$ in function of the argument of the cosine: $\varphi_2 - \frac{\varphi_3}{2}$

A graphical representation of the phase shifts tolerance intervals is given in Fig. 3.15, where all the plots are related to the case $\theta_0 = 0°$. In particular, Fig. 3.15(a) represents (3.18), while Fig. 3.15(c) represents the angle deviation from θ_0 (i.e. $|\theta_{max} - \theta_0|$), where the surface domain was restricted to the values of φ_2 and φ_3 satisfying the condition $cos\left(\varphi_2 - \frac{\varphi_3}{2}\right) > 0$. Fig. 3.15(b) and Fig. 3.15(d) represent the set of the allowed phase shifts φ_2 and φ_3 for $\theta_{th} = 5°$ and lobe ratio equal to 2. These sets are obtained considering the domains associated to values of higher than 4.5 for (3.18) in Fig. 3.15(a) and to deviations $|\theta_{max} - \theta_0|$ lower than 5° in Fig. 3.15(c). Lastly, Fig. 3.15(e) is the intersection between Fig. 3.15(b) and Fig. 3.15(d) and represents the domain of allowed phase shifts φ_2 and φ_3 satisfying the imposed conditions on θ_{th} and (3.18).

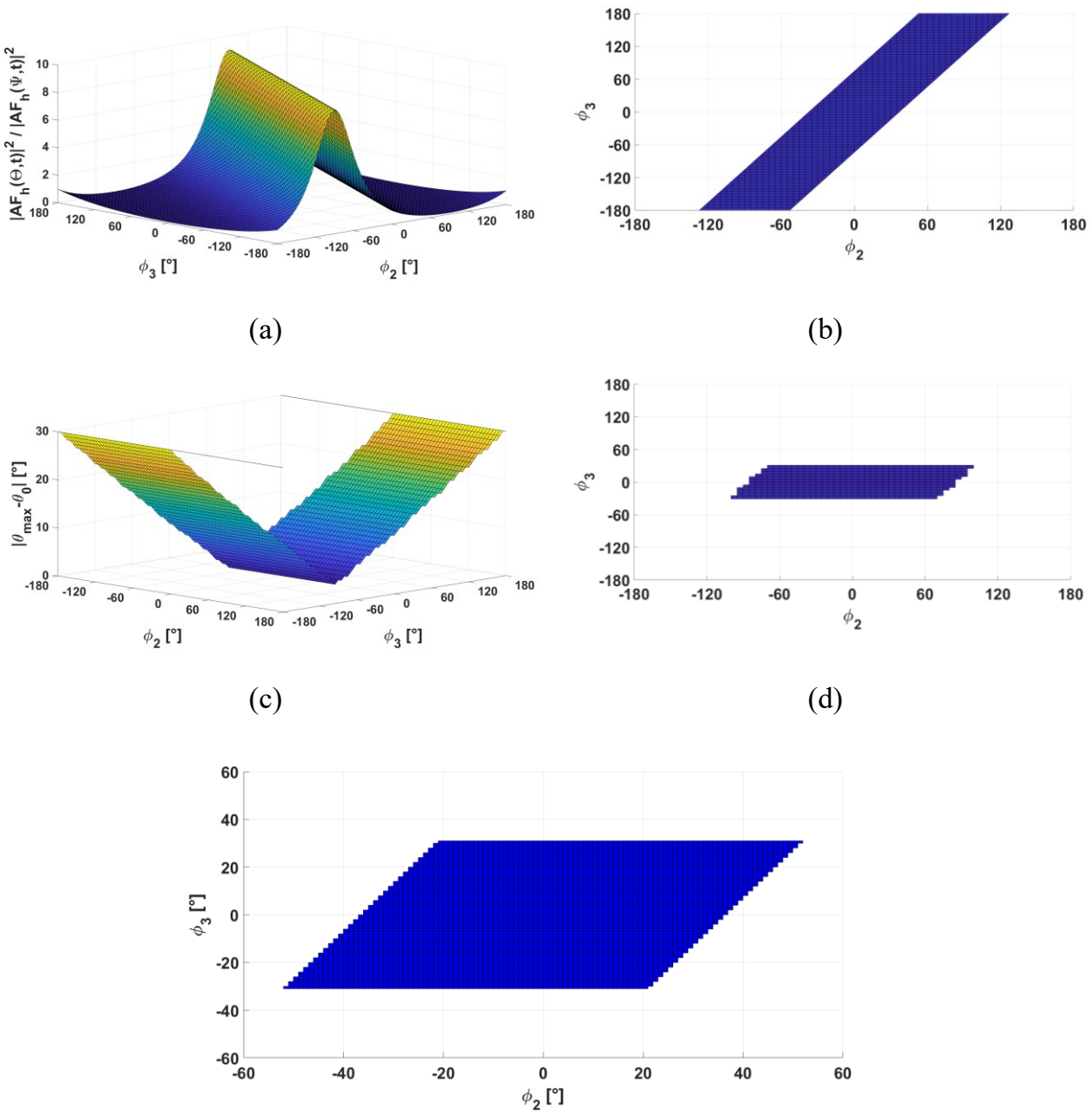

Fig. 3.15: (a) behaviour of $\frac{|AF_h(\Theta)|^2}{|AF_h(\Psi)|^2}$. (b) domain for which $\frac{|AF_h(\Theta)|^2}{|AF_h(\Psi)|^2} \geq 4.5$. (c) behaviour of $|\theta_{max} - \theta_0|$. (d) domain for which $|\theta_{max} - \theta_0| < 5°$. (e) intersection between (b) and (d).

In conclusion, if the phase shifts are within the tolerance domain in Fig. 3.15(e), then the TMA behaviour is guaranteed to be similar to the expected one, referred to the ideal case without phase shifts.

3.4.2. *Experimental validation of the phase shifts effects on a 3-element TMA*

In this section, the theoretical analysis of the phase shift impact on the TMA developed in section 3.4.1 is validated through measurements. In addition, the Matlab simulations shown in section 3.4.1 are adapted to the practical cases that will be shown in the current section for a comparison with the measurements. The experimental set-up adopted is shown in Fig. 3.16 and it is composed of a RoF link followed by a 3-element antenna array, realized with planar square patch antennas resonant at 2.45 GHz. The RoF system consists of an Optical Transmitter based on a directly modulated laser, followed by 1 km of single mode G652 optical fiber, and by a 1:3 optical splitter, ending in three photodetectors. Like in the RoF-TMA validation case, the laser and the photodetectors are a DFB and PIN photodiodes integrated with a TIA. In the case of a 2-element array, the analysis results simpler and trivial, hence the choice to study a 3-element array instead. This work led to the publication of the journal paper [119].

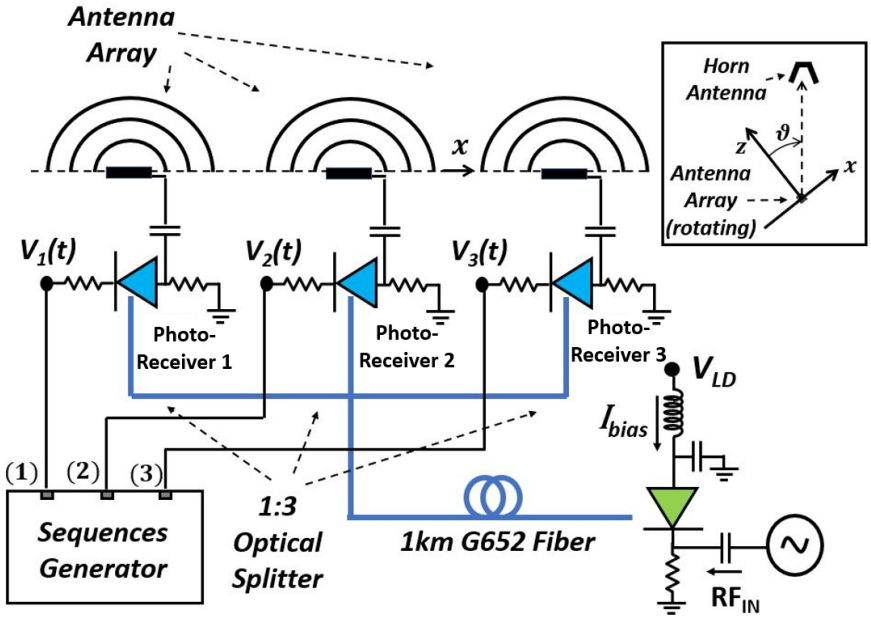

Fig. 3.16: Experimental set-up with the RoF link using a DFB laser and PIN photodiodes. In the inset the reference system of the TMA with respect to the receiving horn antenna.

The modulating sequences are generated by an evaluation board *STM32VLDiscovery* and have a modulation frequency f_M of 10 kHz, duty cycles c_n equal to 80% and initial delays $c_{i,n}$ equal to 0%, 33% and 66%, respectively, as shown in Fig. 3.17. These sequences do not correspond to an optimum exploitation of the TMA but rather represent just a simple example for the theoretical approach validation. The quality condition on φ_2 (3.18) is set to 4.5, meaning that $\frac{\varphi_3}{2} - 37° \leq \varphi_2 \leq \frac{\varphi_3}{2} + 37°$, while the angle shift tolerance threshold θ_{th} is set to 5°. The analysed frequencies range from f_0 to $f_0 + 4f_M$ and a TDK horn antenna receives the radiated power to measure the radiation pattern. The measurements of the radiation pattern are performed in the same way described in section 3.3.

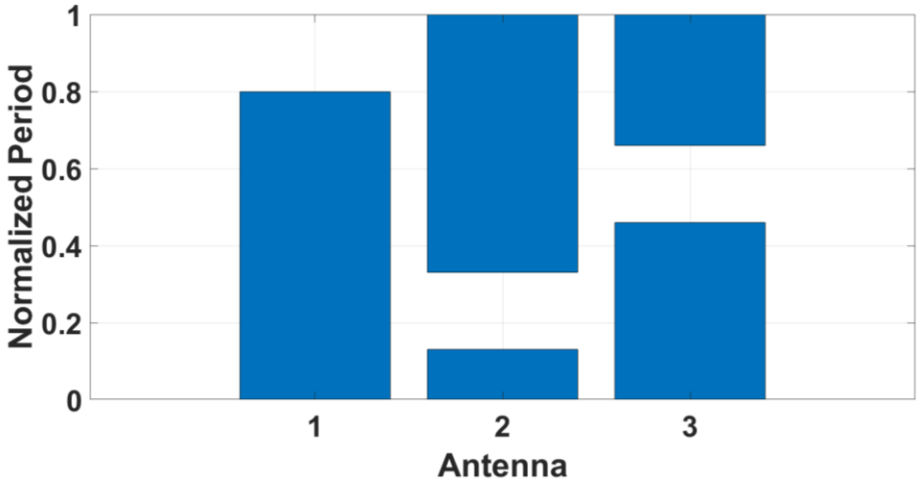

Fig. 3.17: Graphical representation of the chosen sequences. The length of the bar represents the duty cycle, while the starting point represents the initial delay.

Fig. 3.18(a) shows the ideal (i.e. without phase shifts) normalized $|AF_h(\theta,t)|^2$ obtained by applying the test sequence, while Tab. 3.1 summarizes the different MRD and $\varphi_{3,max}^{+,-}$ of each harmonic. Fig. 3.18(b) represents the domain of tolerable phase shifts φ_2 and φ_3 relative to all the considered frequencies. In particular, for each frequency the tolerance intervals of phase shifts are determined according to the study shown in the previous section defining a phase shift domain. Then the total domain is obtained by intersecting all the domains of each frequency. To satisfy (3.19) for every considered frequency, it must be $-25.2° \leq \varphi_3 \leq 24.9°$. This interval is obtained by intersecting all intervals in Tab. 3.1. For a comparison, in the image it has been included the domain found in Fig. 3.18(e). It can be noted that the latter is larger in size. This is because this domain was determined for a single frequency with MRD 0°, which is the best-case scenario. In general, the more the MRD approaches $\pm 90°$ and the smaller is the tolerance interval of φ_3. Considering multiple frequencies with different MRDs, the size of the allowed phase shifts domain is determined by the furthest MRD with respect to the broadside direction.

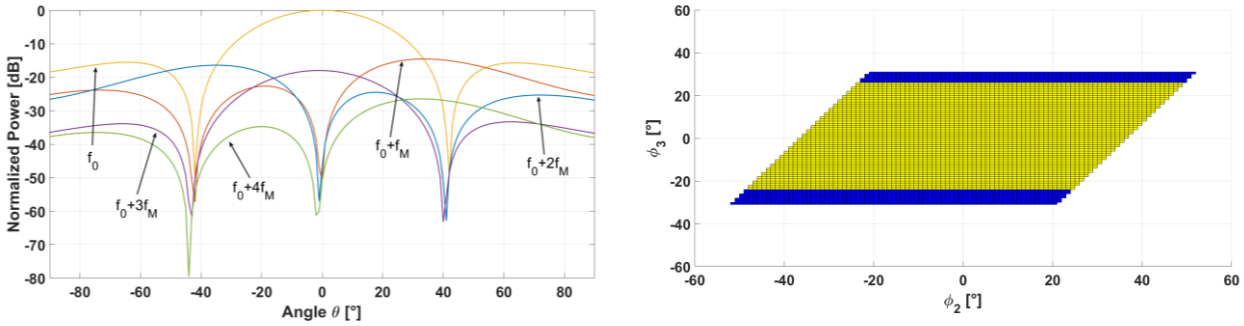

(a) (b)

Fig. 3.18: (a) simulations of the test sequence with zero phase shifts at $f_0 + hf_M$, $h \in [0,4]$. (b) domain of allowed phase shifts (yellow area) compared to Fig. 3.15e (blue areas).

f	θ_0	$\varphi^{+}_{3,max}$	$\varphi^{-}_{3,max}$
$f_0 + f_M$	34°	26.8°	-25.2°
$f_0 + 2f_M$	-35°	24.9°	-26.5°
$f_0 + 3f_M$	-1°	31.3°	-31.4°
$f_0 + 4f_M$	33°	27.1°	-25.6°

Tab. 3.1: Values of the desired MRD θ_0 and of the maximum and minimum allowed phase shift φ_3 for each frequency $f_0 + hf_M$ related to the test sequence.

The antenna currents have inherent phase shifts φ_n different from 0° due to the splitter ends having slightly different lengths. Considering that the transmitted RF signal has frequency 2.45 GHz and an approximated index of refraction of 1.5 for silica, then a fiber strand long 2.3 mm is sufficient to cause a phase shift of 10° in the antenna current. Each φ_n is changed by putting additional strands of fiber to the corresponding splitter output. In this way, it is possible to measure the received radiation pattern in different phase shifts conditions. Three different cases are considered:

1. Only φ_3 out of its tolerance domain.
2. Only φ_2 out of its tolerance domain.
3. Both φ_2 and φ_3 within their tolerance domain.

In the first scenario, the phase shifts $\varphi_2 = 31.2°$ and $\varphi_3 = 58.6°$ are applied. In this case, only φ_3 is out of the tolerance range, as the interval for φ_2 is bounded by $\frac{\varphi_3}{2} + 37° = 66.3°$ and $\frac{\varphi_3}{2} - 37° = -7.7°$, while φ_3 is above the maximum upper bound $\varphi^{+}_{3,max}$=31.3° in Tab. 3.1. Consequently, the MRDs at all frequencies under test are expected to be shifted of more than the tolerance value $\theta_{th} = 5°$. This means that by applying a known sequence in presence of phase shifts, the TMA behaves unexpectedly and emits in the wrong directions. To avoid this situation, it is fundamental to ensure that the antenna paths have equal or almost-equal phase, depending on the degree of tolerance fixed by the user. Alternatively, optimization tools can be used to solve phase shifts impairments, as shown in section 3.5.

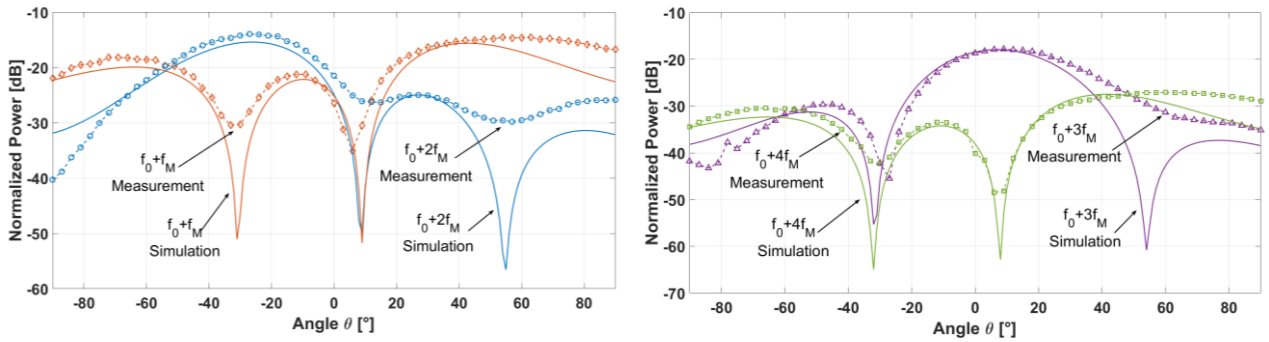

(a) (b)

Fig. 3.19: Simulated and measured Radiation Diagrams when φ_3 is out of bounds. (a) $(f_0 + f_M)$ and $(f_0 + 2f_M)$ frequencies. (b) $(f_0 + 3f_M)$ and $(f_0 + 4f_M)$ frequencies.

f	Measured θ_{max}	Simulated Θ	Simulated Ψ
$f_0 + f_M$	63°	55.5°	-10°
$f_0 + 2f_M$	-27°	-31°	29°
$f_0 + 3f_M$	9°	8°	-59°
$f_0 + 4f_M$	60°	53.5°	-11.5°

Tab. 3.2. MRD θ_{max}, simulated Θ and Ψ directions at $(f_0 + hf_M)$ for φ_3 out of bounds.

The resulting simulations and measurements are summarized in Tab. 3.2 and Fig. 3.19. The plots depict the comparison between simulations and measurements are organized in two distinct figures for clarity. In particular, Fig. 3.19(a) is related to frequencies $f_0 + f_M$ and $f_0 + 2f_M$, while Fig. 3.19(b) to $f_0 + 3f_M$ and $f_0 + 4f_M$. All the radiation diagrams are normalized with respect to the maximum received power at f_0. The measurements are in good accordance with the simulations and the MRDs are shifted of more than 5°, thus confirming the expected results.

In the second scenario, the phase shifts $\varphi_2 = 106.6°$ and $\varphi_3 = -10.2°$ are applied. In this case, φ_3 is in its own range for all frequencies of interest, i.e. between -25.2° and 24.9°, while φ_2 is out of bounds, which are -42.1° and 31.9°. Additionally, this value of φ_2 also exceeds $\frac{\varphi_3}{2} + 90° = 84.9°$, meaning that the MRD is actually located in Ψ. In Tab. 3.3 and Fig. 3.20, simulations and measurements are compared as in the previous case. It can be noted that, according to the expectations, even if φ_3 is in the range of tolerance, the MRD is not located in Θ but in Ψ, whose values are listed in Tab. 3.3. Additionally, the side lobe level and the extinction ratio (i.e. the ratio between the highest and the lowest values) of the radiation diagrams are worse compared to the ideal case. Overall, the results related to the out of bounds phase shifts are compliant with the expectations.

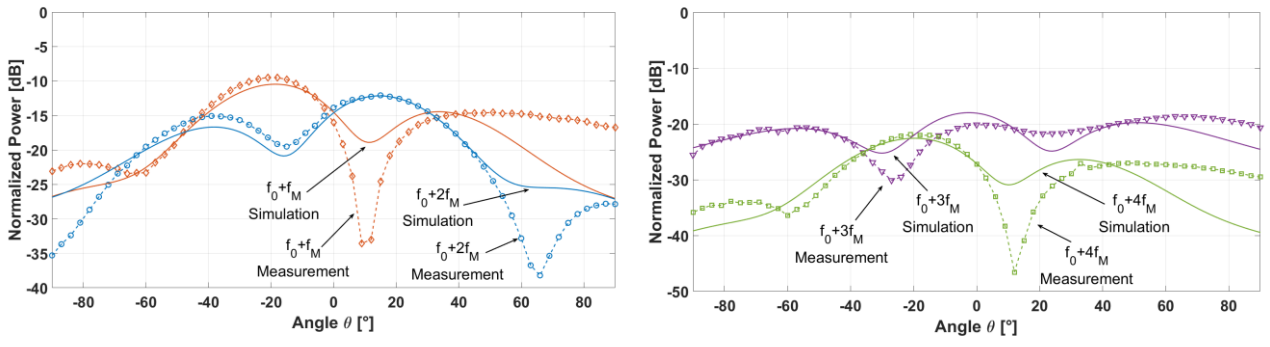

(a) (b)

Fig. 3.20: Simulated and measured Radiation Diagrams when φ_2 is out of bounds. (a) $(f_0 + f_M)$ and $(f_0 + 2f_M)$ frequencies. (b) $(f_0 + 3f_M)$ and $(f_0 + 4f_M)$ frequencies.

f	Measured θ_{max}	Simulated Θ	Simulated Ψ
$f_0 + f_M$	-21°	39.5°	-21.5°
$f_0 + 2f_M$	15°	-45°	17°
$f_0 + 3f_M$	63°	-2.5°	72.5°
$f_0 + 4f_M$	-21°	38°	-23°

Tab. 3.3: MRD θ_{max}, simulated Θ and Ψ directions at $(f_0 + hf_M)$ for φ_2 out of bounds.

In the last scenario, the phase shifts $\varphi_2 = -34.8°$ and $\varphi_3 = -7.4°$ are applied to the TMA. Both are within the intervals of tolerance $-40.7° \leq \varphi_2 \leq 33.3°$ and $-25.2° \leq \varphi_3 \leq 24.9°$ and ensure that the MRD is not shifted of more than 5° for all frequencies. The simulated and measured received radiation diagrams are shown in Fig. 3.21 along with the information on the MRDs, Θ and Ψ in Tab. 3.4. The results are compliant with the expectations, showing that there is only a slight degradation in the side lobe level due to φ_2.

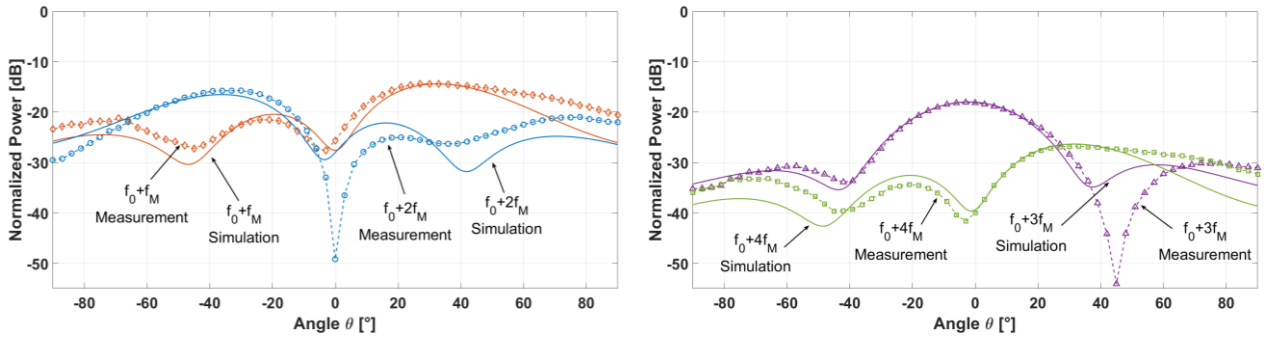

(a) (b)

Fig. 3.21: Simulated and measured Radiation Diagrams for allowed φ_2 and φ_3 values. (a) $(f_0 + f_M)$ and $(f_0 + 2f_M)$ frequencies. (b) $(f_0 + 3f_M)$ and $(f_0 + 4f_M)$ frequencies.

f	Measured θ_{max}	Simulated Θ	Simulated Ψ
$f_0 + f_M$	30°	40°	-21°
$f_0 + 2f_M$	-30°	-44.5°	17.5°
$f_0 + 3f_M$	-3°	-2.5°	73.5°
$f_0 + 4f_M$	33°	38.5°	-22.5°

Tab. 3.4: MRD θ_{max}, simulated Θ and Ψ directions at $(f_0 + hf_M)$ for allowed φ_2 and φ_3.

To conclude, in all the exposed cases the measurements have been shown to be in good agreement with the simulations in terms of MRD behaviour. The minor differences between the curves of simulations and measurements are due to the environment where they have been

carried out and to the characteristics of the single antennas. However, their impact in the overall behaviour of the TMA is small and there are no major anomalies that need to be discussed, thus confirming the developed model.

3.5. Optimization algorithm for the determination of the modulating sequences of a TMA

A difficult aspect of TMAs is the determination of the modulating sequences. In fact, there is no direct way to determine the sequence which produces a certain desired effect. Even considering a low number of antennas, it is too challenging to determine theoretically how to shape a modulating sequence to transmit in a certain direction even for a single frequency. If more frequencies are involved, then the problem is even harder. A useful tool in this case is mathematical optimization. In the literature many research groups have proposed different effective ways to choose the proper sequence for a given application: just to cite few of them, simulated annealing techniques [120], particle swarm techniques [121], [122], [123], and differential evolution algorithms [124]. In this thesis work, a simpler optimization tool has been developed in order to have the possibility to carry on tests for validation purposes. Optimization consists in using or elaborating algorithms to solve numerically a mathematical problem, which is always the minimization of a function $f(x)$, called the objective function. There exist many branches of mathematical optimization, for example Linear Optimization, where $f(x)$ is linear and Non-Linear Optimization. Usually, there is a trade-off between computational time and precision of the solution, with methods focusing more on finding the true solution of the problem but requiring a long computational time and others focusing more on finding a good enough solution in a short amount of time.

The Heuristics approach provides algorithms belonging to the second category, meaning that they find a good enough solution in a short time, without wanting to find the very best solution. The typical optimization problem is formulated as follows:

$$\begin{aligned} &\min f_m(x), m = 1, 2, \dots, M \\ &s.t. g_j(x) \leq 0, j = 1, 2, \dots, J \\ &h_i(x) = 0, i = 1, 2, \dots, I \\ &x \in \Omega \end{aligned} \tag{3.19}$$

where $f_m(x)$ are the objective functions to be minimized, $g_j(x)$ and $h_i(x)$ are inequality and equality constraints and Ω is the domain of x. If $M > 1$ then the optimization is multi-objective, while if $J = I = 0$ then the problem is unconstrained (otherwise it is constrained). The constraints are meant to bound the domains of the objective functions $f_m(x)$ and/or the solution x and are set depending on the problem. So, before choosing an appropriate algorithm, the first step is to translate our problem into an optimization problem.

Let us define the modulating sequences' problem: given a TMA with N_a antennas and for a given set of frequencies $f_0 + h_m f_M$ ($m = 1, 2, \dots, M$), find the modulating sequences c_n and $c_{i,n}$ such that the TMA has maximum radiation in the directions $\theta_{0,m}$. In other words, for each frequency we fix a maximum radiation direction (MRD) $\theta_{0,m}$ and then find the

modulating sequence causing the TMA to radiate in those directions. The next step is to define the objective function. According to the definition of our problem, we want to maximize the radiated power in $\theta_{0,m}$, which is naturally proportional to the Array Factor (AF) in the form $\left|AF_{h_m}(\theta)\right|^2$. Assuming uniform excitation of the antennas, since the AF directly depends on the modulating sequence, a good choice for $f_m(x)$ is:

$$\begin{aligned} f_m(x) &= -\left|AF_{h_m}(\theta_{0,m})\right|^2 \\ &= -\left|\sum_{n=1}^{N_a} c_n sinc(h\pi c_n) e^{-j\{h\pi(c_n+2c_{i,n})-(n-1)kD\ sin(\theta_{0,m})-\varphi_n\}}\right|^2 \\ &= -\sum_{x=1}^{N_a}\sum_{y=1}^{N_a} c_x sinc(h\pi c_x)\, c_y sinc(h\pi c_y) cos\Big(h\pi\Big(2(c_{i,x}-c_{i,y})+(c_x-c_y)\Big) \\ &\qquad -(x-y)kD\ sin(\theta_{0,m})-(\varphi_x-\varphi_y)\Big) \end{aligned} \tag{3.20}$$

which is the negative squared modulus of the AF evaluated in $\theta_{0,m}$ and where the solution vector x in our case is the vector $[c_1, \dots, c_n, c_{i,1}, \dots, c_{i,n}]$. The minus sign has been added because the objective function needs to be conventionally minimized and the amplitude terms A_n have been omitted due to the uniform excitation assumption (i.e. A_n constant). The last equality is a way to write the function as a sum of simpler cosine terms, which are more easily manageable by a calculator.

The next step is to determine the constraints. Firstly, the domain of c_n and $c_{i,n}$ must be restrained to [0; 1] since these quantities are percentages. However, it is better to bound c_n to [0.1; 0.9] because it would make no sense to keep an antenna completely off or 100% on due to the TMA being based on square wave modulations. Additionally, we fix $c_{i,1}$ to 0 as a reference, as all initial delays can be expressed in function of a reference point. In this way we have shaped the solution's domain as a convex set, which is especially useful in optimization.

Secondly, we need to set a constraint to make sure that the obtained solution actually produces the MRDs in $\theta_{0,m}$. To understand better this last point, we must consider that the chosen objective function is evaluated in $\theta_{0,m}$, so there is no control over what happens in $\theta \neq \theta_{0,m}$. This means that without this kind of constraint we could find solutions which produce the lowest possible value of $f_m(x)$ but where the MRD is not located in $\theta_{0,m}$. The described situation does not actually happen if the optimization has a single objective (i.e. $M = 1$), but must be considered if the optimization is multi-objective (i.e. $M > 1$). Therefore, the condition to ensure that the found solution gives a MRD in $\theta_{0,m}$ is to have a local maximum in $\theta_{0,m}$, which is given by

$$\frac{d\left(\left|AF_{h_m}(\theta_{0,m})\right|^2\right)}{d\theta} = 0 \tag{3.21}$$

which is the very well-known Fermat's Theorem. This constraint is an $h_i(x)$ type constraint, but it is challenging to treat numerically by calculators. In fact, what is usually done is to set a threshold ε and consider as 0 any value below ε in absolute value.

$$\left|\frac{d\left(\left|AF_{h_m}(\theta_{0,m})\right|^2\right)}{d\theta}\right| \leq \varepsilon, \qquad with\ \varepsilon \leq 1 \tag{3.22}$$

A different approach leading to a similar result is to consider the product between the derivatives evaluated in $\theta_{0,m} + \varepsilon$ and $\theta_{0,m} - \varepsilon$. If the product is negative then the derivative is 0 between $[\theta_{0,m} - \varepsilon; \theta_{0,m} + \varepsilon]$, which includes $\theta_{0,m}$.

$$\frac{d\left(\left|AF_{h_m}(\theta_{0,m} - \varepsilon)\right|^2\right)}{d\theta}\frac{d\left(\left|AF_{h_m}(\theta_{0,m} + \varepsilon)\right|^2\right)}{d\theta} \leq 0, \qquad with\ \varepsilon \leq 1 \tag{3.23}$$

However, the last approach is not the best as the constraint is non-linear, differently from (3.22).

Finally, we are ready to define the optimization problem associated to determine the modulating sequences:

$$\begin{gathered}
\min f_m(x) = -\left|AF_{h_m}(\theta_{0,m})\right|^2, m = 1, 2, \dots, M \\
x = [c_1, \dots, c_n, c_{i,1}, \dots, c_{i,n}], x \in \mathbb{R}^{N_a} \\
\\
such\ that: \\
0.1 \leq c_n \leq 0.9 \\
c_{i,n} = 0 \\
0 \leq c_{i,n} \leq 1 \\
\left|\frac{d\left(\left|AF_{h_m}(\theta_{0,m})\right|^2\right)}{d\theta}\right| \leq \varepsilon\ or\ \frac{d\left(\left|AF_{h_m}(\theta_{0,m} - \varepsilon)\right|^2\right)}{d\theta}\frac{d\left(\left|AF_{h_m}(\theta_{0,m} + \varepsilon)\right|^2\right)}{d\theta} \leq 0
\end{gathered} \tag{3.24}$$

The problem defined in (3.24) can now be solved with any Heuristic or Non-Heuristic method. In this project, I used the Python suite Pymoo [125], a free library containing various well-known Heuristic algorithms for single- or multi-objective optimization. The chosen algorithm is the Non-dominated Sorting Genetic Algorithm (NSGA-II). This algorithm provides a genetic algorithm approach mixed with a crowding distance sorting approach and is helpful for optimization problems up to 2 objectives. Its working principle follows this procedure:

- An initial population of N elements is doubled through classic genetic algorithm proceedings, i.e. population's sampling, crossover's selection, crossover and mutation. The parent generation is kept along with the offspring.

- The resulting population of 2N elements is sorted in dominance fronts. A point x_1 dominates another point x_2 if $f_m(x_1) \leq f_m(x_2)$ for all m and if $f_m(x_1) < f_m(x_2)$ for at least one m. The first dominance front is constituted by the points which are not dominated by any other point. The second front is constituted by the points which are not dominated by any other point, excluding the points of the first front. The third and following fronts are determined in the same way as the second one.
- The surviving population of N elements is selected by taking all the elements of the first dominance front, followed by all the elements of the second front and so on until a front has too many elements compared to the available slots for survival.
- The "overcrowded" front is sorted by means of a crowding distance sorting algorithm. In particular, for each point of the front the left and right neighbour define a cuboid with a perimeter whose value is associated to the point. The points are sorted following the descending order of the cuboids' perimeters. The first and last point of the front are associated with an infinite cuboid's perimeter, as one of their neighbours is assumed to be infinity.
- The remaining available slots for survival are filled with the first sorted elements of the front and the next iteration can take place.

A visual understanding of this algorithm is given in Fig. 3.22, which shows the flow of NSGA-II and a representation of the aforementioned cuboid.

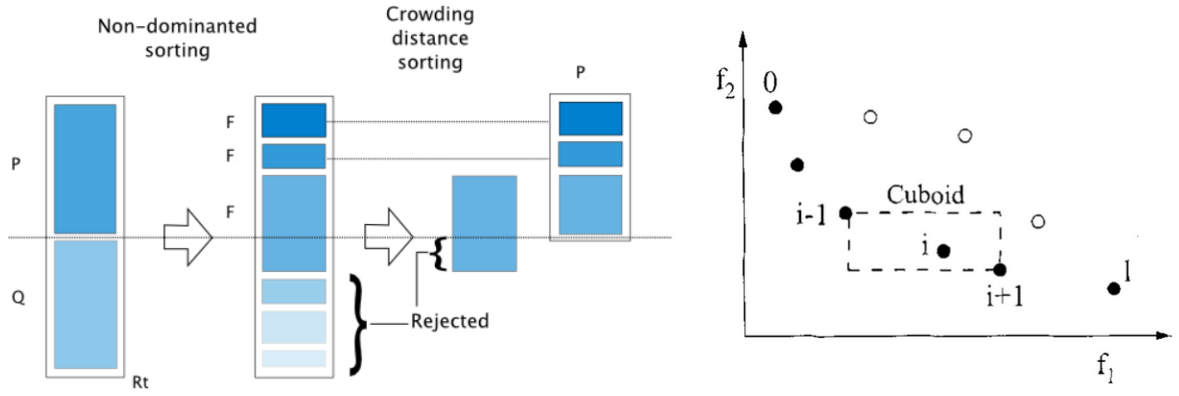

Fig. 3.22: Representation of the flow of NSGA-II algorithm and of the cuboid of the i-th point of a front (dark points) for the Crowding Distance Sorting.

The purpose of this algorithm is to heuristically search for a set of solutions belonging to the Pareto front of the problem, with the Pareto front being the set of all non-dominated points of the solutions' domain. This means that each solution of this set is no better than all the others in absolute terms for the definition of dominating point. The final choice of the best solution depends on external information, such as how important is an objective compared to the others, and is performed by a Multi-Criteria Decision Making (MCDM) algorithm. Pymoo provides a simple MCDM implementation using decomposition functions, requiring only the weights of importance of each objective function.

To test Pymoo we implemented a Python program, reported at the end of the chapter, where we considered a TMA of 4 antennas with $\lambda/2$ spacing (i.e. $kD = \pi$), frequencies of interest $f_0 + f_M$ and $f_0 + 2f_M$ and objective MRDs fixed to $\theta_{0,1} = 20°$ and $\theta_{0,2} = -40°$. Unwanted phase shifts φ_n are considered to be 0° or different from 0° in two separated scenarios. The other hyperparameters used for the algorithm are listed below:

- Initial population size: 1000.
- Initial population sampling: Integer Random Sampling.
- Crossover selection method: Tournament Selection.
- Crossover method: Simulated Binary Crossover.
- Mutation method: Polynomial Mutation.
- Termination criteria: stop after 100 generations.
- MCDM: Augmented Scalarization Function with equal weights for both objectives.

The hyperparameters of each of the previous points have not been optimized, but the obtained results are sufficiently satisfying for our testing purpose to justify the choice.

When φ_n are all 0, the algorithm outputs the set of non-dominated solutions shown in Fig. 3.23. The plot represents the performance of each solution in terms of value of the objective functions $f_{m,1}$ and $f_{m,2}$. The crossed point is the solution chosen by the MCDM algorithm, which is approximately $c_n = [35, 35, 65, 35]\%$ and $c_{i,n} = [0, 25, 25, 50]\%$. The corresponding radiation diagrams are represented in Fig. 3.24, showing that the MRDs are correctly located in 20° and -40°.

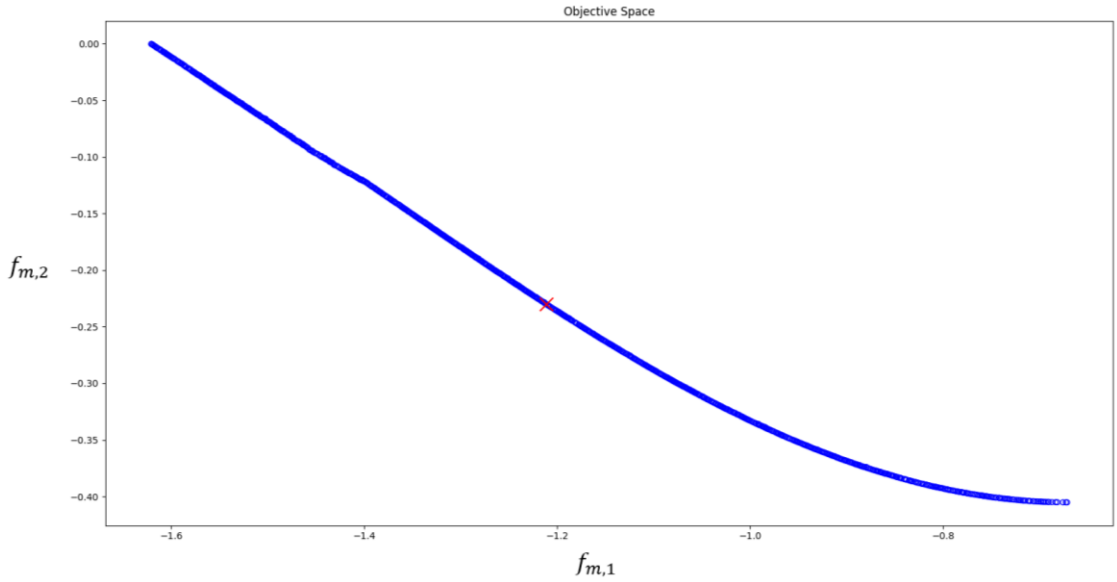

Fig. 3.23: Non-dominated solutions found by NSGA-II in the Objective Space $f_{m,1} \times f_{m,2}$. The crossed point is the solution chosen by the MCDM algorithm.

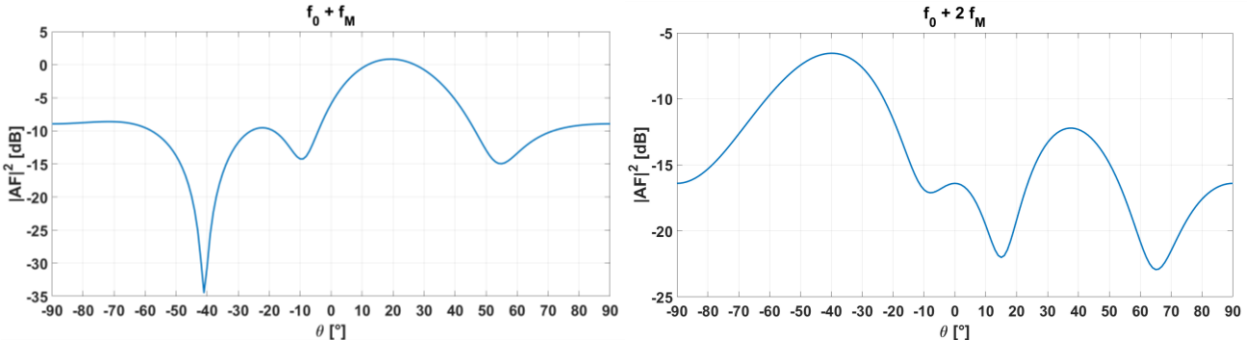

Fig. 3.24: Radiation diagrams generated by the chosen solution at the frequencies $f_0 + f_M$ and $f_0 + 2f_M$.

When non-ideal φ_n are taken into account, for example [0°, 106°, -10°, 237°], the algorithm outputs the set of non-dominated solutions shown in Fig. 3.25. Again, the crossed point being the solution chosen by the MCDM algorithm, which is approximately $c_n = [35, 65, 35, 65]\%$ and $c_{i,n} = [0, 75, 25, 75]\%$. The corresponding radiation diagrams in Fig. 3.26 show that the MRDs are correctly located in 20° and -40°. It can be noted that there is a worsening in the side lobe ratio levels of both plots. This side effect is due to the unwanted phase shifts, whose negative effects in a lot of cases can only be mitigated but not fully cancelled.

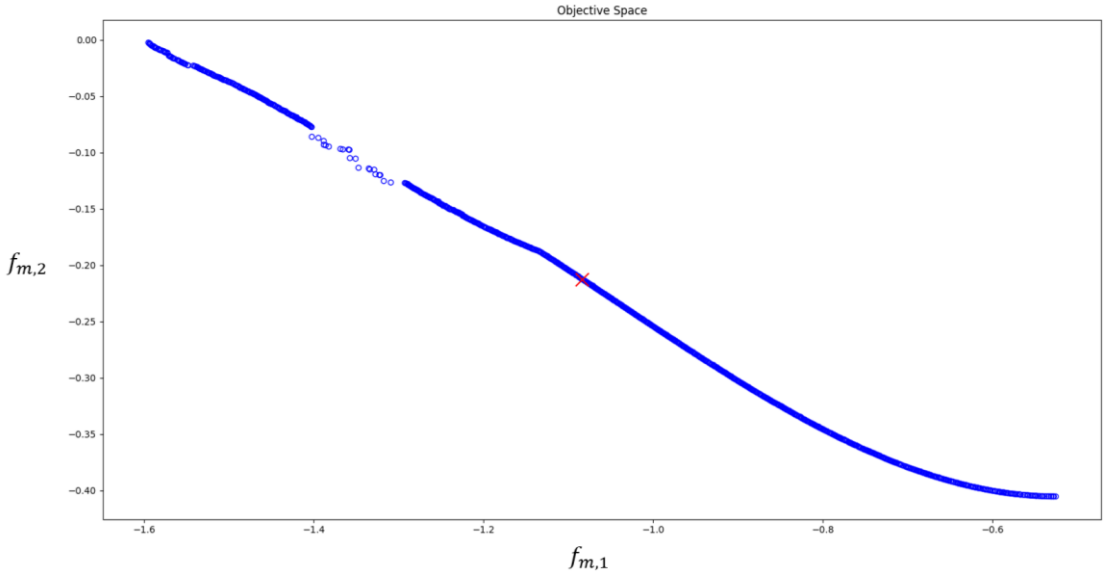

Fig. 3.25: Non-dominated solutions found by NSGA-II in the Objective Space $f_{m,1} \times f_{m,2}$. The crossed point is the solution chosen by the MCDM algorithm.

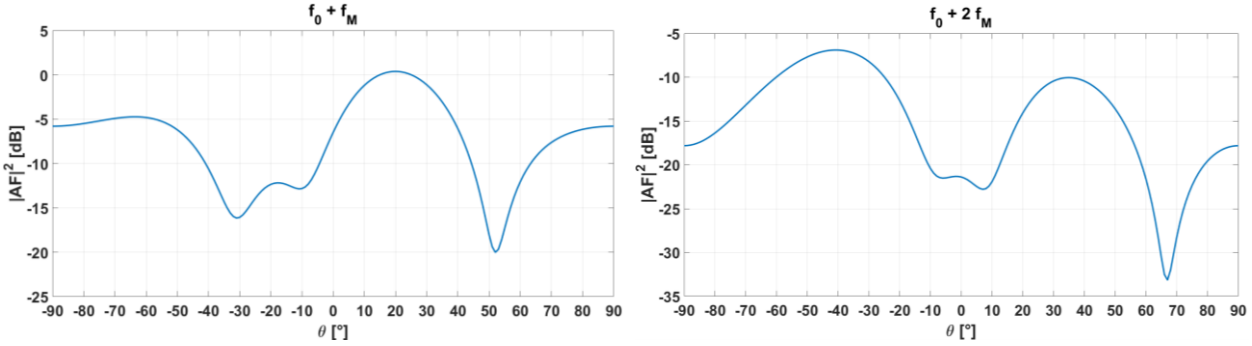

Fig. 3.26: Radiation diagrams generated by the chosen solution at the frequencies $f_0 + f_M$ and $f_0 + 2f_M$.

In conclusion, I demonstrated that the phase shifts impairments analysed in section 3.4 can be mitigated by changing the modulating sequences exploiting optimization algorithms. The analysis of section 3.4 showed that analytical solutions to TMA related problems are challenging to find. Therefore, optimization algorithms (Heuristics in particular) proved to be a powerful tool to determine the modulation sequences in TMA systems.

An implementation of the optimization algorithm NSGA-II showed good results in sequences determination and phase shifts correction in a TMA. The proposed implementation is simple in terms of constraints and meant for test purposes. More powerful algorithm

implementations exist in literature which take into account more aspects related to antenna systems, such as the Side Lobe Radiation.

3.6. Conclusions

In this chapter, I presented the concept of the RoF-TMA system along with a first realization of such system with a RoF link composed of a DFB laser, a single mode fiber and PIN photodiodes. With respect to the state of the art, this is the first time that a TMA piloted by opto-electronic devices is realized. The measurements performed on this system demonstrated that the proposed RoF-TMA system has the same behaviour of a purely RF TMA system (i.e. composed of only electrical components). In particular, the results showed that the error between the maximum radiation direction of a RoF-TMA and of a purely RF TMA is less than 7°.

It was shown that the presence of unwanted phase shifts in the antenna currents impairs the functioning of the system. A full analysis of the phase shifts effects on a 3-TMA system showed that it is possible to determine a tolerance interval for each phase shift which ensures the system to behave correctly. At the same time, the problem itself proved to be challenging to solve even for an array composed of few elements. The found results were validated through measurements in different scenarios characterized by phase shifts inside or outside the interval of tolerance. In particular, in the case of a 3-TMA where all maximum radiation directions are within $[-35°, 35°]$, the phase shifts φ_2 and φ_3 needed to be within the intervals $[\varphi_3/2 - 37°, \varphi_3/2 + 37°]$ and $[-25.2°, 24.9°]$ to maintain the beams at less than 5° from their original position. Finally, an optimization approach has been presented to determine the modulating sequences of a TMA and to tackle the phase shifts detrimental effects. A test program implementing the Heuristic algorithm NSGA-II has been developed, showing positive results on both sequences determination and phase shifts mitigation.

Chapter 4: RoF system and components modelling

4.1. Introduction

In this chapter, the behaviour and modelling of the RoF link's components is discussed, focusing especially on lasers and Heterojunction Phototransistors (HPTs). Firstly, we introduce our approach to RoF links modelling, followed by the presentation of a large signal behavioural model for lasers. This model takes into account the main non-linearities of a laser, it works for a single frequency and is effective for its simplicity. Several models have been developed in the last decades to describe the RoF links behaviour [126], [127]. Due to the similarities between the large signal behaviour of both lasers (e.g., VCSEL LIV curves [128], [129]) and power amplifiers (e.g., amplifier transfer function), some models have been developed, based on the existing literature about behavioural modelling of power amplifiers [130]-[138].

Finally, the last sections of the chapter focus on the analysis and modelling of the parameters of the HPT that allow it to be used as a suitable switching component for the TMA. In particular, we defined the On-Off Ratio parameter to evaluate the performances of the HPT as a switch.

The results of this chapter led to the publication of a journal paper [139].

4.2. RoF link components Modelling

4.2.1. Model of the RoF system

Modelling the behaviour of the components of a system is of fundamental importance as it allows to simulate performances of the system considering the impact of parameters on the system and to facilitate the optimisation of the system. After a validation of the developed models based on measurements, these models can be exploited in other research works especially involving simulations. A classic way to model an unknown component is to treat it as an N-port device and characterize its behaviour through the Scattering Matrix *S*. The parameters of the Scattering Matrix provide an exhaustive description of the behaviour of an N-port in function of the frequency and usually the parameters of most interest are the transmission coefficients, as the reflection coefficients need to be ideally zero in most devices. However, the Scattering Matrix approach fails if non-linear effects need to be considered, since the S parameters allow only a linear modelling of the device. A different approach is required when non-linearities necessary to model optical and optoelectronic devices with high precision are needed. For this project we adopt the behavioural model approach. Behavioural models are used to describe a device input-output behaviour with non-linear equations depending both on parameters related to the device's nature (e.g. the saturation current of a laser) and on parameters specific to the model.

The system to model is the RoF link, composed of a laser, an optical fiber and a photodetector. A first issue is in how to represent this kind of devices: since a port is

electrically defined, the optical nature of the RoF does not allow to directly represent lasers, optical fibers and photodetectors with electrical N-ports. Intuitively, all the three of them should be represented by 2-ports, as they have a single input and output for the signal. The adopted solution is to convert the optical power envelope, representing the information carried by the light, into a fictitious electrical current I_{opt} through a conversion factor $\alpha = 1\ A/W$, such that $I_{opt} = \alpha P_{opt}$. This is possible only because the behaviour of the envelope optical power follows the one of the laser's modulating current. In this way, an electrical port can be effectively associated to an optical device and the system will result in a cascade of quadrupoles, as recalled in Fig. 4.1.

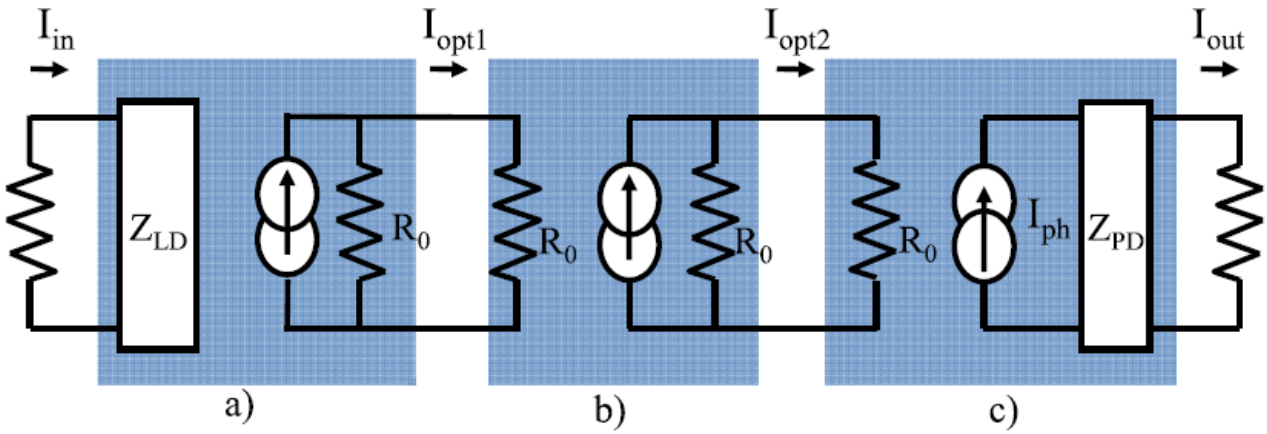

Fig. 4.1: Block scheme of the RoF link. Block (a) is the laser, block (b) the fiber and block (c) the photodetector.

The block scheme follows this logic: the quadrupole (a), representing the laser, has a real electric current I_{in} provided by an external generator as the input current and an internal input impedance Z_{LD} equal to the real impedance of the laser. The output current is the fictitious I_{opt1}, generated by an internal current generator with parallel impedance R_0 and equal to αP_{opt1}. Quadrupole (b) represents the optical fiber and has I_{opt1} as the input current and an input impedance R_0 matched to the impedance of the internal current generator of (a). Following the same logic, the second fictitious current I_{opt2} is generated and passed to the photodetector, the quadrupole (c). The current provided by the photodetector's internal current generator is equal to the real photocurrent I_{ph} and the parallel impedance of the generator equals the characteristic impedance of the photodetector Z_{PD}. Finally, I_{out} flows to the load impedance at the end of the cascade. In this representation of RoF links, behavioural models find their application in defining each quadrupole's input-output dependence.

4.2.2. Laser behaviour modelling

The large signal model of a laser must shape accurately the behaviour of the laser with different biasing, while taking into account the non-linear (NL) effects of the device. In particular, the main non-linearities that need to be considered are the 1 dB compression point (P_{1dB}) and the third order intercept point (IP_3), which both depends on frequency. Before giving the definitions of these two quantities, any device's behaviour may be defined by its input-output power relationship, which is modelled as the following polynomial:

$$P_{out} = G_{lin}(f)P_{in} + \sum_{n=2}^{\infty} G_{NLn}(f)P_{in}^{n} \tag{4.1}$$

where G_{lin} is the linear gain, G_{NLn} is the gain associated with n-th order non-linearities and both quantities are dependent on frequency. In general, if P_{in} is low enough the behaviour of the device is in its linear regime since all the NL terms are negligible, while with higher P_{in} levels the device is in its NL regime, which is usually a saturation regime. In most cases, low order terms, such as quadratic and cubic non-linearities, have greater impact than higher order terms.

The definitions of P_{1dB} and IP_3 involve two different situations. For P_{1dB}, let us consider a Device Under Test (DUT) fed with a single tone frequency f at different power levels $[P_{min};\ P_{max}]$ and monitor the output power at the same input frequency, as shown in Fig. 4.2. At low P_{in}, the behaviour of the DUT is linear and its gain is equal to G_{lin}. At high P_{in}, the gain is no more constant and starts decreasing. The P_{1dB} is defined as the point for which the gain $P_{out} - P_{in}$ is 1 dB less than the linear gain G_{lin}. P_{in} and P_{out} are respectively called Input P_{1dB} (IP_{1dB}) and Output P_{1dB} (OP_{1dB}) at frequency f.

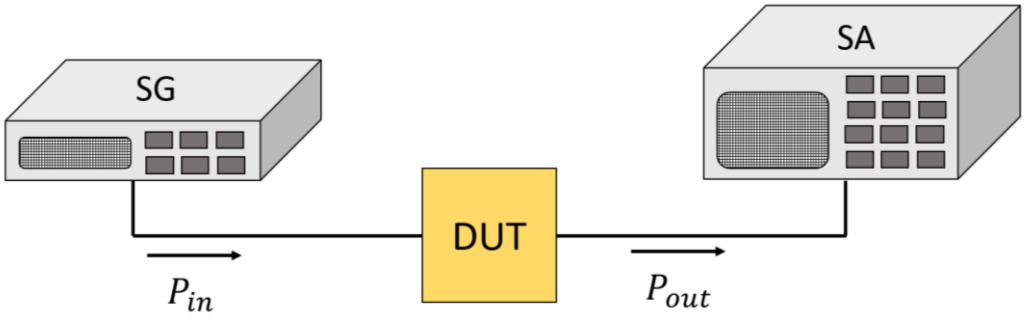

Fig. 4.2: Set-up for measuring P_{1dB} and IP_3. P_{in} has a single or double frequency component depending on the quantity to measure.

Regarding IP_3, let us consider a DUT fed with two near frequency tones f_1 and f_2 with equal power levels in the range $[P_{min};\ P_{max}]$ and monitor the output power at frequencies f_1, f_2, $2f_1 - f_2$ and $2f_2 - f_1$ as shown in Fig. 4.3. These last two frequencies are the so-called third order intermodulation distortion (IMD_3) frequencies, as they are involved in cubic non-linear distortion. Considering the power associated to the input signal $I\cos(2\pi f_1 t) + I\cos(2\pi f_2 t)$, it is easy to compute that $G_{NL3}P_{in}^3$ has components in the IMD_3 frequencies. Finally, f_1 and f_2 are close enough that the terms G_{lin} and G_{NLn} associated to the 4 frequencies of interest have the same value. At low P_{in}, the DUT behaves linearly and P_{out} is observed only at f_1 and f_2, while at $2f_1 - f_2$ and $2f_2 - f_1$ it is negligibly low. At higher P_{in}, we observe non-negligible output power also at the IMD_3 frequencies due to cubic NL effects. The IP_3 is defined as the interception point between the linear curve $G_{lin}P_{in}$ and the cubic curve $|G_{NL3}|P_{in}^3$. This point is always found mathematically by prolonging the two curves expressed in dB scale, as shown in Fig. 4.3. It is physically impossible to measure IP_3 because raising P_{in} too much causes higher order NL effects to appear and the DUT could be permanently damaged as a consequence. The P_{in} and P_{out} associated to IP_3 are respectively called Input IP_3 (IIP_3) and Output IP_3 (OIP_3) at frequency f_1.

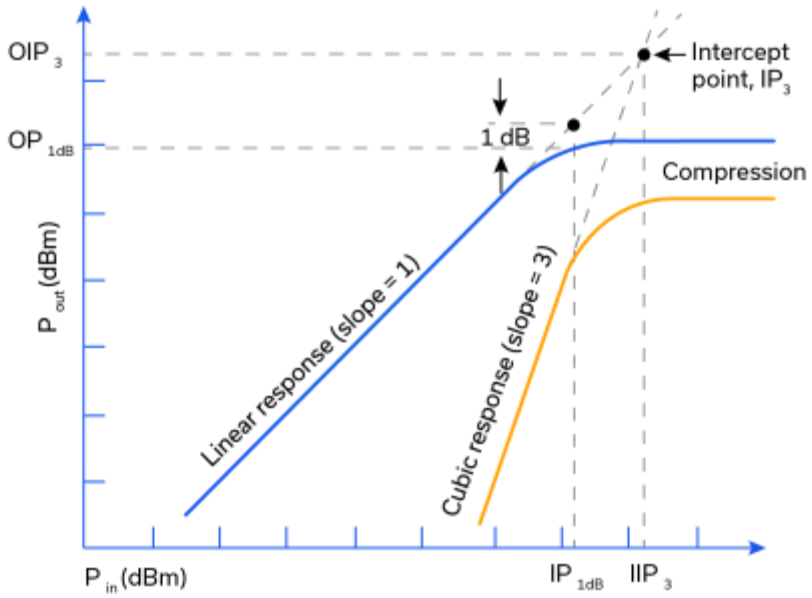

Fig. 4.3: Representation of P_{1dB} and IP_3 on a P_{in} vs P_{out} plot of a DUT. The linear and cubic responses are represented in dB scale, so that they both behave linearly.

The behaviour of a laser is mainly characterized by 3 operating regions, depending on the biasing: linear region, knee region and saturation region, represented in Fig. 4.4. The linear region represents the ideal behaviour of the laser, while the saturation region is where the laser experiences full compression. The knee region represents the junction between the linear one and the saturation one and is knee shaped.

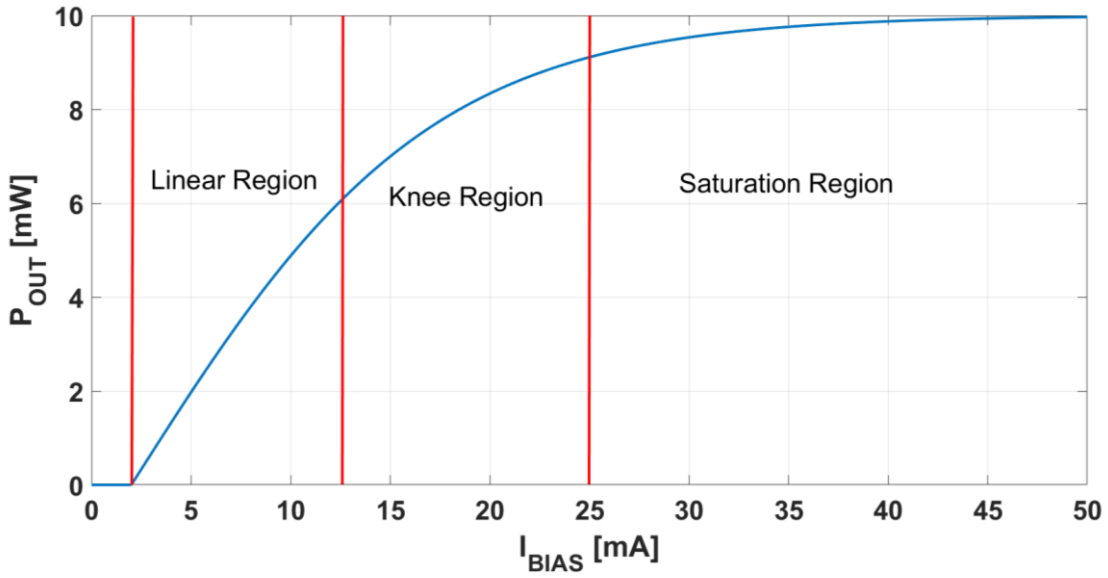

Fig. 4.4: Representation of the working regions of a laser: linear, knee and saturation.

Over the years, multiple behavioural models of the laser have been conceived with different degrees of complexity. For example, the hyperbolic tangent model [140] shapes the output response of the laser with a tanh function, which is very simple and straightforward, but it is very limited in shaping adequately the nonlinearities of the laser.

The model we considered in this project is the Improved Cann Model [141], which was developed by Alfred J. Cann as an improvement of its previous Cann Model [142]. In particular, the improvement aimed to solve problems related to the modelling of two-tone intermodulation. The model expresses the laser's output current I_{opt} in function of its input current I_{in} through the following:

$$I_{opt} = \frac{I_{S,LD}}{k} ln\left(\frac{1 + e^{k\left(\frac{g_{LD} I_{in}}{I_{S,LD}} + 1\right)}}{1 + e^{k\left(\frac{g_{LD} I_{in}}{I_{S,LD}} - 1\right)}}\right) - I_{S,LD} \tag{4.2}$$

where $I_{S,LD}$ is the saturation current of the laser, g_{LD} is the laser model gain and k is the knee factor, a design parameter for shaping the knee region of the laser. Both $I_{S,LD}$ and g_{LD} can be determined experimentally, as g_{LD} can be substituted by the current laser's linear gain (i.e. the slope efficiency) with good approximation. However, it is apparently impossible to determine the k factor without a heuristic approach. We proceed to show that there actually is a link between the design parameters and the nonlinear quantities P_{1dB} and IP_3. For this purpose, we start by the Taylor expansion of (4.2) up to the third degree, given by:

$$I_{opt} = \sum_{n=1}^{\infty} TC_n \frac{I_{in}^n}{n!} \tag{4.3a}$$

$$TC_1 = \left.\frac{dI_{opt}}{dI_{in}}\right|_{I_{in}=0} = g_{LD} \frac{sinh(k)}{1 + cosh(k)} = S_{LD} \tag{4.3b}$$

$$TC_2 = \left.\frac{d^2 I_{opt}}{dI_{in}^2}\right|_{I_{in}=0} = 0 \tag{4.3c}$$

$$TC_3 = \left.\frac{d^3 I_{opt}}{dI_{in}^3}\right|_{I_{in}=0} = -\frac{k^2 g_{LD}^3}{I_{S,LD}^2} \frac{sinh(k)}{(1 + cosh(k))^2} = -\frac{k^2 S_{LD}^3}{I_{S,LD}^2} \frac{1 + cosh(k)}{(sinh(k))^2} \tag{4.3d}$$

with TC_n being the n-th Taylor coefficient of the series. The second order term TC_2 is null due to (4.2) being an odd function, while TC_1 is equal to the current linear gain of the laser, defined as the slope efficiency S_{LD} (i.e. $I_{opt} = S_{LD} I_{in}$, but $P_{opt} = S_{LD}^2 P_{in}$). It can be noted that if $k > 3$ then $g_{LD} \approx S_{LD}$, thus confirming that g_{LD} can be well approximated by S_{LD}.

The next step is to consider IP_3: as previously said, to determine this quantity the DUT is fed with two equally powered tones f_1 and f_2, such that $I_{in}(t) = I\, cos(2\pi f_1 t) + I\, cos(2\pi f_2 t)$, and the power levels at the IMD_3 frequencies $2f_1 - f_2$ and $2f_2 - f_1$ are evaluated along with the power levels at f_1 and f_2. At linear regime, the theoretical power levels at these frequencies have the following expression:

$$P_{out}(f_1) = \langle I_{opt}^2(t, f_1) \rangle = \langle \left(TC_1\, I\, cos(2\pi f_1 t)\right)^2 \rangle = \frac{1}{2} S_{LD}^2 I^2 \tag{4.4a}$$

$$P_{out}(IMD_3) = \langle I_{opt}^2(t, 2f_1 - f_2)\rangle = \langle \left(TC_3 \ \frac{3}{4} I^3 \ cos(2\pi(2f_1 - f_2)t) \right)^2 \rangle = \\ = \frac{9}{32} \frac{k^4 S_{LD}^6}{I_{S,LD}^4} \frac{(1 + cosh(k))^2}{sinh^4(k)} I^6 \tag{4.4b}$$

where $\langle \cdot \rangle$ denotes the averaging operator (i.e. $\langle cos^2(\omega t)\rangle = 0.5$) and $I_{opt}(t, f)$ is the component of $I_{opt}(t)$ at the frequency f. The expression of $I_{opt}(t, 2f_1 - f_2)$ in (4.4b) is found by computing the term $I_{in}^3(t)$ and separating its frequency components. I highlight the resistance term is missing in the expression of the powers, following the well-known convention for signal powers. The IP_3 is defined as the $(P_{in},\ P_{out})$ point for which (4.4a) is equal to (4.4b) and its coordinates are referred as IIP_3 and OIP_3. By equalling (4.4a) and (4.4b) and considering that $IIP_3 = P_{in} = 0.5\, I^2$ it is possible to isolate $I_{S,LD}$

$$I_{S,LD} = k g_{LD} \sqrt{\frac{3}{2} \cdot \frac{IIP_3}{1 + cosh(k)}} \tag{4.5}$$

This shows that it is possible to choose the model's parameters based on the knowledge of nonlinear effects. For instance, S_{LD} is always found on the datasheet and IIP_3 can be measured experimentally, meaning that Eq. (4.5) links $I_{S,LD}$ and k.

Another important expression can be derived by considering the 1 dB compression point P_{1dB}. Recalling its definition, the P_{1dB} is the $(P_{in},\ P_{out})$ point for which the gain associated is 1 dB less than the linear gain nominal value and its coordinates are referred as IP_{1dB} and OP_{1dB}. To determine P_{1dB}, a single tone f with tunable power is sent through the DUT and the received power is measured at the same frequency. The gain is then computed so that the P_{1dB} is easily found. Theoretically, the P_{1dB} is such that:

$$P_{out}^{dB} = P_{in}^{dB} + G_{lin}^{dB} - 1 \rightarrow OP_{1dB}^{dB} = IP_{1dB}^{dB} + G_{lin}^{dB} - 1 \tag{4.6a}$$

$$P_{out} = OP_{1dB} = IP_{1dB} G_{lin} 10^{-\frac{1}{10}} = IP_{1dB}\, S_{LD}^2 10^{-\frac{1}{10}} \tag{4.6b}$$

The two equations are the same expression, the former in dB scale (Eq. (4.6a)) and the latter in linear units (Eq. (4.6b)). The linear gain is equal to S_{LD}^2, since the slope efficiency is in fact the current gain. The next step is to substitute to P_{out} the expression $0.5\, I_{out}^2$, with $I_{out} = I_{opt}$ from (4.2), and to substitute (4.3b) and (4.5) to g_{LD} and S_{LD} respectively. This leads to

$$ln\left(\frac{1 + e^{\sqrt{\frac{4IP_{1dB}}{3\ IIP_3}(1+\cosh(k))} + k}}{1 + e^{\sqrt{\frac{4IP_{1dB}}{3\ IIP_3}(1+\cosh(k))} - k}} \right) - k = \sqrt{\frac{4}{3(1 - \cosh(k))} \frac{IP_{1dB}}{IIP_3}} 10^{-1/20} \tag{4.7}$$

Equation (4.7) depends only on k and on the ratio between IP_{1dB} and IIP_3. We can furtherly prove the dependence of k on IP_{1dB}/IIP_3 with numerical simulations in Matlab. Let us

arbitrarily fix S_{LD}, k and IIP_3 (so that $I_{S,LD}$ is fixed from (4.5)), find numerically P_{out} exploiting the Improved Cann Model (4.2) and extract the corresponding IP_{1dB} values, shown in Fig. 4.5. The curves are obtained considering an S_{LD} of 0.31 W/A.

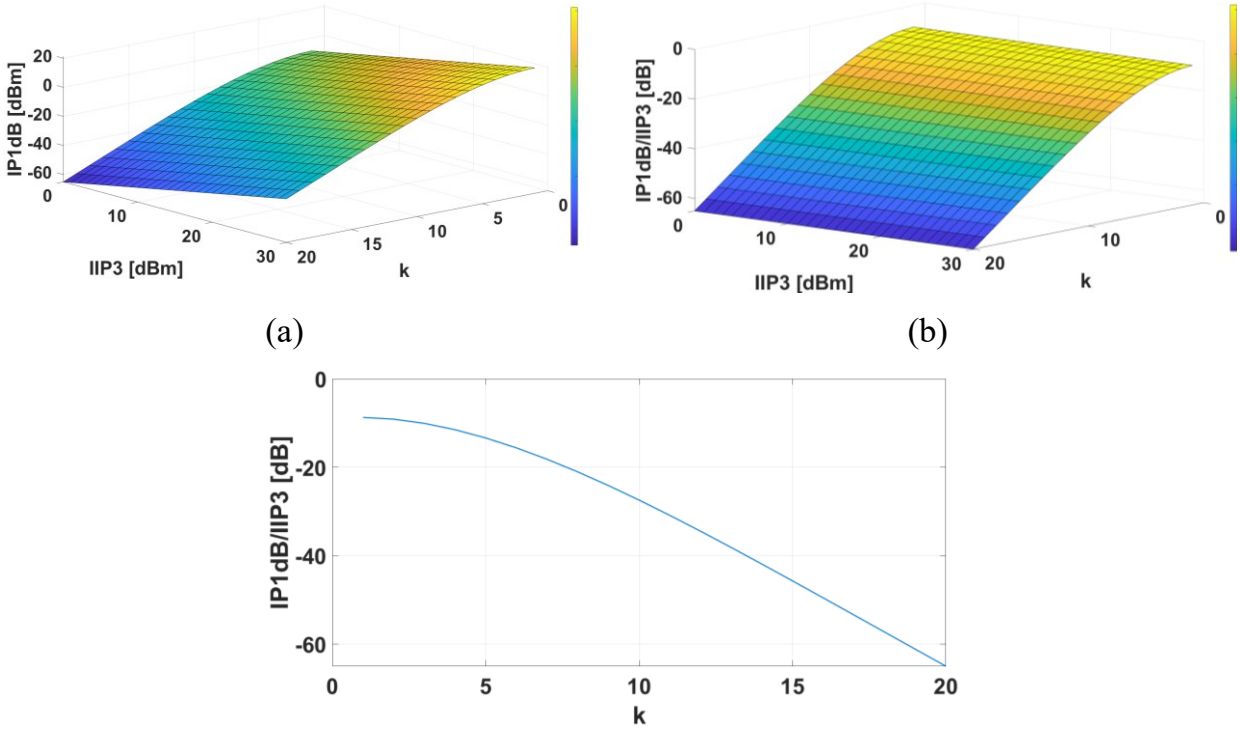

Fig. 4.5: (a) IP_{1dB} in function of k and IIP_3. (b) $\frac{IP_{1dB}}{IIP_3}$ in function of k and IIP_3. (c) $\frac{IP_{1dB}}{IIP_3}$ in function of k, obtained with a fitting polynomial.

The results show the following: the surface in Fig. 4.5(a) represents the values of IP_{1dB} in function of k and IIP_3, while the surface in Fig. 4.5(b) shows the values of $\frac{IP_{1dB}}{IIP_3}$ in function of k. The surface in Fig. 4.5(b) is independent of IIP_3, since its profile is a constant curve, shown in Fig. 4.5(c). However, isolating k from (4.7) is rather challenging and the best choice is to fit the numerically found curve with a polynomial, like the following

$$\left.\frac{IP_{1dB}}{IIP_3}\right|_{dB} = -1.484\,10^{-4}k^4 + 1.166\,10^{-2}k^3 - 0.3414k^2 + 0.5478k - 8.985 \qquad (4.8)$$

With (4.8) the model is complete, because all the parameters of the Improved Cann Model (4.2) are linked to the measurable quantities IP_{1dB}, IIP_3 and S_{LD} through (4.3b), (4.5) and (4.8). The model has been validated on ADS software, by Keysight, as shown in Fig. 4.6.

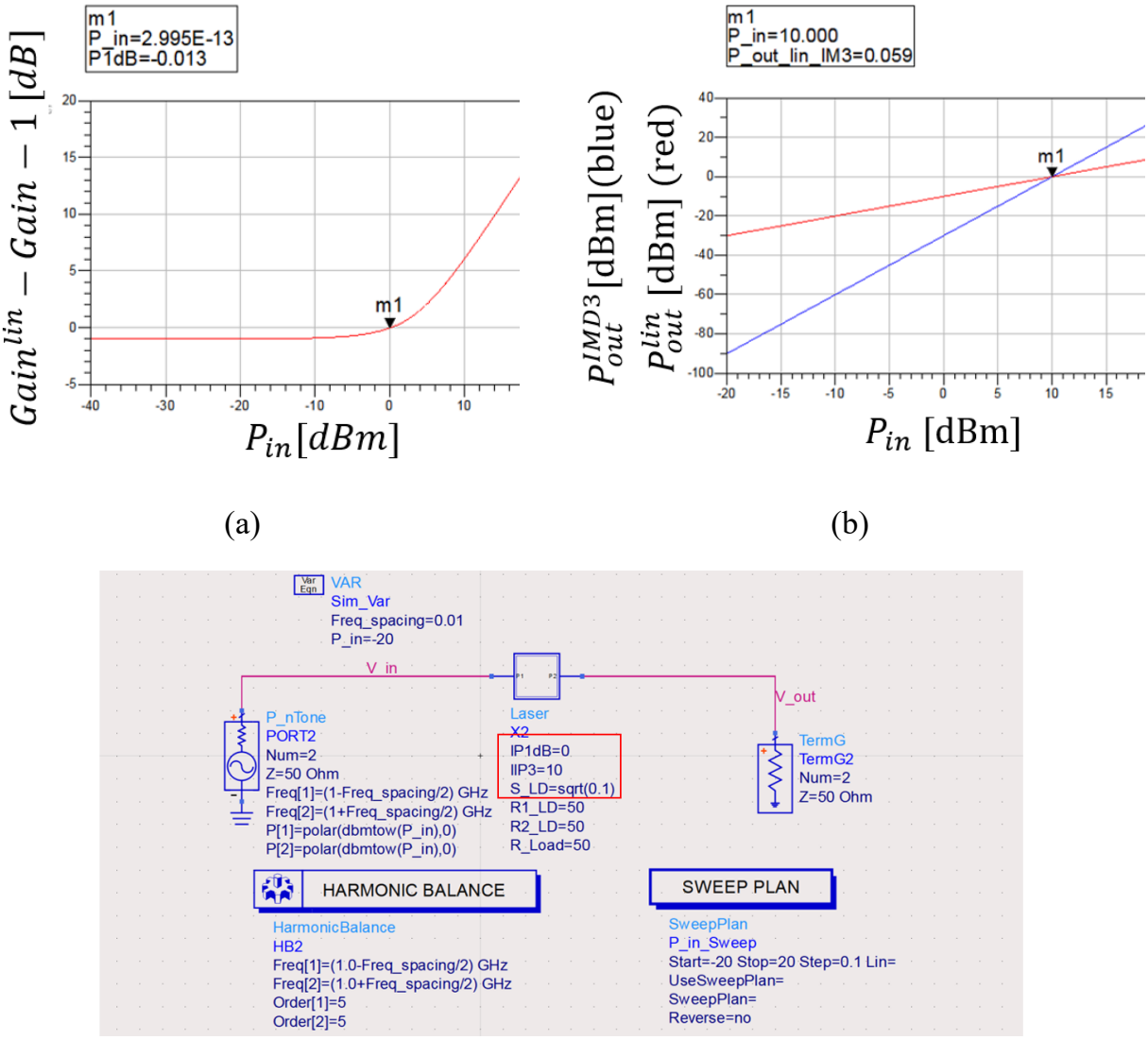

Fig. 4.6: (a) function $Gain_{linear} - Gain - 1$ with the P_{1dB} point highlighted by the marker. (b) output linear power (red line) and IMD_3 output power (blue line) with the IP_3 point highlighted by the marker. (c) ADS schematic of the laser model program.

In the simulation, the laser is modelled with a custom block with the structure of the quadrupole in Fig. 4.1. Its parameters include the input, output and load impedances, but the most important are IP_{1dB}, IIP_3 and S_{LD}, as shown in Fig. 4.6(c). The corresponding parameter values for the curves in Fig. 4.6(a) and Fig. 4.6(b) are fixed to $IP_{1dB} = 0$ dBm, $IIP_3 = 10$ dBm and $S_{LD} = \sqrt{0.1}$ W/A respectively. The output of the laser block implements (4.2), with the model parameters g_{LD} and k derived from the values of IP_{1dB} and IIP_3. Lastly, the block is fed by a generator block with input power varying from -20 dBm to 20 dBm and terminates on a 50 Ω load block. Two different simulations are run to check numerically the location of P_{1dB} and IP_3, shown in Fig. 4.6(a) and Fig. 4.6(b). In particular, Fig. 4.6(a) shows the curve $G_{dB}^{lin} - G_{dB} - 1$, where G_{dB}^{lin} is the linear gain g_{LD} and G_{dB} is the gain $P_{out}^{dB} - P_{in}^{dB}$. In this way the P_{1dB} point is found when the curve equals 0, which happens at $P_{in}^{dB} = IP_{1dB} = 0$ dB. Fig. 4.6(b) shows the behaviour of the output linear power and of the output power related to

IMD_3. IP_3 is found by definition in the intersection between these two curves, which happens at $P_{in}^{dB} = IIP_3 = 10$ dB. The markers show that both NL points are located exactly at the IP_{1dB} and IIP_3 points defined in the model block. This is indicative of the fact that the developed model behaves as we foresaw, thus validating the exposed results.

4.3. HPT Modelling

One of the main interests of this PhD project is to use advantageously HPTs in the proposed RoF-TMA system. While photodiodes have a straightforward behaviour, HPTs are characterized by multiple modes of employment and offer a potentially higher degree of flexibility. In this section we analyse and measure the performances of HPTs to adapt them as photodetectors in our system.

As mentioned in chapter 1, the structure of an HPT follows the same principle of an HBT of type npn, with the addition of an optical window at the base level, responsible for converting the light into a current. Like an HBT, the 3 main topological mode of employment are Common Emitter (CE), Common Base (CB) and Common Collector (CC). In this project, we chose to use the HPT CE configuration, acting as a voltage amplifier with high gain current due to the transistor effect. The amplified output current is higher compared to the current that a photodiode with the same optical window dimension would output. A fundamental aspect is that by changing the Base-Emitter voltage V_{be}, the HPT behaves differently. In particular, assuming $V_{bc} > 0\ V$:

- If $V_{be} = 0\ V$, the HPT operates in Photodiode (PD) mode. The Base and the Emitter are at the same voltage, meaning that only one of the two junctions composing the HPT is biased and the device behaves as a photodiode.
- If $V_{be} > 0\ V$, the HPT operates in 3 Terminals (3T) mode. In this case, both junctions are biased and the HPT behaves as a transistor in its Active or Saturation region depending on the biasing on each junction. For his reason the 3T mode is also referred as Transistor mode.

The two presented modes are characterized by different gains, in particular the PD mode has a lower gain than the 3T mode. The switching action, a condition of necessity for that the TMA can be tuned, is done by the HPT by modulating its Base-Emitter voltage V_{be}. Another important aspect to consider is that in CE configuration the output voltage phase is shifted of 180°. So, it is necessary to input a V_{be} modulating sequence opportunely phase shifted, as illustrated in Fig. 4.7.

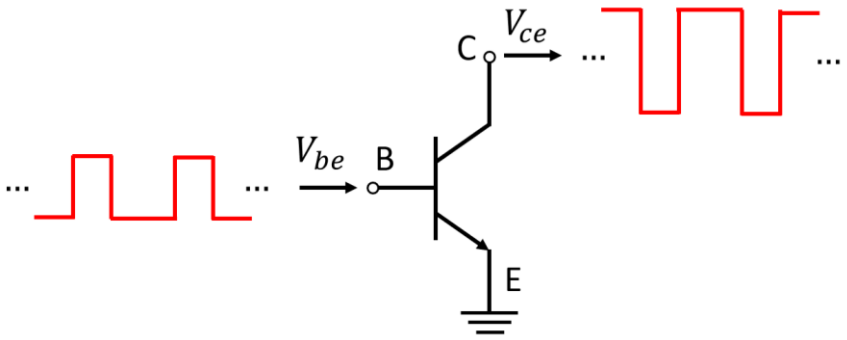

Fig. 4.7: HBT CE configuration input V_{be}-output V_{ce} representation.

It is clear that TMA modulation in HPTs is achievable by modulating V_{be}, however the HPT is not a perfect switch. In fact, the switching is between a lower and higher level rather than 0 and 1, so we want to quantify the impact of these levels on the system's performances.

Let us consider the TMA field Eq.(3.1). In this formula, the switches are assumed to be ideal, so that the imposed square wave modulation on the field varies between 0 and A_n.To be noted that $U_n(t)$ and A_n are unitless, as the units of $E(\theta,t)$ are in the term $E_0(\theta)$. Now if we consider a general modulating sequence ranging from a low positive level A_n^{OFF} to a high level A_n^{ON}, then Eq. (3.1) becomes:

$$E(\theta,t) = E_0(\theta)e^{j2\pi f_0 t}\sum_{n=1}^{N_a}(U_n(t)(A_n^{ON} - A_n^{OFF}) + A_n^{OFF})e^{j\varphi_n}e^{jk(n-1)d\,sin(\theta)} \tag{4.9}$$

where in this case $U_n(t)$ is multiplied by $A_n^{ON} - A_n^{OFF}$. Considering only the Array Factors $AF_h(\theta)$, we can easily find that:

$$AF_h(\theta) = \sum_{n=1}^{N_a}(A_n^{ON} - A_n^{OFF})e^{j\varphi_n}c_n sinc(h\pi c_n)e^{-jh\pi(c_n+2c_{i,n})}e^{jk(n-1)d\,sin(\theta)}$$
$$AF_0(\theta) = \sum_{n=1}^{N_a}A_n^{ON}e^{j\varphi_n}c_n e^{jk(n-1)d\,sin(\theta)} \tag{4.10}$$

The first equation in (4.12) refers to the case $h \neq 0$, while the second one to the case $h = 0$. Since the power emitted at each frequency $f_0 + hf_M$ is proportional to $|AF_h(\theta)|^2$, this result shows that the greater the difference $A_n^{ON} - A_n^{OFF}$ is, the greater the power associated. Let us now assume that all amplitudes are the same for each antenna (i.e. $A_n^{ON} = A_{ON}$ and $A_n^{OFF} = A_{OFF}$ for each n) and that the high level A_{ON} is fixed. By analysing (4.10) it is clear that the highest power available at every frequency corresponds to $A_n^{OFF} = 0$, which is the case shown in chapter 3, in (3.7). To compare these two studied cases, we introduce the On-Off Ratio (OOR), defined as the ratio between high and low level:

$$OOR = \frac{A_{ON}}{A_{OFF}} \tag{4.11}$$

Based on the observation done before, the highest output power is achieved with an infinite On-Off Ratio (i.e. $A_{OFF} = 0$), while the lowest power corresponds to $OOR = 1$ (i.e. $A_{OFF} = A_{ON}$). The aim is to compare the ideal $OOR = \infty$ case with the non-ideal one to establish a quality threshold for the modulation sequence. The ratio of the power output at $OOR = \infty$ and the power output at $OOR < \infty$ is then:

$$\frac{P_{OOR=\infty}}{P_{OOR<\infty}} = \frac{|A_{ON}|^2}{|(A_{ON} - A_{OFF})|^2} = \frac{|OOR|^2}{|OOR - 1|^2} \tag{4.12}$$

Equation (4.12) is meaningful as it depends only on the OOR. The trend of this ratio is represented in Fig. 4.8. From this curve we note that the 3 dB point corresponds to an OOR of 5.33 dB. This means that if a modulating sequence has an OOR of at least 5.33 dB, then

the TMA output power will be at most 3 dB less than the power output by an ideal switch. In the same manner, an OOR greater than 10 dB means that the TMA output power difference between an ideal and a non-ideal switch is less than 1 dB.

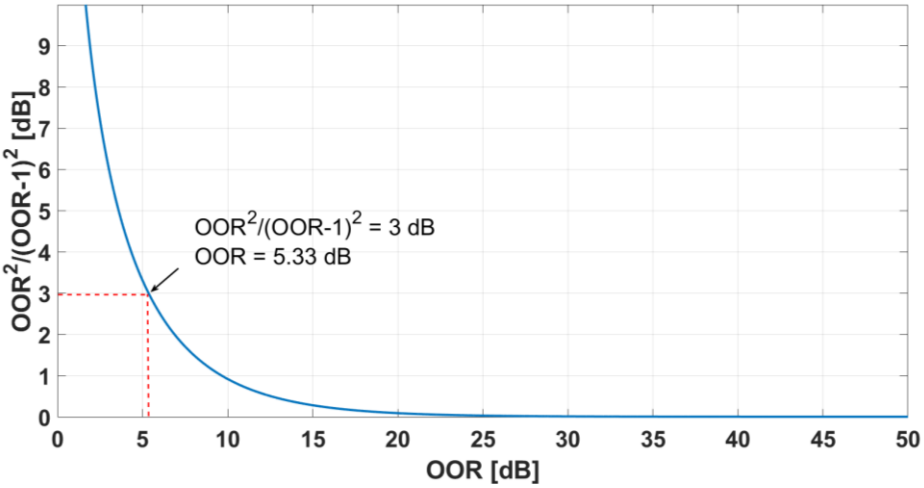

Fig. 4.8: Trend of equation (3.12).

Fixing the quality threshold of Eq. (4.12) to 3 dB, we conclude that the HPT is suitable for TMA applications if it has an OOR of at least 5.33 dB. In particular, the OOR of the HPT is the ratio between its gain in 3T mode and its gain in PD mode. However, these gains depend on frequency, thus it is necessary to characterize the HPT to find its range of work.

4.4. Conclusion

In this chapter I presented a laser behavioural model for the characterization of the laser's non-linearities at a single frequency. Compared to other solutions, the proposed model distinguishes itself for its simplicity in both formulation and number of parameters, requiring only the quantities IP_{1dB}, IIP_3 and S_{LD} to be known. This is advantageous in terms of simulation time, as a simpler model is faster. The effectiveness of the proposed model was proved through both simulations on ADS and measurements performed for the work [139].

I then showed an analytical model for the HPTs as switching elements of a TMA system. The model proved that any device switching between two states with a minimum On-Off Ratio of 5.33 dB is suitable for TMA applications. This result established the main parameter to evaluate in the characterization of HPTs presented in chapter 5.

Chapter 5: HPT design, characterization and packaging

5.1. Introduction

In this chapter, the design, characterization and packaging of the HPTs are highlighted. Firstly, the design rules and the fabrication process of HPTs are explained. Then, the set-ups for the characterization of HPTs in both frequency and time domain are presented along with the results. The measured performances are compared to the requirements of chapter 4 and the best HPT for TMA applications is chosen accordingly.

Finally, the realization of the PCB for the packaging of the HPTs for the RoF-TMA system is presented, with a description of all the steps taken. The last section shows the perspectives on the characterization and the measurements that will be performed on the RoF-TMA prototype employing the packaged HPTs.

The results of this chapter have been presented in three national conferences [143], [144] and [145].

5.2. Design of HPT and layout

In this chapter, the characteristics and the mode of employment of the HPT are described and highlighted. The structure of an HPT follows the same principle of a Heterojunction Bipolar Transistor (HBT) of type npn, with the addition of an optical window at the base level, responsible for converting the light into a current. In the proposed project, the HPT, realised in SG13S technology described in detail in chapter 2, is employed in Common Emitter configuration. As the HBT counterpart, when the HPT is employed in Common Emitter configuration, the transistor effect takes place and the output current coming from the Collector is amplified. The amplification effect is considered with respect to the current that a photodiode with the same optical window dimension would deliver.

The ESYCOM lab has an extensive knowledge and history in the development of SiGe HPT. They were developed into Atmel, Telefunken and then IHP Microelectronics SiGe technologies [146]-[151]. These works have given the possibility to design further HPT in order to be compatible with an HPT which could be integrated to an antenna using wire bonding. In this work, a special care is given to the use of bonding pads and a proper orientation of the HPT on the chip to reduce the length of wires.

For the design of an HPT, the HBTs contained in the Process Design Kit (PDK) components library are taken as a basis for the layout. The component layout is visualized and modified with the aid of Keysight's Advanced Design System (ADS). To design the phototransistors, some process layers normally hidden for internal use by IHP-Microelectronics have been made available. The design and stack of layer of the two HPTs (high voltage HV and high speed HS) mainly differs in the collector region, while the upper layers are common to the two devices.

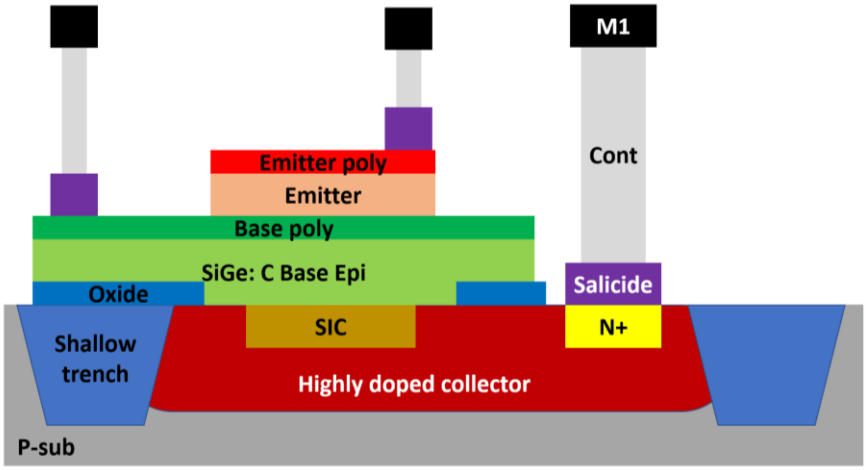

(a)

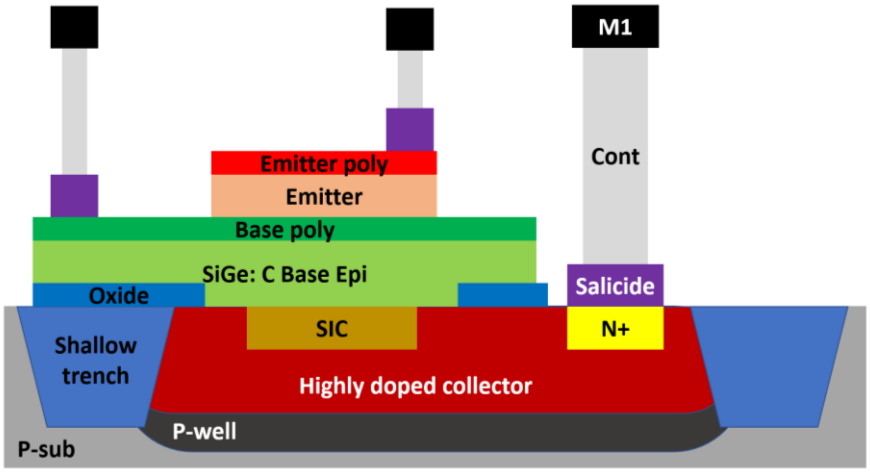

(b)

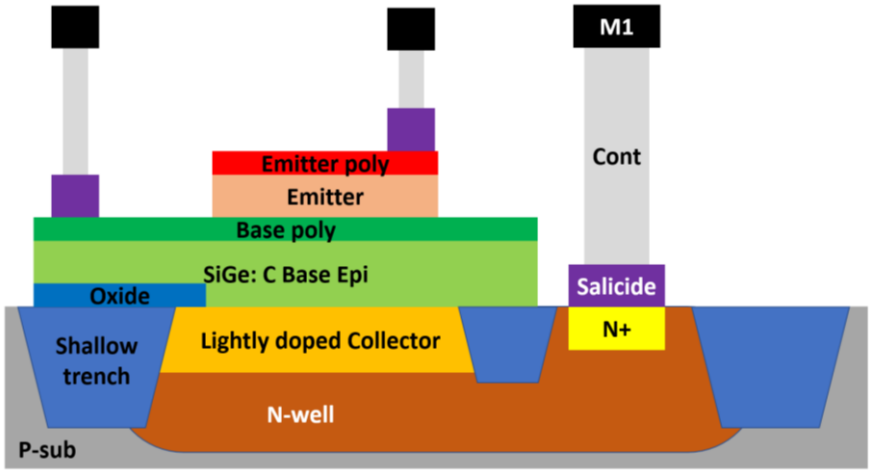

(c)

Fig. 5.1: Cross sections of (a) HS-HBT, (b) HS-HBT with P-well, (c) HV-HBT devices realized in SG13S IHP-technology.

The main steps taken for the design are the following:

- Definition of the active area where the transistor will be fabricated.
- A P-well can alternatively be defined or not underneath the entire structure. This layer is normally blocked in purely electrical transistors but can be added to have a better control of the pn junction formed between the n-collector and the p-substrate.
- For both device topologies a layer is employed to define the npn collector region. Specific layers are then employed according to the device:
  - HS-HPT: a heavily doped collector region is defined.
  - HV-HPT: a lightly doped collector region and a deep n-well have to be defined.
- For both devices an N++ implant is added in correspondence to the collector contact to improve its conductivity.
- A mask is employed to define the emitter window.
- To improve the contacting of the transistors, masks defining the base and emitter polysilicon layers are designed.
- A salicide layer can be added in correspondence of the contacts, aiming at reducing the resistivity of the path. However, it will be removed from the top of the optical window since it has shown to deteriorate the responsivity of the device [152].
- Contacts and Metal layer for electrical connection are defined around the optical window.
- An isolation active ring is defined around the entire structure and it is connected to the ground of the phototransistor.

Fig. 5.1 represents the cross sections of the HS-HBT with and without the additional P-well and of the HV-HBT of the SG13S IHP technology. As mentioned before, the HBTs are the starting components for the design of the HPTs.

To choose the proper HPT to be used in the system, we designed a chip containing the highest number of different HPT within a 0.923 mm^2 surface. In this way, we were able to characterise and measure the performances of each kind of HPT and make the best choice afterwards. The other design rules for this layout required the Collector pads to be on the external side of the chip, to guarantee shorter wire bonding links, necessary for integrating the HPT in the final realization of the photodetector. The other important rules are the minimum pad dimension, fixed to 60 μm, and the vertical distance between the pads, fixed to 100 μm. This last constraint is needed in order to be able to measure the HPT on chip with 100 μm GSG probes, i.e. they have a spacing of 100 μm between each probe. The final conceived design, depicted in Fig. 5.2, is a square chip of side 0.96 mm which contains 8 testing devices as well as 4 calibration structures, all measurable using GSG probes with 100 μm spacing. This layout was manufactured by the company IHP microelectronics and the chips were delivered and ready for testing.

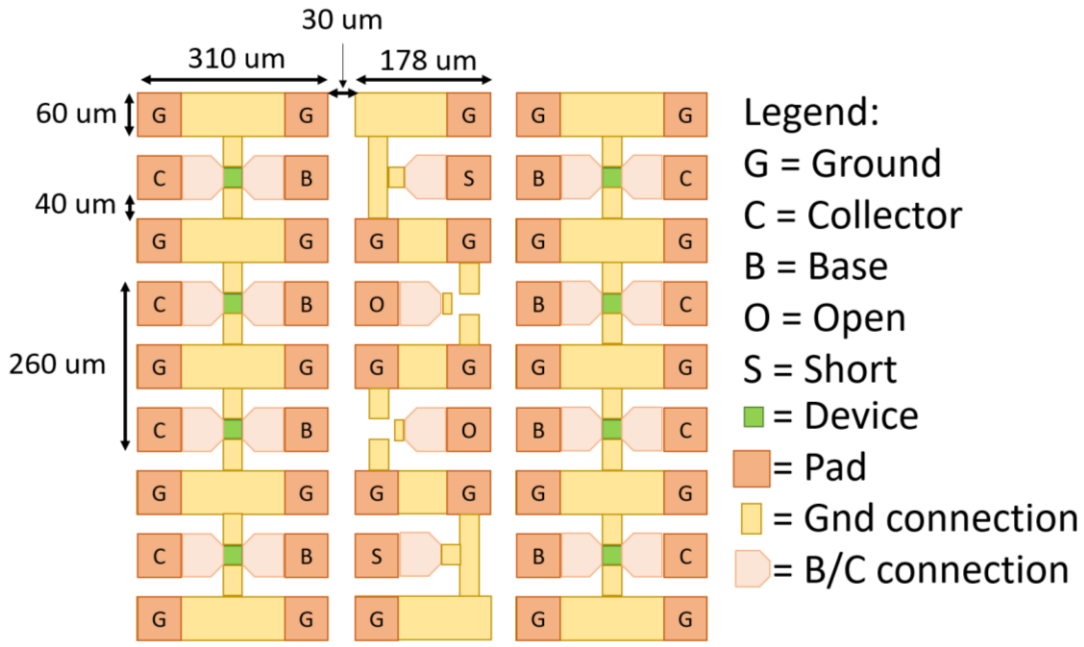

Fig. 5.2: Scheme of the layout of the HPT chip.

The Collector pads are all on the external side of the chip, while conventionally the Base is always on the left while the Collector on the right. This is because when the HPT will need to be wire-bonded to a PCB, it will be necessary to have the length of the wire-bonding on the Collector as short as possible to avoid undesired effects, while the Base wire-bonding is allowed to be longer. The selected typologies of HPTs are the following:

- 10V: it has an optical window of 10 µm x 10 µm and it can sustain high voltages (HV-HPT).
- 20V: it has an optical window of 20 µm x 20 µm and it can sustain high voltages (HV-HPT).
- 30V: it has an optical window of 30 µm x 30 µm and it can sustain high voltages (HV-HPT).
- 30L: it has an optical window of 30 µm x 30 µm and has enhanced performances (HS-HPT).

These 4 categories are replicated in two different versions, called Double Contact Based (2B) and Single Contact Based (1B). The 2B version is in fact the standard layout of the HPT, where the metal contacts of Base, Emitter and Collector are connected to the respective layers of the HPT in two opposite points, at the edges of the HPT structure. While the 1B version has a single connection on one of the edges, causing the current flow in the device to be unbalanced. The main idea is that if the current is unbalanced, the device could benefit in terms of speed due a faster flow, but it would also make it weaker to higher voltages and currents due to the higher flow on a single contact.

5.3. HPT Frequency Domain Characterization

The characterization of HPTs is done with the set-up shown in Fig. 5.3. A Vector Network Analyzer (VNA) collects data on the S parameters from an HPT in CE configuration. The HPT is mounted on a chip and its base and collector terminals are accessible through pads, which are biased by two identical Ground-Signal-Ground (GSG) probes with a 150 µm spacing. Both base and collector DC biases are provided by external generators and the HPT's optical window is illuminated by light coming out from a multimode fiber coupled to a Vertical Cavity Surface Emitting Laser (VCSEL) DC-biased by a third generator. The fiber's end illuminates the HPT from a distance of 50 µm. Two Bias-Tees ensure isolation between the instruments, while the VNA inputs an RF bias to the VCSEL and collects the collector's RF output.

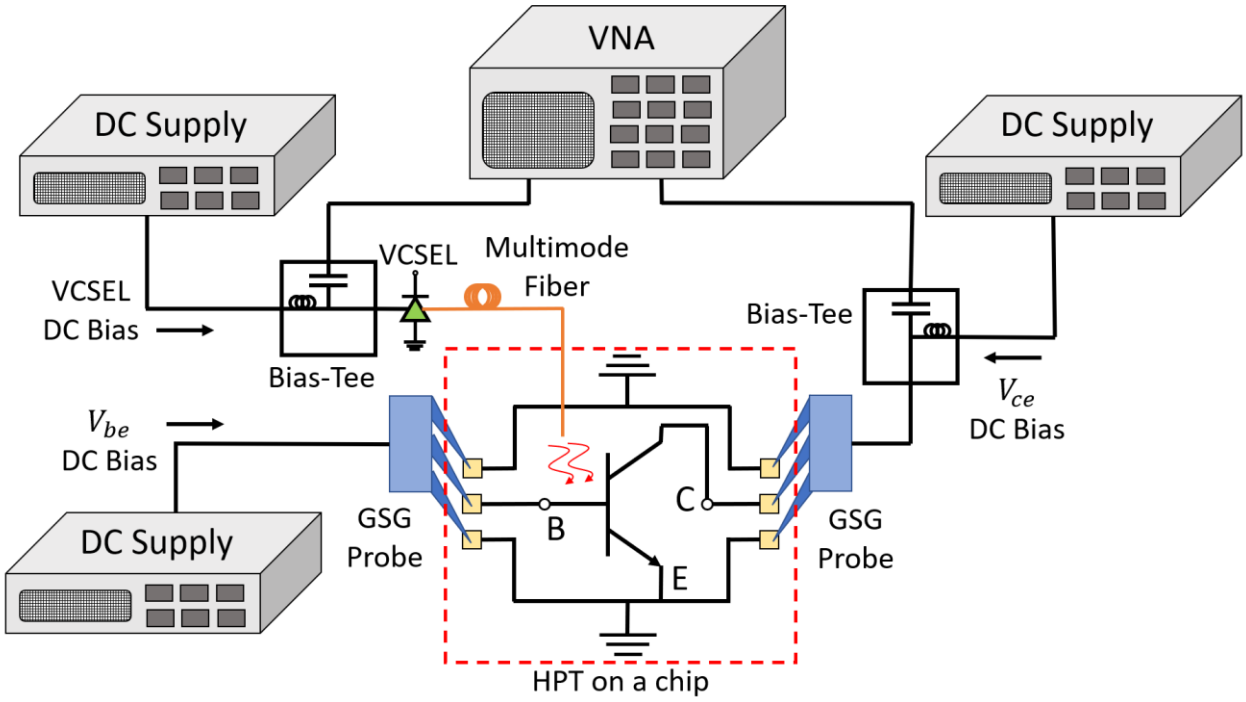

Fig. 5.3: Set-up for the frequency response characterization of the HPTs.

The presented set-up aims at measuring the S parameters of the HPT in different biasing conditions. The most interesting quantity to measure is the S_{21} parameter, as it represents the gain of the HPT. The raw data obtained from the set-up are not sufficient to trace the HPT behaviour, as the VNA calibration cannot include the parts between the probes. To extract the S parameters data related to the HPT it is necessary to perform a de-embedding operation to remove the effects of the probes and of the circuits before and after the HPT. To do this, it is necessary to have access to on-chip SOLT calibration structures, which are used to collect data to move the reference planes of the VNA on the input and output ports of the HPT. This concept is better illustrated in Fig. 5.4. Regarding the calibration of the laser, its biasing point was chosen in its linear region to ensure a linear frequency response. Then, its gain was measured and subtracted in the de-embedding of the HPTs' measurements.

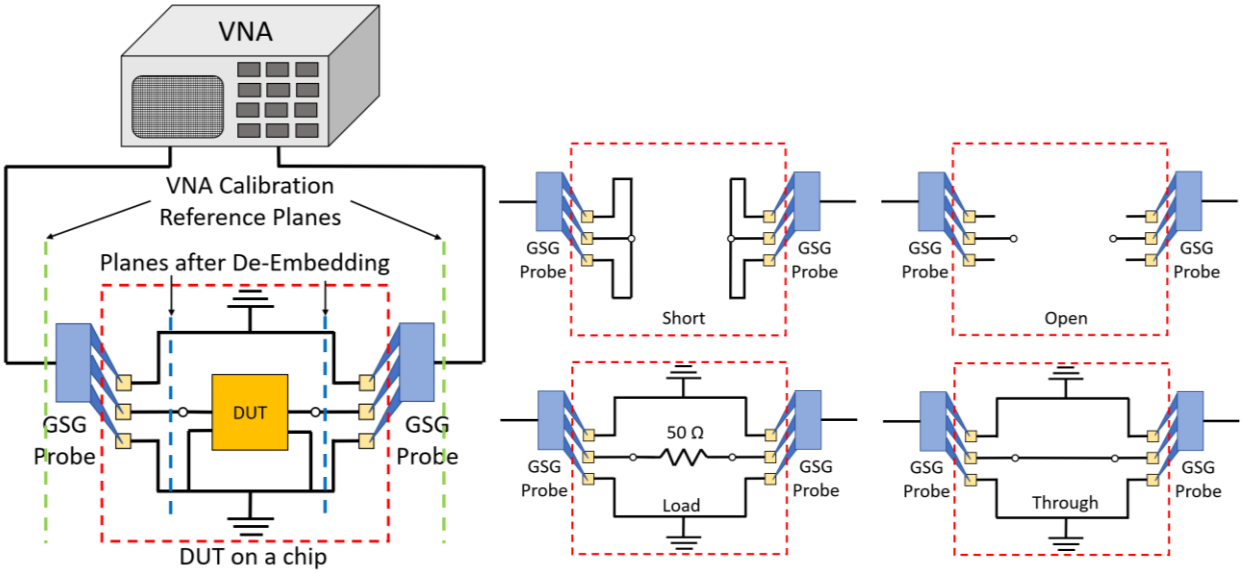

Fig. 5.4: On the left, reference planes with the VNA calibration only (green) and after the de-embedding (blue); on the right, SOLT on-chip structures for the de-embedding.

The measurements were carried out considering different levels of V_{be} and V_{ce}. In particular V_{be} ranging from 0 V to 1 V and V_{ce} ranging from 0 V to 5 V. For reference, only the measurements related to the 10 μm^2 HV-HPT will be shown, as important issues arose from the results obtained.

Let us start from a DC characterization of the HPT, in particular the Gummel plot of the devices. The Gummel plot shows on the same plot the behaviour of the collector and base currents I_C and I_B in function of the base-emitter voltage V_{be}, while the base-collector voltage V_{bc} is kept constant. Fig. 5.5 shows the Gummel plot of the 10 μm^2 HV-HPT. The trend of the curves correctly resembles the one observed in HBTs, with I_C and I_B increasing after a threshold value of 0.4 V for I_C and 0.6 V for I_B and with I_C reaching larger values than I_B due to the amplification of the transistor effect. β is the amplification coefficient, defined by the relation $I_C = \beta I_B$. The β peak value of 243 is reached around $V_{be} = 0.82$ V, which is the optimal bias of the HPT, as it is related to the maximum amplification effect in the HPT. Similar results are obtained also for the other HPTs, meaning that the DC behaviour of the devices is good.

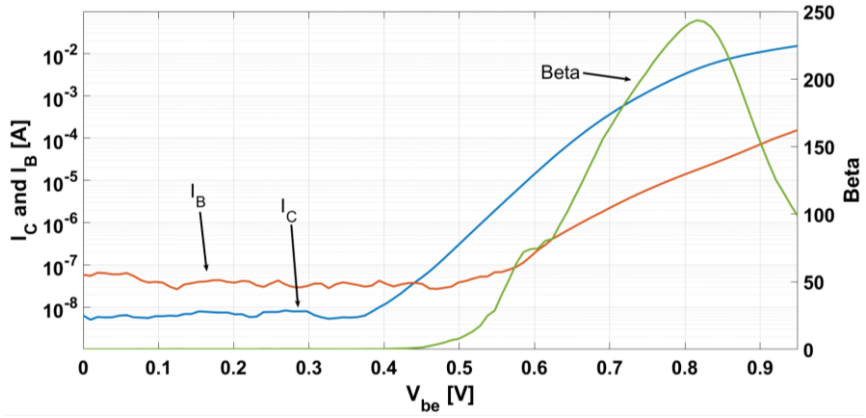

Fig. 5.5: Gummel plot of the 10 μm2 HV-HPT.

Another important measurement is the ensemble of the $I_C - V_{ce}$ curves which show the behaviour of the of I_C on different V_{ce} biasing. A set of curves is obtained, one for each different V_{be} biasing. The same measurement can be performed with the laser either illuminating or not the HPT. The main difference between the two cases is that the set of curves related to the turned-on laser is raised by a quantity of 0.8 mA, corresponding to the generated photocurrent, as shown in Fig. 5.6.

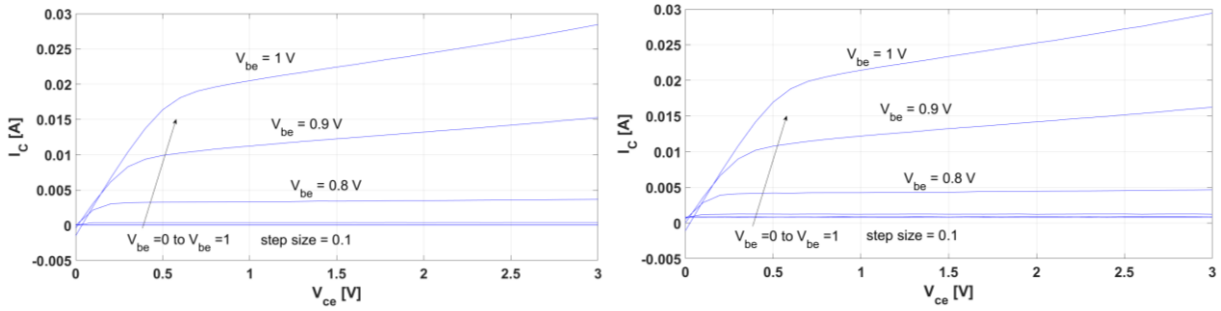

(a) (b)

Fig. 5.6: $I_C - V_{ce}$ plots of the 10 µm2 HV-HPT. (a) is related to the turned-off laser case, while (b) to the turned-on laser case.

The results obtained are compliant with the expectations, thus confirming that the HPTs behave correctly at DC frequency.

The next step is the Opto-RF characterization, which consists in extracting the S_{21} parameter of the HPT in function of the frequency. This kind of measurement is performed for different V_{ce} biasing and for different biasing of either I_B or V_{be}. Several sets of measurements have been performed and the results obtained were unfortunately too unclear to draw definite conclusions. In general, an HPT in PD mode presents lower gain with respect to 3T mode and the peak performance is usually reached when V_{be} is such that the gain β is maximized. It is normal to observe a transition frequency at which the gain of HPT in PD mode equals the gain in 3T mode and normally this frequency is lower when the optical window size of the HPT is bigger. This transition frequency is also used as a reference for the maximum working frequency of the HPT. Fig. 5.7 shows a comparison between the Opto-RF behaviour of the 20 µm^2 2B HV-HPT and the 20 µm^2 1B HV-HPT. It can be observed that while the 1B HPT reaches values of gain about 2 dB higher at lower frequencies, the transition frequency is lowered as well, passing from 340 MHz (2B HV-HPT) to 150 MHz (1B HV-HPT).

These results already show lower performances in the behaviour of the HPT compared to results obtained in previous works for HPTs done with the same technology, such as in [152]. It is normal to have a transition frequency where the HPT in PD mode has better performance with respect to the 3T mode, however it is desirable to have this transition happen at higher frequencies than the ones shown in Fig. 5.7. In addition, the obtained curves are too similar for different biases. Normally, the difference between the curves for each V_{be} bias can go up to more than 10 dB, while in this case the difference between the curves is below 5 dB. This means that at the working frequency of 2.45 GHz, when modulating V_{be} with a square wave, the difference between the output in 3T mode and in PD mode is less than 5.33 dB, thus making the HPT not suitable as a switch for a TMA.

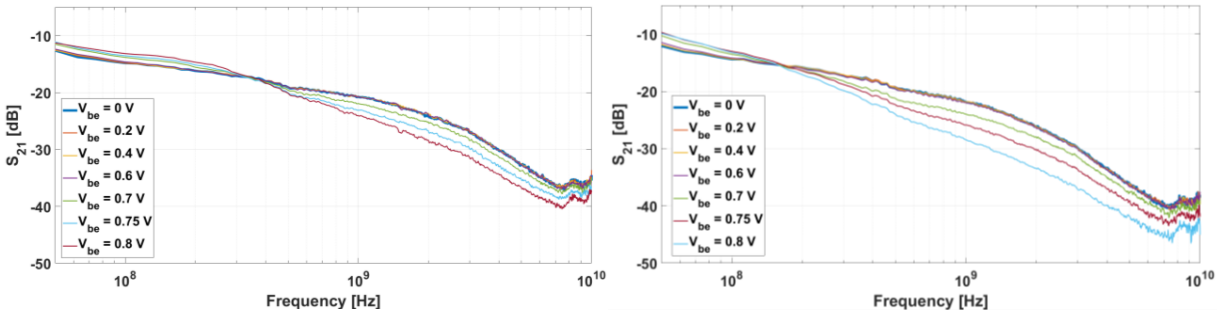

(a) (b)

Fig. 5.7: Opto-RF plots for different V_{be} biasing at $V_{ce} = 2$ V. (a) is the 20 µm2 2B HV-HPT, while (b) is the 20 µm2 1B HV-HPT.

Fig. 5.8 shows a comparison of the measurements related to the 2B HPTs, in particular the 20 µm^2 2B HV-HPT, the 30 µm^2 2B HV-HPT and the 30 µm^2 2B HS-HPT. In all the shown cases, the behaviour of the curves is still low performing, with transition frequencies too low for the foreseen applications. In particular, we measured 340 MHz for the 20 µm^2 2B HV-HPT, 200 MHz for the 30 µm^2 2B HV-HPT and 60 MHz for the 30 µm^2 2B HS-HPT.

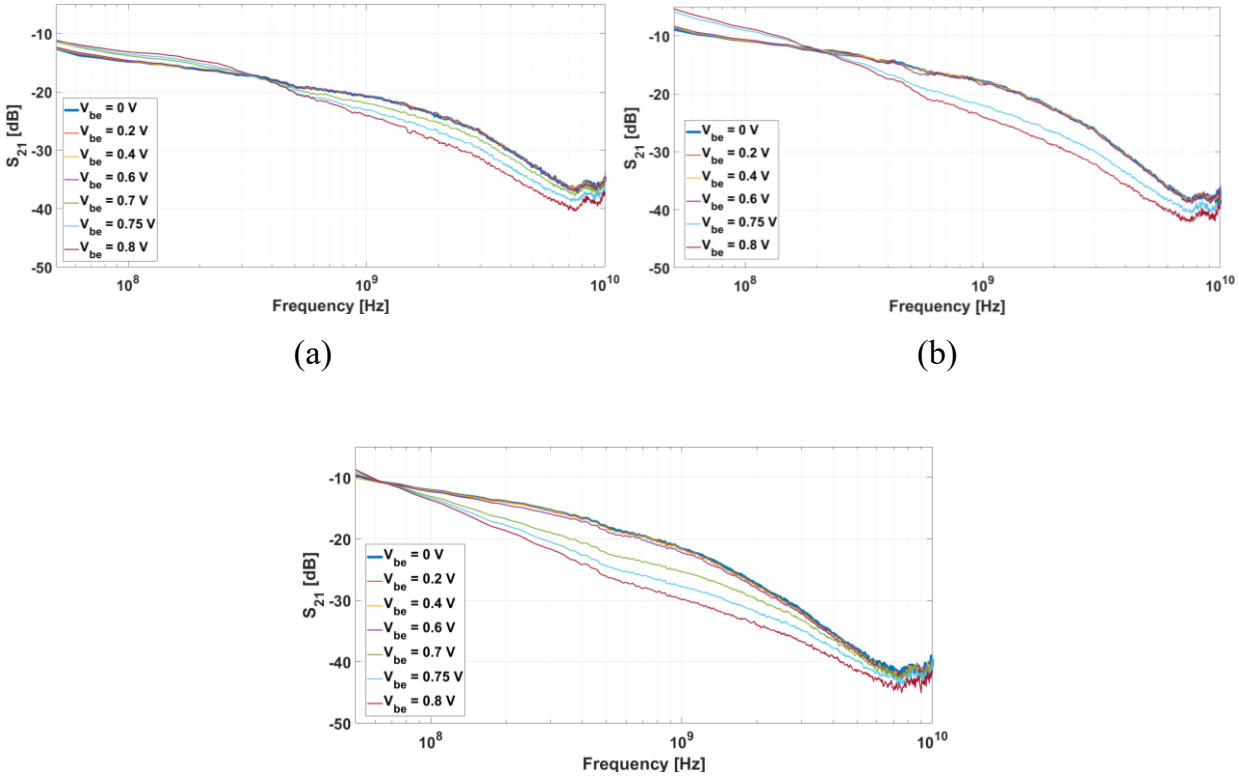

(a) (b)

(c)

Fig. 5.8: Opto-RF plots for different V_{be} biasing at $V_{ce} = 2$ V ((a) and (b)) and $V_{ce} = 1.6$ V ((c)). (a) 20 µm2 2B HV-HPT, (b) 30 µm2 2B HV-HPT and (c) 30 µm2 2B HS-HPT.

Following these results, we opted to perform complementary measurements and to focus particularly on the 10 µm^2 2B HV-HPT, as the 1B HPTs and the larger HPT showed a transition frequency lower than 1 GHz. Fig. 5.9 shows the Opto-RF measurements obtained from the 10 µm^2 2B-HV HPT, related to both V_{be} and I_B. On the V_{be} side, the results obtained

are promising as there is a clear distinction between the PD mode and the 3T mode and the On-Off Ratio (OOR) is greater than 5.33 dB up to almost 4 GHz, which is an overall good performance. However, on I_B side, all the curves are almost overlapping independently of the value of I_B. This behaviour is not desirable, as the curves are expected to have greater difference, like for the Opto-RF plots where V_{be} is changed in Fig. 5.9b.

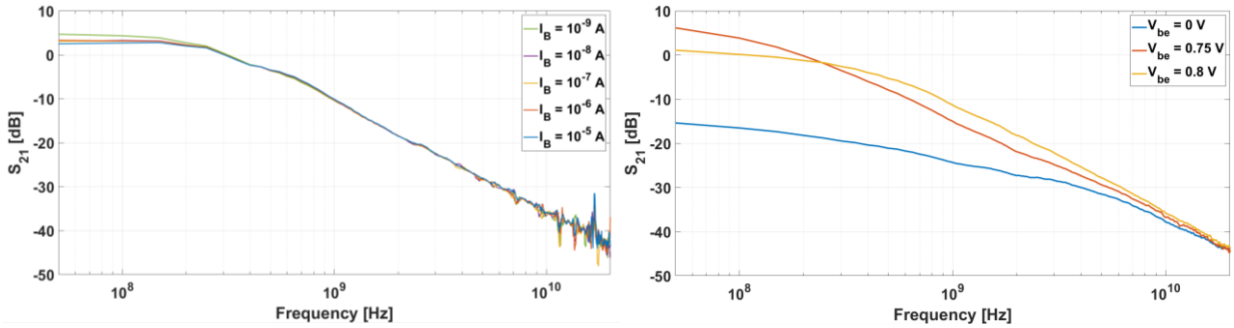

(a) (b)

Fig. 5.9: Opto-RF plots of the 10 µm2 HV-HPT for different (a) I_B and (b) V_{be} biasing at $V_{ce} = 3$ V.

To summarize, repeated cycles of measurements have shown unclear results in the frequency behaviour of the conceived HPT. While some results are promising, it is still unsure whether these HPTs are safe to use or not. Unfortunately, it is still not clear what is the cause of the detected anomalies, but we elaborated two main hypotheses:

- The presented set-up is very sensitive to calibration errors and extreme care must be taken in performing measurement. One or more errors in the calibration or the de-embedding processes could have detrimental effects on the success of the measurements.
- Errors in the design of the HPT on ADS could have led to the fabrication of devices with poor performances or even malfunctioning, thus compromising the chips.

Due to time constraints on the project, we opted for the following solution: to substitute the fabricated HPTs with older devices which have been measured and demonstrated to be working well in previous research works. We opted for the HPTs employed in the ORIGIN project [64], in particular the HPT named 10SQxEBC, realized with the technology TELEFUNKEN GmbH [153]. The nomenclature of the HPT means it has a 10x10 µm^2 optical window area, it is integrated in common emitter topology and its base and collector contacts are accessible through dedicated pads. The frequency performance of such devices is shown in Fig. 5.10. Focusing on the 10SQxRBC HPT, it can be noted that for all analysed frequencies, the OM gain in 3T mode (i.e. also called HPT mode) is always higher than the OM gain in PD mode. The OOR, which is the difference between the OM gain in HPT mode and PD mode curves in dB is steadily higher than 5.33 dB until up to 5 GHz, hence why we chose this HPT as a substitute. The shown curves allow also to appreciate the effect of increasing the dimensions of the optical window. In fact, the second set of curves is related to the HPT 50SQxEBC, having a 50x50 µm^2 optical window area. It is clear that, while the larger area allows to reach higher OM gain values at lower frequencies due to the higher amount of received photons, the device is slower. The PD mode and HPT mode intersect at 1 GHz, meaning that the HPT behaves in the same way regardless of the V_{be}. This is also the

limit frequency of employment of such HPT. The data shown in the plots is related to the peak performance bias of the bias, namely $V_{ce} = 2$ V and $V_{be} = 0.857$ V for the HPT mode and $V_{ce} = 2$ V and $V_{be} = 0$ V for the PD mode.

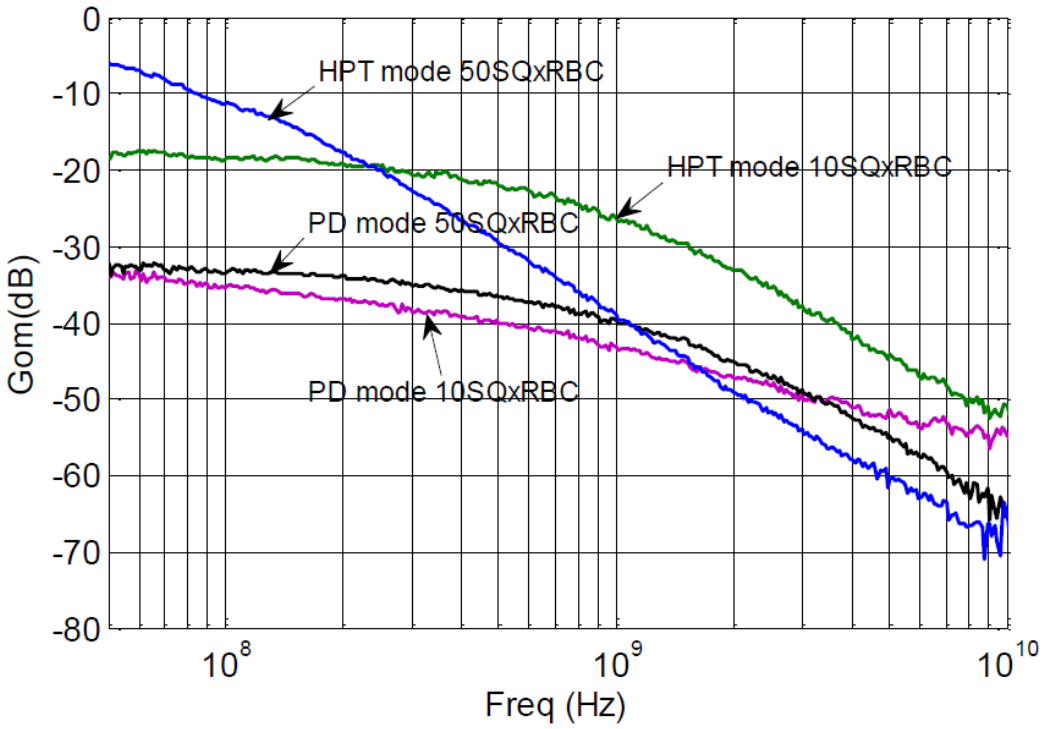

Fig. 5.10: OM gain of the ORIGIN HPTs 10SQxEBC and 50SQxEBC. HPT mode bias: $V_{ce} = 2$ V and $V_{be} = 0.857$ V; PD mode bias: $V_{ce} = 2$ V and $V_{be} = 0$ V.

5.4. HPT Time Domain Characterization

It is important for HPTs to be fast enough to detect the antenna carrier, in our case 2.45 GHz, and provide the modulation for the TMA, which happens at much lower frequencies. To prove the HPT's capabilities in modulating the output signal we prepared the set-up shown in Fig. 5.11. The aim is to feed the HPT's V_{be} with a square wave signal of increasing frequency and check the output V_{ce} with an oscilloscope. The square wave is generated with an Arbitrary Waveform Generator (AWG) which can generate waves with adjustable duty cycle and amplitude up to a frequency of 100 MHz. Since the generated waves always have zero average value, it is necessary to raise the wave of half its amplitude with an external DC supply. The HPT on chip is illuminated by an unmodulated VCSEL and the output at the collector is divided into AC and DC, with the DC port providing the V_{ce} bias and the AC port monitoring the output through an oscilloscope. The V_{be} ranges from 0 V to 0.7 V, while the V_{ce} from 0 V to 3 V. The duty cycle applied to the HPT is 50% and the HPT tested is the one designed and fabricated in SG13S technology.

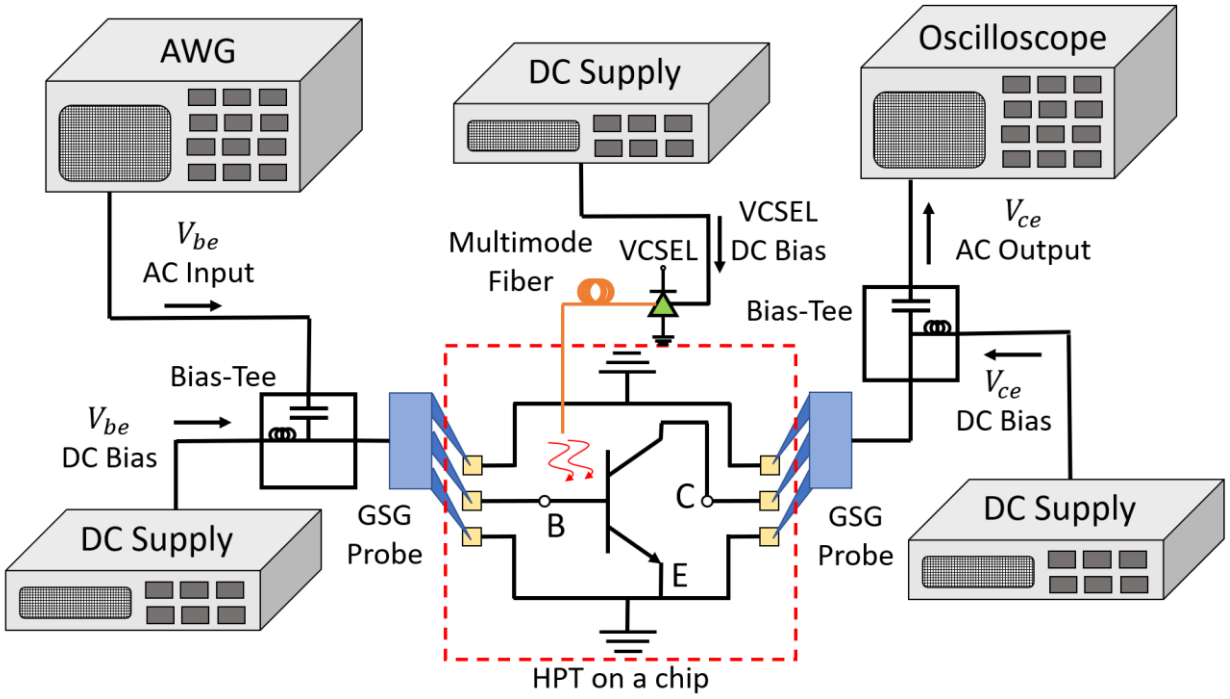

Fig. 5.11: Set-up for time domain measurements of HPTs.

The results are shown in Fig. 5.12, representing the AC output response of the 10 μm^2 HV-2B HPT biased with V_{ce} = 3 V and a 50% square wave at V_{be} varying between 0 V and 0.7 V. The considered frequencies are 1 MHz, 10 MHz and 100 MHz as lower frequencies are below the working frequencies of the bias-tees, while higher frequencies cannot be reached by the AWG. The plot at 1 MHz shows that the HPT responds well at 0.7 V, with a discharge behaviour in the lower fronts of the wave, which might be due to the bias-tees capacitors or to capacitive effects internal to the HPT. In the 10 MHz plots we note that the HPT still responds well and keeps up with the input wave, however some spurious effects start to appear in the lower part of the wave. These effects become worse at 100 MHz and the output signal is much attenuated compared to the 1 MHz case, suggesting that the device might not work properly at those frequencies and that the performances at higher frequencies are worse overall.

Based on the frequency domain results shown before in section 5.3, the On-Off Ratio below 1 GHz is greater than 10 dB, as in Fig. 5.9b. However, when the DC voltage V_{ce}= 3 V, the output signals in Fig. 5.12 vary between 3 V and 4.5 V at 1 MHz, between 3 V and 4 V at 10 MHz and between 3 V and 3.5 V at 100 MHz. Therefore, the On-Off Ratio related to the measured output voltage is lower than expected. We speculate that the observed behaviours might be due to capacitive effects internal to the HPTs, but all hypotheses need to be assessed in the future with measurements and at present we cannot provide definitive answers.

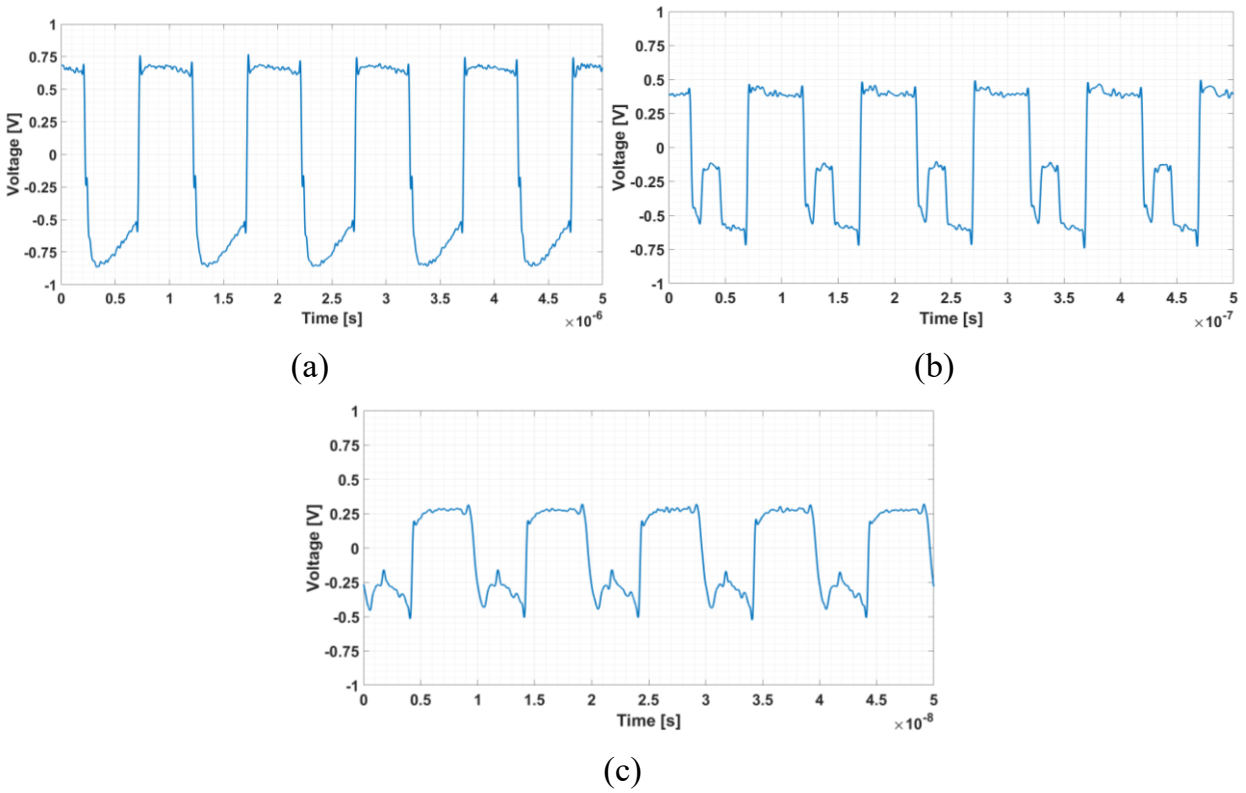

Fig. 5.12: AC V_{ce} output of the 10 µm2 HV-2B HPT at frequencies (a) 1 MHz, (b) 10 MHz, (c) 100 MHz (see time axis order of magnitude).

In conclusion, the presented measurements prove the HPTs designed and measured in chapter 5 do not perform well enough for the envisaged application. The final choice are the HPTs employed in the ORIGIN project, in particular the 10SQxEBC HPT. This SiGe HPT is characterized by a square optical window of 10x10 µm^2 integrated in CE topology with all the terminals (Base, Collector and Emitter) accessible through dedicated pads. The arisen issues need to be carefully addressed to understand the root of the problems encountered. However, in the final packaging of the HPTs we still want to include at least one of the designed HPTs to test it at modulating frequencies no higher than 1 MHz. In fact, even if the measurements showed that it is a safer choice to change HPTs, the time domain behaviour of the designed HPT at 1 MHz is promising enough and should be considered in the final tests.

5.5. Packaging of the HPT on a PCB board

This section describes the how the HPT are packaged in order to be used in the final prototype of the proposed RoF-TMA system, then follows with a description of the measurements to be performed on such system. Unfortunately, the actual measurements were not realized in time and therefore they are not included in the chapter due to the time constraints of the thesis. Instead, the perspectives on the final system characterization and measurements are presented.

The HPT, in order to be used as a photodetector in the RoF-TMA system, needs to be packaged keeping in mind the following needs: compactness, modularity, input ports to provide the modulating sequences on the base, the collector bias and the RF signal through an optical fiber and finally the antenna output port. The design needs modularity in order to

have more flexibility during the final tests and also for future use. In this way it is possible to have full control over factors such as the number of elements of the array and the antenna spacing. We designed a printed circuit board (PCB), shown in Fig. 5.13, with an input SMA port for the modulating sequence and an output SMA port for the antenna. The SMA ports are installed by welding their ground and signal connectors to the "GND" rectangular slots and to the line respectively. The PCB has a coplanar line design adapted to 2.45 GHz, which is the resonating frequency of the antennas, the HPT has an allocated space highlighted in Fig. 5.13, so that it is placed near the antenna line, the modulating sequence line and the ground. In this way the wire bonding operations necessary to link the HPT's base, emitter and collector nodes to the modulating sequence line, ground and antenna line respectively are eased. The antenna line is provided with an integrated bias-tee, consisting of a 40 nH inductance coil and a 15 pF capacitor, to isolate the DC and RF components of the collector's bias. In particular, the RF component of the collector's current needs to be directed towards the antenna, while the DC path is used to provide the V_{ce} DC bias through a pair of pins labelled "GND" and "Vcc". An additional capacitor of 150 nF is added to the DC path in order to direct any spurious RF component to ground and to better isolate the external V_{ce} generator. Finally, the "GND" pin on the bottom is used to connect the ground planes of two neighbouring PCBs.

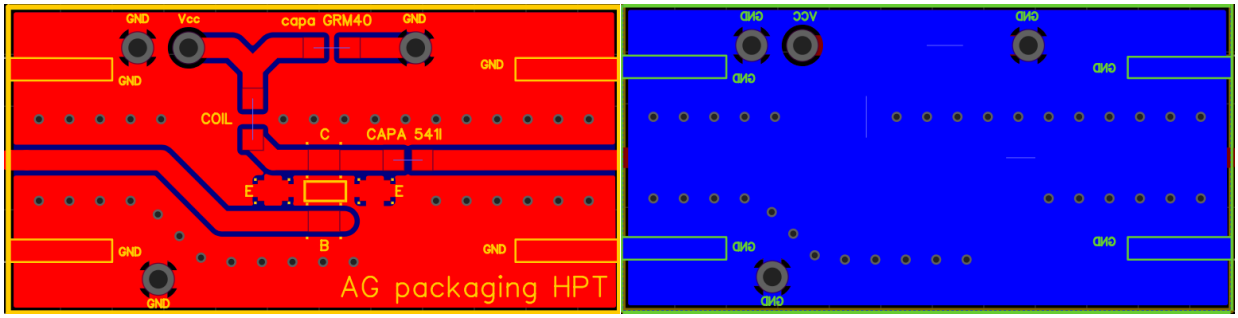

Fig. 5.13: Top view (red) and bottom view (blue) of the PCB for the HPT packaging. The dedicated space for the integration of the HPT is highlighted by a yellow rectangle and the letters E, B and C highlight the zones for the wire bonding of the HPT nodes.

The design of a bias-tee requires particular attention as the components to be used need to be carefully selected depending on the frequency requirements. For a bias-tee working in a range $[f_{min}, f_{max}]$ with known impedance loads at its DC and RF ports Z_{DC} and Z_{RF},the main design rules of thumb are the following:

- At f_{min}, the bias-tee RF port capacitor must present a reactance X_C equal to $Z_{RF}/5$.
- At f_{min}, the bias-tee DC port inductance must present a reactance X_L equal to $Z_{RF} \cdot 5$.
- The components of the bias-tee must have a resonance frequency higher than f_{max}.

In this way, we ensure that signals with frequency above f_{min} pass through the RF port and are blocked by the DC port. In our case, Z_{DC} is the impedance of the V_{ce} generator, while Z_{RF} is the antenna's impedance and both are equal to 50 Ω, so that $X_C = 10\ \Omega$ and $X_L = 250\ \Omega$. Considering a frequency interval between $f_{min} = 1$ GHz and $f_{max} = 10$ GHz it is:

$$C = \frac{1}{2\pi f_{min} X_C} = 15 \text{ pF}$$
$$L = \frac{X_L}{2\pi f_{min}} = 40 \text{ nH} \tag{5.1}$$

These are the minimum values of capacity and inductance needed for the bias-tee to operate above 1 GHz. This is furtherly proved by simulating the bias-tee circuit shown in Fig. 5.14, representing our situation.

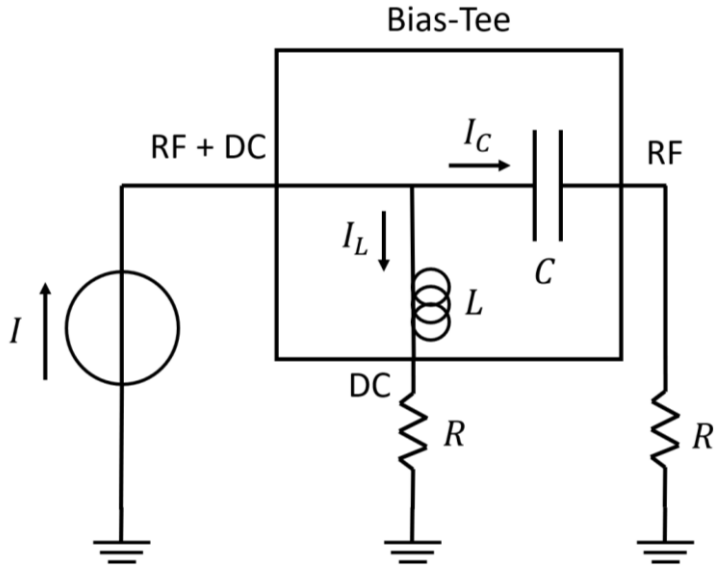

Fig. 5.14: Bias-tee circuit simulation. A generator simulating the HPT collector feeds the RF+DC port of the bias-tee and the DC and RF ports are connected to equal loads R.

The currents on the loads on the DC and RF ports, respectively I_L and I_C, are given by:

$$I_L = \frac{1}{1 + \frac{R - \frac{j}{\omega C}}{R + j\omega L}} I$$
$$I_C = \frac{1}{1 + \frac{R + j\omega L}{R - \frac{j}{\omega C}}} I \tag{5.2}$$

If we compute the power on the DC port load and on the RF port load and normalize them to RI^2 (i.e. the maximum available power on any of the loads) we obtain the curves in Fig. 5.15.

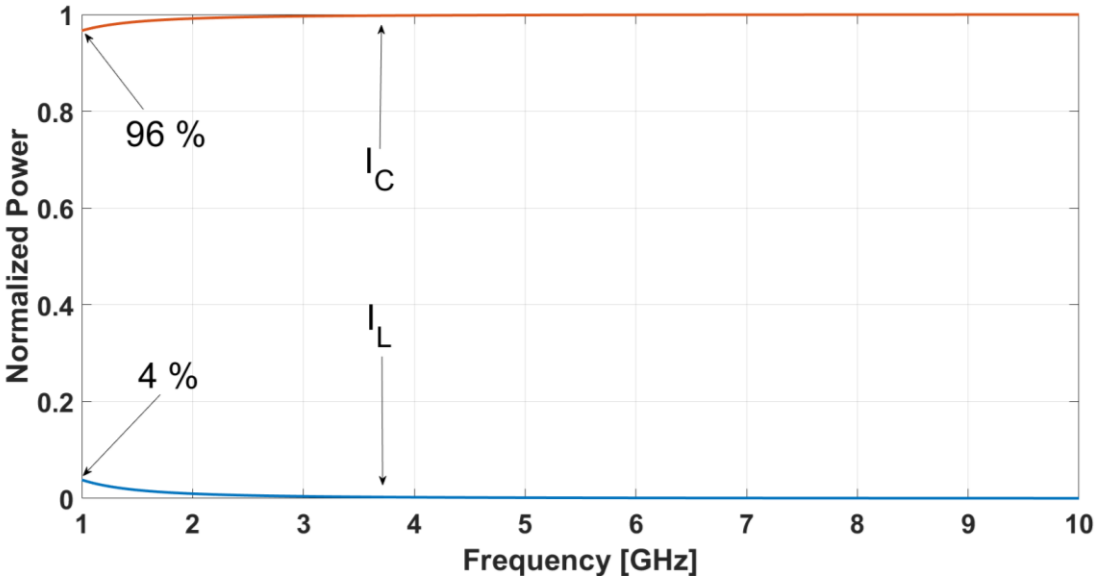

Fig. 5.15: Bias-tee circuit simulation results. The two curves represent the power absorbed by the DC port load (blue) and RF port load (red). At 1 GHz, 96% of the power is on the RF load and only 4% on the DC load.

The resulting curves show that at 1 GHz approximately 96% of the available power is located on the RF port load, while the remaining 4% is on DC port load, thus confirming the effectiveness of the bias-tee and of the aforementioned design rules. Furthermore, the additional capacity on the DC port ensures that the residual RF current on the DC port of bias-tee is redirected to the ground. Fig. 5.16 shows the delivered PCB, where the zones for gluing the components are visible.

To integrate the HPT, we need to: glue the HPT to its dedicated zone, solder the components and the SMA ports to their respective zones, wire bond the HPT's base, collector and emitter to the corresponding pads on the PCB and finally glue a multimode fiber pigtail aligned on the optical window of the HPT. The wire bonding is the operation of connecting through thin wires, usually in gold, copper or aluminium, integrated circuits' pads and PCB circuitry. The two main wire bonding techniques are the ball bonding and the wedge bonding and both of them require some degree of expertise to be performed. It is for this reason that the wire bonding is performed by the LABSTICC team in Brest. The fiber pigtail gluing will be performed by the ESYCOM team. The operation consists in aligning a cleaved multimode fiber pigtail vertically on the HPT optical window and then to use a special glue to fix it in position. Unfortunately, due to time constraints, it is not possible to include a picture of the packaged HPT, which will be finished before the defence of this project. Nevertheless, a representation of the final package is given in Fig. 5.17.

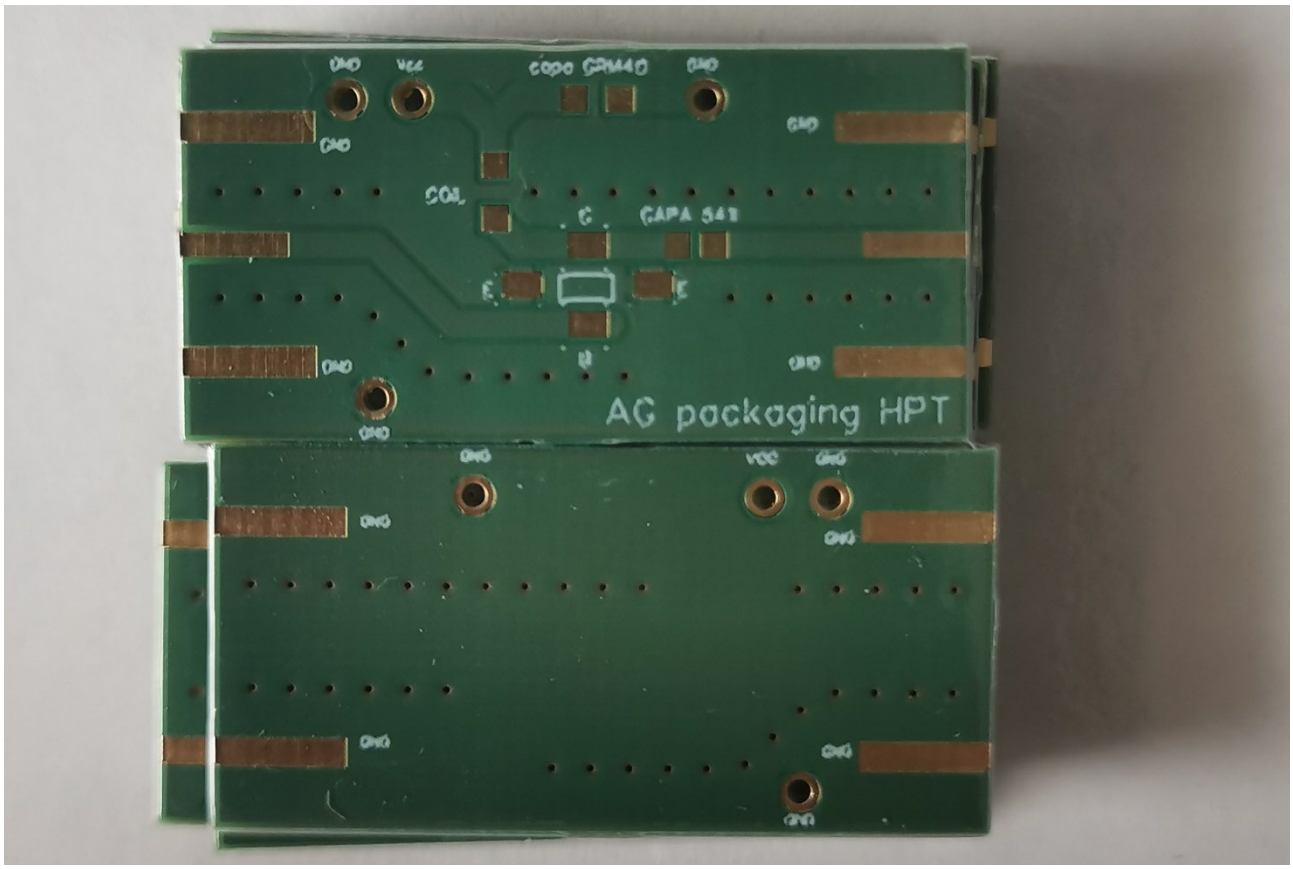

Fig. 5.16: Photograph of the designed PCB for HPT packaging.

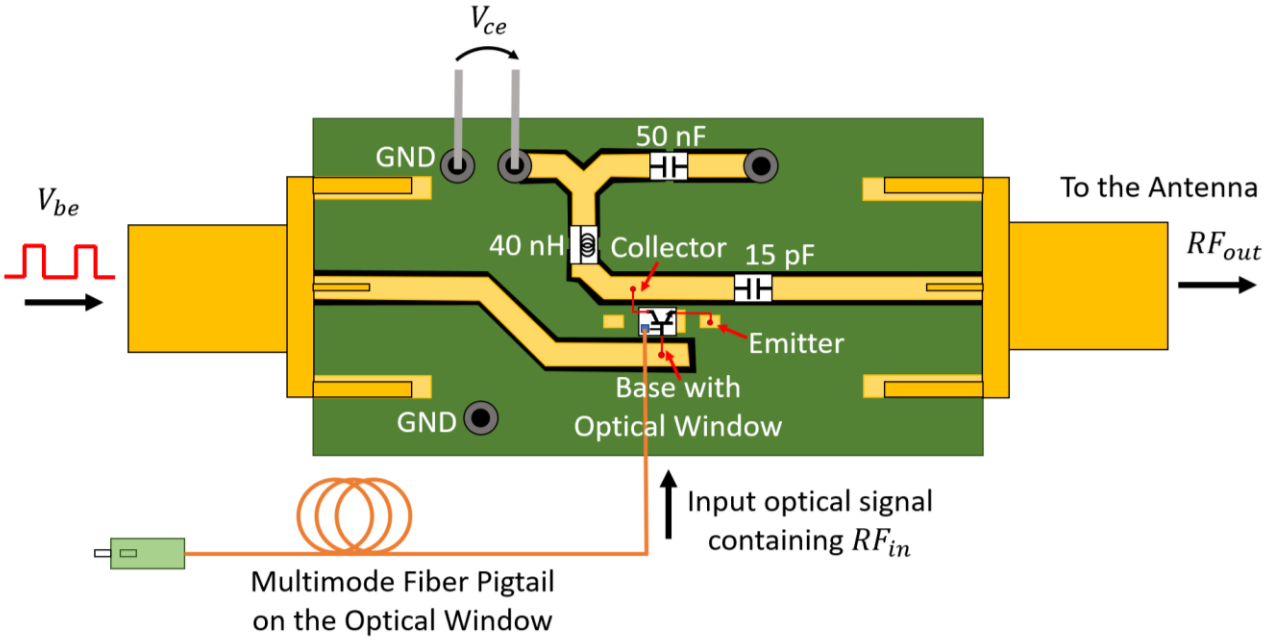

Fig. 5.17: Representation of the fully packaged HPT.

5.6. Perspectives on the RoF-TMA final prototype realization and characterization.

After the packaging of the HPT, all the elements composing the RoF-TMA system are ready to be combined, as shown in Fig. 5.18. The system differs from the one shown in chapter 2 for the RoF link, composed of a VCSEL coupled to a multimode fiber terminating in the packaged HPT. The modulating sequences are always provided externally by a *STM32VLDiscovery* board to the input PCB port to modulate the V_{be} tension. The measurements set-up will be identical to the one used in chapter 3 and aims at scanning the radiation diagram emitted by the RoF-TMA system at different frequencies. As for the first prototype, the main objective is to measure the performances of the RoF-TMA system with different numbers of elements to prove the TMA behaviour and also make comparisons with the first prototype. The antennas emit at 2.45 GHz and the modulating frequency is fixed at 10 kHz. The aim is to scan and measure the radiation diagram emitted by the RoF-TMA system and compare the results with the radiation diagram of a theoretical TMA fed with the same modulating sequence. I expect to obtain similar behaviour to the system employing photodiodes. This expectation is motivated by the fact that I demonstrated that a TMA behaviour is obtainable even from non-ideal switches, fixed a minimum OOR of 5.33 dB to obtain acceptable performance and chose the HPT best satisfying this constraint. The sole aspect that could impair the system is the inverting nature of HPTs used in Common Emitter (CE) topology. In fact, CE topology bipolar transistors are known to amplify current but also to invert tension at their output. This inversion is related to the voltage only, while the current is unchanged and amplified. The polarity inversion of voltage could cause problems at the antenna transmission level. To solve the issue, it is sufficient to feed the HPT's V_{be} with the sequence shifted of 180°. Unfortunately, due to time constraints for the thesis manuscript, it is not possible to show results here, but they will be shown in the final presentation of this work. Nevertheless, we gave a description of the system intended to be employed along with the expectations of the results that we aim to obtain.

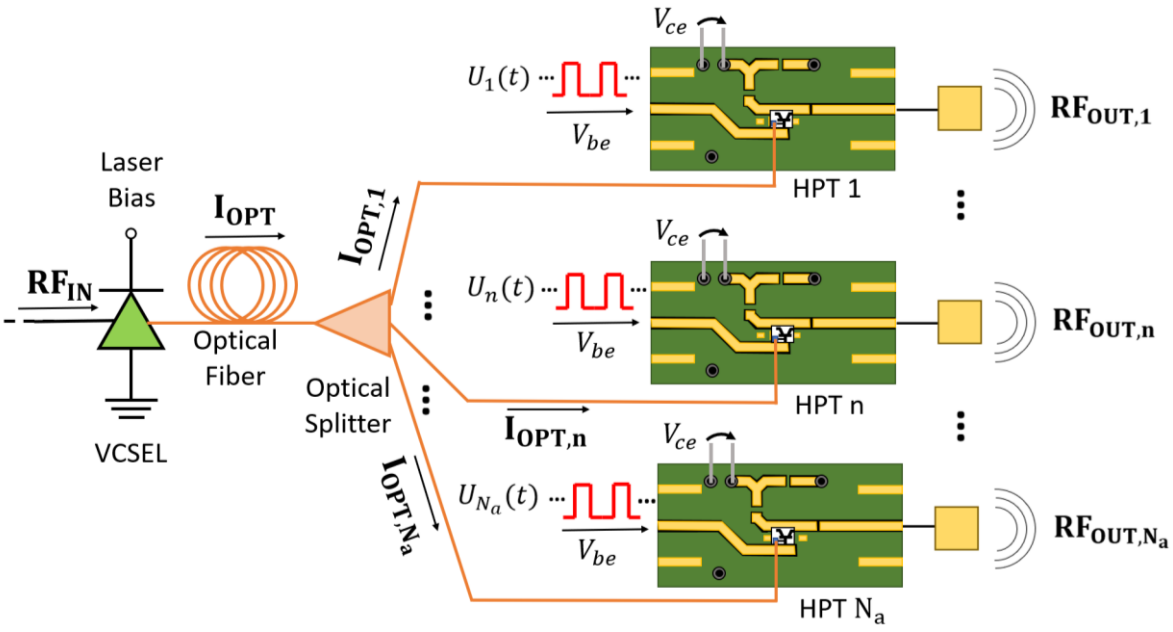

Fig. 5.18: Representation of the final RoF-TMA system prototype.

A second set of measurements will focus on testing the optimization program shown in section 3.5 to determine the modulating sequences of a TMA with up to 4 elements, but also to test the phase shifts effects mitigation showed in section 3.4. The aim is to test the developed optimization program to check precise transmission in multiple directions at different frequencies and to correct the phase shifts caused by the difference in length of fiber paths. Two different situations will be analysed: at first, the modulating sequence is applied without caring for the phase shifts correction, while in the second scenario, corrections for mitigating the phase shifts are applied. It is useful to remind that due to the nature of TMA, it would be useless to consider specular harmonic frequencies (i.e. $f_0 + hf_M$ and $f_0 - hf_M$) when phase shifts are involved. This is because when no phase shifts are present, any modulating sequence applied to the TMA generates specular radiation diagram on such frequencies. In fact, recalling Eq. (3.7) it easy to demonstrate that in absence of phase shifts (i.e. $\varphi_n = 0°$, for every n):

$$AF_h(\theta) = AF^*_{-h}(-\theta) \tag{5.3}$$

where x^* denotes the complex conjugate operator. Eq. (5.3) is true due to $sinc(h\pi c_n)$ being an even function. The associated radiation diagrams are proportional to $|AF_h(\theta)|^2$ and $|AF^*_{-h}(-\theta)|^2$, therefore the radiation at $f_0 + hf_M$ is mirrored at $f_0 - hf_M$. However, in presence of unwanted phase shifts, this relation is no more valid. In this situation, when applying a modulating sequence cancelling the effects of the phase shifts at $f_0 + hf_M$, then it is automatically impossible to recover the correct radiation diagram at $f_0 - hf_M$. For instance, let us consider a series of unwanted phase shifts φ_n different from 0° and choose c_n and $c_{i,n}$ such that $h\pi(c_n + 2c_{i,n}) = \varphi_n$ at $f_0 + hf_M$. The AFs then become:

$$AF_h(\theta) = \sum_{n=1}^{N_a} A_n c_n sinc(h\pi c_n) e^{jknD\ sin(\theta)} \tag{5.4a}$$

$$AF_{-h}(\theta) = \sum_{n=1}^{N_a} A_n c_n sinc(h\pi c_n) e^{j2\varphi_n} e^{jknD\ sin(\theta)} \tag{5.4b}$$

Eq. (5.4a) and (5.4b) show that the chosen modulating sequences completely countered the phase shifts at $f_0 + hf_M$, but at the same time doubled the phase shifts $f_0 - hf_M$. This demonstrates that phase shifts correction cannot be done on specular frequencies, concluding that for the final tests on the phase shifts correction it will be necessary to carefully choose the set of testing frequencies.

5.7. Conclusions

In this chapter I showed the design rules and realization of a customized chip with integrated HPTs for this PhD thesis. Then I described the set-ups and showed the measurements of characterization of the HPTs in both frequency domain and for the first time in time domain.

The obtained results showed that the designed HPTs' performances both in time and frequency are not satisfying for a TMA system. In particular, frequency domain

measurements showed transition frequencies below 1 GHz for all the designed HPTs. While SiGe photodetectors generally show lower transition frequencies compared to other semiconductors, the state of the art shows that frequencies up to 15 GHz and beyond are achievable. Time domain measurements showed a decrease in output voltage gain with frequency and non linear effects already present at 10 MHz. The minimum requirements for TMA applications are a transition frequency and an On-Off Ratio greater than 5.33 dB beyond 2.45 GHz. Nevertheless, the designed HPTs are to be considered for applications below 1 GHz.

Therefore, we decided to use the HPTs conceived during the ORIGIN project, in particular the 10SQxEBC HPT, as their measured performances qualify them to be used as switching components in a TMA system working at 2.45 GHz.

Then, I presented the project of the packaging of the HPTs to use them as photodetectors in the RoF-TMA system prototype. This included the design and fabrication of a PCB to host the device and the design of an integrated bias-tee on the PCB. Finally, I described the final steps that need to be taken to finish the packaging of the HPT and the future set-up that will be employed to characterize the final system prototype.

Chapter 6: Conclusions and Perspectives

6.1. Conclusions

This PhD thesis aimed at the realization of an innovative low-cost system combining Radio-over-Fiber (RoF) and Time Modulated Array (TMA) technologies. The main applications foreseen for this kind of system are the coverage of in-building environments with RF signals such as 4G, 5G and WiFi, the in-door Distributed Antenna Systems (iDAS) and coverage in Local Area Networks (LANs). The proposed system exploits the high capacity, low costs, flexibility and easiness of deployment of optical fibers conjoined with the beamforming capabilities, simplicity and low costs of TMAs. While focusing on the system as a whole with a global perspective, this thesis focused in particular on the theory of TMAs and challenges related to piloting and controlling this kind of system and on the study of SiGe Heterojunction Phototransistors (HPTs) as photodetectors, thanks to their mature technology, easiness of integration and inherent high current gain.

The state-of-the-art showed the main evolution of RoF and TMA systems, focusing in particular on Vertical Cavity Surface Emitting Lasers (VCSELs) and photodetectors, such as PIN photodiodes and HPT for the RoF. While the TMA state-of-the-art focused on its multiple applications and challenges related to the system.

In chapter 3 a detailed introduction on the working principle of the TMA was given and the concept of a system combining RoF-TMA has been proposed for the first time, in particular the piloting of a TMA system with opto-electronic devices. The RoF-TMA system first prototype was then realized and characterized by measuring the radiation diagram emitted by the system. The results showed that the combined RoF-TMA works behaves as a purely electrical TMA system with deviation errors of less than 7°, thus validating the concept of a hybrid system.

It followed an analysis on the effects of unwanted phase shifts on a TMA system in general, with accurate results related to a 3-element system. This work showed that the analysis itself is challenging already for array composed of a few elements, indicating that an optimization approach is preferrable. Nevertheless, the analysis allowed to define tolerance intervals for the phase shifts for which the TMA behaviour is not compromised. In the particular case of a 3-element TMA with maximum radiation within $[-35°, 35°]$, phase shifts φ_2 and φ_3 needed to be within the intervals $[\varphi_3/2 - 37°, \varphi_3/2 + 37°]$ and $[-25.2°, 24.9°]$. Finally, an optimization program implementing the algorithm NSGA-II has been proposed as a solution to finding the TMA's modulating sequences associated to a determined and desired radiation diagram, but also to mitigate the negative effects of unwanted phase shifts. The program testing gave positive results, with possibility of improvements.

Chapter 4 focused on the RoF modelling and on the HPT in particular. A behavioural model for the laser modelling accurately the laser's non-linearities has been developed and tested in [139]. The model works at a single frequency and was presented in detail, along with simulations proving its effectiveness. Then, an analytical model of the HPT as a switching element for TMA application has been presented, defining the On-Off Ratio parameter to evaluate the HPT performance and fixing its minimum value to 5.33 dB.

In chapter 5, a design for a chip of HPTs to be tested for the RoF-TMA system was illustrated and fabricated. The HPTs on chip were characterized in frequency domain and for the first time in time domain through different set-ups. The obtained results showed that the conceived HPT were not suitable to be used as switching elements for a TMA. The transition frequencies of all the designed HPTs were below 1 GHz and the On-Off Ratio (OOR) was below 5.33 dB in the considered spectrum, while the TMA required a minimum transition frequency above 2.45 GHz. The time domain measurements showed a decrease in the output voltage gain when increasing the frequency of the input modulating wave. In addition, non linear behaviours started to appear at 10 MHz and above. Nevertheless, the DC measurements of the HPTs showed normal behaviours and a current gain β of approximately 250 for the HPT with the smallest optical window (10x10 μm^2). Therefore, the designed HPTs are to be considered for applications below 1 GHz.

It was decided that the best solution was to employ different HPTs. We chose the 10SQxEBC HPTs employed in the ORIGIN project, whose frequency characteristics are optimal for TMA applications, meaning that the OOR is above 5.33 dB at 2.45 GHz, which is our application frequency.

Finally, the packaging of the HPT was presented, consisting of a PCB with an integrated bias-tee where the HPT chip can be wire bonded and an optical fiber pigtail is glued above the optical window of the HPT. The chapter ended with the perspectives and a detailed description of the final steps for the characterization of the final RoF-TMA prototype, where the set-up and aim of the measurements is described.

In conclusion, it was demonstrated the possibility to realize a low-cost RoF-TMA system capable of distributing signals in in-building environments while ensuring a lower electromagnetic impact thanks to the beamforming provided by the TMA. The challenges related to the TMA control, such as the phase shifts and the determination of the modulating sequences, have been addressed with both an analytical and an optimization approach. Regarding the photodetector, PIN photodiodes proved to be suitable to provide the TMA modulation along with the optical-electrical conversion, with measurements to support this fact. The HPTs are suitable as well from an analytical point of view and provide an inherent current gain which is impossible to obtain with photodiodes. Unfortunately, the final prototype of the RoF-TMA system employing HPTs and VCSEL in the RoF link is yet to be realized. However, once the HPTs will be packaged on the PCBs, then all the necessary components of the system will be ready for the final measurements.

6.2. Perspectives

The perspectives of this PhD thesis project are oriented towards the following themes: the finalization and testing of the RoF-TMA prototype employing HPTs and VCSEL, the increase of the working frequencies, both the antenna frequency and the modulating sequences frequency and different application domains.

In the very next future, once the HPT packaging will be complete the final RoF-TMA prototype will be finalised and ready for testing in order to assess how the HPT perform in the double role of photodetector and TMA modulator. The implementation of VCSEL in this system is also of interest as these lasers are cheaper compared to other lasers, but provide a

better coupling and higher performances, in exchange for a lower emitted power. In the context of in-building environments, the lower power levels do not pose a problem, as the areas to cover are usually limited in space. Next, it will be necessary to study how to increase the working frequency of the system. While 2.45 GHz is a commonly employed frequency, for example in WiFi, 5G and next generation networks will also use mm waves, in the range of tens of GHz. Therefore, it is necessary to have a system capable of performing well at higher antenna frequencies. On the modulating sequences frequency side, this frequency defines also the spacing between thee harmonics radiated by a TMA. If we want to exploit at best the multiple radiated frequencies, it is necessary to have them spaced of at least the bandwidth of a single channel, which is in the order of a hundred MHz. Finally, the proposed applications of the RoF-TMA system are related to in-building coverage, but it can be adapted to different application domains, especially involving short range communication.

6.3. Acknowledgements

In this section I would like to thank all the people that supported and helped me throughout this project. First of all, thanks to my family and friends, you were always supporting me and this work is dedicated to you. Then, thanks to my supervisors Prof. Giovanni Tartarini and Prof. Jean-Marc Laheurte and co-supervisors Prof. Jean-Luc Polleux, Prof. Diego Masotti and Prof. Anne-Laure Billabert who made this project and the overall experience possible. A particular thanks to my colleague Dr. Jacopo Nanni who followed me since my Master's thesis and was always available to help me. Thanks to the ICON Photonics team and Dr. Francesco Peressutti, who formed me on the topic of opto-electronic devices and their characterizion. Thanks to Veronika Kienle, who helped me develop the set-up for the time domain measurements of HPTs during her internship at ESIEE. Thanks to Maxime Le Bigot, who helped me with the time domain measurements and in the design of the PCB for the packaging of the HPTs during the project "Tremplin de Recherche" between ESIEE and the University of Bologna. Lastly, thanks to Prof. Thierry Alves for his helpful advice in the design of the bias-tee integrated on the PCB.

6.4. Publications list

Publications list in chronological order:

1. J. Nanni, A. Giovannini et al., "Challenges Due to Rayleigh Backscattering in Radio over Fibre Links for the Square Kilometre Array Radio-Telescope," 2019 21st International Conference on Transparent Optical Networks (ICTON), 2019, pp. 1-4, doi: 10.1109/ICTON.2019.8840161.
2. J. Nanni, A. Giovannini et al., "Optimum Mitigation of distortion induced by Rayleigh Backscattering in Radio-over-Fiber links for the Square Kilometer Array Radio-Telescope," 2019 International Topical Meeting on Microwave Photonics (MWP), 2019, pp. 1-4, doi: 10.1109/MWP.2019.8892158.
3. J. Nanni, A. Giovannini et al., "Controlling Rayleigh-Backscattering-Induced Distortion in Radio Over Fiber Systems for Radioastronomic Applications," in Journal of Lightwave Technology, vol. 38, no. 19, pp. 5393-5405, 1 Oct.1, 2020, doi: 10.1109/JLT.2020.2993203.

4. A. Giovannini et al., "Modellization and Control of Spurious Frequency Generation due to Rayleigh Backscattering in Low-Frequency-Radio over Fiber Systems for Radioastronomic Application," 2020 XXXIIIrd General Assembly and Scientific Symposium of the International Union of Radio Science, 2020, pp. 1-4, doi: 10.23919/URSIGASS49373.2020.9232422.
5. J. Nanni, A. Giovannini et al., "Efficient Solution to Bimodal Propagation Effects in Low-Cost 850nm Radio over G.652-Fibre Systems," 2020 Italian Conference on Optics and Photonics (ICOP), 2020, pp. 1-4, doi: 10.1109/ICOP49690.2020.9300342.
6. A. Giovannini et al., "Beam-Steering Features of Radio-over-Fiber Systems via Antenna Array Time Modulation," 2020 International Topical Meeting on Microwave Photonics (MWP), 2020, pp. 140-143, doi: 10.23919/MWP48676.2020.9314581.
7. A. Giovannini et al., "Radio over Fiber–driven Time Modulated Array Antennas for Efficient Beamforming within In-Building Environments," 2020 European Conference on Optical Communications (ECOC), 2020, pp. 1-4, doi: 10.1109/ECOC48923.2020.9333311.
8. A. Giovannini et al., "Phase Shift Impact on the Performance of Time Modulated Antenna Arrays Driven by Radio Over Fiber," in Journal of Lightwave Technology, vol. 39, no. 24, pp. 7761-7770, 15 Dec.15, 2021, doi: 10.1109/JLT.2021.3098232.
9. J. Nanni, A. Giovannini et al., "Identification of the Optimal Value of the Dithering Tone Frequency to Mitigate Rayleigh-Backscattering-Induced Distortion in Radioastronomic Scenarios," 2021 XXXIVth General Assembly and Scientific Symposium of the International Union of Radio Science (URSI GASS), 2021, pp. 1-4, doi: 10.23919/URSIGASS51995.2021.9560222.
10. J. Nanni, A. Giovannini et al., "Optimal Configuration Mitigating Rayleigh-Backscattering-Induced Distortion in Radioastronomic Optical Fiber Systems," in Journal of Lightwave Technology, vol. 40, no. 20, pp. 6785-6795, 15 Oct.15, 2022, doi: 10.1109/JLT.2022.3187175.
11. A. Giovannini et al., "Improved Nonlinear Model Implementation for VCSEL Behavioral Modeling in Radio-Over-Fiber Links," in Journal of Lightwave Technology, vol. 40, no. 20, pp. 6778-6784, 15 Oct.15, 2022, doi: 10.1109/JLT.2022.3195048.
12. A. Giovannini, F. Peressutti, J. Nanni, J.L. Polleux, A. L. Billabert, D. Masotti, G. Tartarini, J.M. Laheurte, “Phototransistors SiGe en mode commuté pour les réseaux d’antennes à modulation temporelle (TMA)”, presentation at 2022 Journées Nationales Microondes (JNM), 7-10 June 2022, Limoges
13. A. Giovannini, F. Peressutti, J. Nanni, J.L. Polleux, A.L. Billabert, D. Masotti, G. Tartarini, J.M. Laheurte, “Phototransistors SiGe/Si pour les réseaux d’antennes commutés TMA”, poster at 2022 Journée de Club Optique Microondes (JCOM), 13 June 2022, Besançon
14. A. Giovannini, J. Nanni, F. Peressutti, A. L. Billabert, D. Masotti, J. L. Polleux, G. Tartarini, J. M. Laheurte, “Commuted Mode SiGe Phototransistors for Time Modulated Array Applications”, presentation at 2022 Italian Conference on Optics and Photonics (ICOP), 15-17 June 2022, Trento

Bibliography

[1] E. S. Kim, M. Sung, J. H. Lee, J. K. Lee, S. H. Cho and J. Kim, "Coverage Extension of Indoor 5G Network Using RoF-Based Distributed Antenna System," in *IEEE Access*, vol. 8, pp. 194992-194999, 2020, doi: 10.1109/ACCESS.2020.3033592.

[2] Y. Fan et al., "Throughput model for IEEE 802.11 distributed coordination function in radio-over-fiber-based distributed antenna systems," in *2013 12th Int. Conf. on Optical Communications and Networks (ICOCN)*, Chengdu, China, 2013, pp. 1-4, doi: 10.1109/ICOCN.2013.6617186.

[3] B. Chow, M. L. Yee, M. Sauer, A. Ng'Oma, M. C. Tseng and C. H. Yeh, "Radio-over-Fiber Distributed Antenna System for WiMAX Bullet Train Field Trial," in *2009 IEEE Mobile WiMAX Symp.*, Napa Valley, CA, USA, 2009, pp. 98-101, doi: 10.1109/MWS.2009.33.

[4] M. Matsuura, "Power-Over-Fiber for Radio-Over-Fiber-Based Distributed Antenna Systems," in *2018 Conf. on Lasers and Electro-Optics Pacific Rim (CLEO-PR)*, Hong Kong, China, 2018, pp. 1-2.

[5] J. Nanni *et al*., "Optimal Configuration Mitigating Rayleigh-Backscattering-Induced Distortion in Radioastronomic Optical Fiber Systems," in *Journal of Lightwave Technology*, vol. 40, no. 20, pp. 6785-6795, 15 Oct.15, 2022, doi: 10.1109/JLT.2022.3187175.

[6] J. Nanni *et al*., "Identification of the Optimal Value of the Dithering Tone Frequency to Mitigate Rayleigh-Backscattering-Induced Distortion in Radioastronomic Scenarios," in *2021 XXXIVth General Assembly and Scientific Symp. of the Int. Union of Radio Science (URSI GASS)*, Rome, Italy, 2021, pp. 1-4, doi: 10.23919/URSIGASS51995.2021.9560222.

[7] J. Nanni *et al*., "Efficient low-cost system for monitoring the fiber-induced delay-shift within Radio Astronomic Scenarios," in *2021 XXXIVth General Assembly and Scientific Symp. of the Int. Union of Radio Science (URSI GASS)*, Rome, Italy, 2021, pp. 1-4, doi: 10.23919/URSIGASS51995.2021.9560269.

[8] J. Nanni, E. Lenzi, F. Perini, J. Monari and G. Tartarini, "Fiber-based Microwave Interferometer monitoring the Delay of Fiber-Optic Antenna Downlinks in Radioastronomic Scenarios," in *2022 Italian Conf. on Optics and Photonics (ICOP)*, Trento, Italy, 2022, pp. 1-4, doi: 10.1109/ICOP56156.2022.9911751.

[9] A. Giovannini *et al*., "Modellization and Control of Spurious Frequency Generation due to Rayleigh Backscattering in Low-Frequency-Radio over Fiber Systems for Radioastronomic Application," in *2020 XXXIIIrd General Assembly and Scientific Symp. of the Int. Union of Radio Science (URSI GASS)*, Rome, Italy, 2020, pp. 1-4, doi: 10.23919/URSIGASS49373.2020.9232422.

[10] J. Nanni *et al*., "Controlling Rayleigh-Backscattering-Induced Distortion in Radio Over Fiber Systems for Radioastronomic Applications," in *Journal of Lightwave Technology*, vol. 38, no. 19, pp. 5393-5405, 1 Oct.1, 2020, doi: 10.1109/JLT.2020.2993203.

[11] J. Nanni *et al.*, "Efficient Solution to Bimodal Propagation Effects in Low-Cost 850nm Radio over G.652-Fibre Systems," in *2020 Italian Conf. on Optics and Photonics (ICOP)*, Parma, Italy, 2020, pp. 1-4, doi: 10.1109/ICOP49690.2020.9300342.

[12] J. Nanni *et al.*, "Challenges Due to Rayleigh Backscattering in Radio over Fibre Links for the Square Kilometre Array Radio-Telescope," in *2019 21st Int. Conf. on Transparent Optical Networks (ICTON)*, Angers, France, 2019, pp. 1-4, doi: 10.1109/ICTON.2019.8840161.
[13] J. Nanni *et al.*, "Optimum Mitigation of distortion induced by Rayleigh Backscattering in Radio-over-Fiber links for the Square Kilometer Array Radio-Telescope," in *2019 Int. Topical Meeting on Microwave Photonics (MWP)*, Ottawa, ON, Canada, 2019, pp. 1-4, doi: 10.1109/MWP.2019.8892158.
[14] D. Coelho and H. M. Salgado, "OFDM signals in WDM radio-over-fiber networks with fiber Bragg grating selection," in *2009 11th Int. Conf. on Transparent Optical Networks*, Ponta Delgada, Portugal, 2009, pp. 1-4, doi: 10.1109/ICTON.2009.5185075.
[15] Y. Zhu, X. Fang, L. Yin, F. Zhang and W. Hu, "Radio-over-Fiber Transmission Supporting 65536-QAM at 25GHz Band with High-Pass Delta-Sigma Modulation and RF fading Mitigation," in *2022 Optical Fiber Communications Conf. and Exhibition (OFC)*, San Diego, CA, USA, 2022, pp. 1-3.
[16] M. Noweir *et al.*, "Digitally Linearized Radio-Over Fiber Transmitter Architecture for Cloud Radio Access Network's Downlink," in *IEEE Transactions on Microwave Theory and Techniques*, vol. 66, no. 7, pp. 3564-3574, July 2018, doi: 10.1109/TMTT.2018.2819665.
[17] M. Bonate *et al.*, "Human RF-EMF Exposure Assessment for an indoor 5G Access Point with Beamforming Capability using Stochastic Dosimetry," in *2021 XXXIVth General Assembly and Scientific Symp. of the Int. Union of Radio Science (URSI GASS)*, Rome, Italy, 2021, pp. 1-4, doi: 10.23919/URSIGASS51995.2021.9560291.
[18] L. Chiaraviglio, A. Elzanaty and M. -S. Alouini, "Health Risks Associated With 5G Exposure: A View From the Communications Engineering Perspective," in *IEEE Open Journal of the Communications Society*, vol. 2, pp. 2131-2179, 2021, doi: 10.1109/OJCOMS.2021.3106052.
[19] A. B. Zekri, R. Ajgou, A. Chemsa and S. Ghendir, "Analysis of Outdoor to Indoor Penetration Loss for mmWave Channels," in *2020 1st Int. Conf. on Communications, Control Systems and Signal Processing (CCSSP)*, El Oued, Algeria, 2020, pp. 74-79, doi: 10.1109/CCSSP49278.2020.9151659.
[20] J. Senic *et al.*, "Challenges for 5G and Beyond," in *2022 16th European Conf. on Antennas and Propagation (EuCAP)*, Madrid, Spain, 2022, pp. 1-5, doi: 10.23919/EuCAP53622.2022.9769413.
[21] R. Zhu, Y. E. Wang, Q. Xu, Y. Liu and Y. D. Li, "Millimeter-wave to microwave MIMO relays (M4R) for 5G building penetration communications," in *2018 IEEE Radio and Wireless Symp. (RWS)*, Anaheim, CA, USA, 2018, pp. 206-208, doi: 10.1109/RWS.2018.8304988.
[22] J. S. Herd and M. D. Conway, "The Evolution to Modern Phased Array Architectures," in *Proceedings of the IEEE*, vol. 104, no. 3, pp. 519-529, March 2016, doi: 10.1109/JPROC.2015.2494879.
[23] E. L. Holzman and A. K. Agrawal, "A comparison of active phased array, corporate beamforming architectures," in *Proceedings of Int. Symp. on Phased Array Systems and Technology*, Boston, MA, USA, 1996, pp. 429-434, doi: 10.1109/PAST.1996.566131.

[24] A. K. Pandey, "Phased Array Antenna with Beamforming Network for 5G mmWave Communication System," in *2020 50th European Microwave Conf. (EuMC)*, Utrecht, Netherlands, 2021, pp. 364-367, doi: 10.23919/EuMC48046.2021.9338222.
[25] H. Shanks, "A new technique for electronic scanning," in *IRE Transactions on Antennas and Propagation*, vol. 9, no. 2, pp. 162-166, March 1961, doi: 10.1109/TAP.1961.1144965.
[26] T. Nakanishi, K. Kihira, T. Takahashi, Y. Konishi and I. Chiba, "Sideband suppression using switched phase distribution in time-modulated array antennas," in *2013 IEEE Int. Symp. on Phased Array Systems and Technology*, Waltham, MA, USA, 2013, pp. 521-528, doi: 10.1109/ARRAY.2013.6731882.
[27] O. Gassab, A. Azrar, A. Dahimene and S. Bouguerra, "Efficient Mathematical Method to Suppress Sidelobes and Sidebands in Time-Modulated Linear Arrays," in *IEEE Antennas and Wireless Propagation Letters*, vol. 18, no. 5, pp. 836-840, May 2019, doi: 10.1109/LAWP.2019.2903200.
[28] A. Tennant and B. Chambers, "Control of the harmonic radiation patterns of time-modulated antenna arrays," in *2008 IEEE Antennas and Propagation Society Int. Symp.*, San Diego, CA, USA, 2008, pp. 1-4, doi: 10.1109/APS.2008.4619900.
[29] C. Shan, J. Shi, Y. Ma, X. Sha, Y. Liu and H. Zhao, "Power Loss Suppression for Time-Modulated Arrays in Radar-Communication Integration," in *IEEE Journal of Selected Topics in Signal Processing*, vol. 15, no. 6, pp. 1365-1377, Nov. 2021, doi: 10.1109/JSTSP.2021.3118896.
[30] H. Li, Y. Chen and S. Yang, " A Time-Modulated Antenna Array With Continuous Sideband Spectrum Distribution," in *IEEE Transactions on Antennas and Propagation*, vol. 71, no. 2, pp. 1557-1567, Feb. 2023, doi: 10.1109/TAP.2022.3225259.
[31] C. He, H. Yu, X. Liang, J. Geng and R. Jin, "Sideband Radiation Level Suppression in Time-Modulated Array by Nonuniform Period Modulation," in *IEEE Antennas and Wireless Propagation Letters*, vol. 14, pp. 606-609, 2015, doi: 10.1109/LAWP.2014.2373639.
[32] Y. Chen, S. Yang, G. Li, and Z. Nie, “Adaptive nulling with time-modulated antenna arrays using a hybrid differential evolution strategy,” in *Electromagnetics*, vol. 30, no. 7, pp. 574–588, Sep. 2010.
[33] L. Poli, P. Rocca, G. Oliveri and A. Massa, "Harmonic Beamforming in Time-Modulated Linear Arrays," in *IEEE Transactions on Antennas and Propagation*, vol. 59, no. 7, pp. 2538-2545, July 2011, doi: 10.1109/TAP.2011.2152323.
[34] R. Maneiro-Catoira, J. C. Brégains, J. A. García-Naya and L. Castedo, "Enhanced Time-Modulated Arrays for Harmonic Beamforming," in *IEEE Journal of Selected Topics in Signal Processing*, vol. 11, no. 2, pp. 259-270, March 2017, doi: 10.1109/JSTSP.2016.2627178.
[35] Y. Ma, C. Miao, Y. -H. Li and W. Wu, "A Partition-Based Method for Harmonic Beamforming of Time-Modulated Planar Array," in *IEEE Transactions on Antennas and Propagation*, vol. 69, no. 4, pp. 2112-2121, April 2021, doi: 10.1109/TAP.2020.3026893.
[36] Q. Zeng et al., "Phase Modulation Technique for Harmonic Beamforming in Time-Modulated Arrays," in IEEE Transactions on Antennas and Propagation, vol. 70, no. 3, pp. 1976-1988, March 2022, doi: 10.1109/TAP.2021.3118736.

[37] R. Chen, M. Zou, X. Wang and A. Tennant, "Generation and Beam Steering of Arbitrary-Order OAM With Time-Modulated Circular Arrays," in IEEE Systems Journal, vol. 15, no. 4, pp. 5313-5320, Dec. 2021, doi: 10.1109/JSYST.2020.3019337.
[38] G. Bogdan, K. Godziszewski and Y. Yashchyshyn, "Time-Modulated Antenna Array With Beam-Steering for Low-Power Wide-Area Network Receivers," in *IEEE Antennas and Wireless Propagation Letters*, vol. 19, no. 11, pp. 1876-1880, Nov. 2020, doi: 10.1109/LAWP.2020.3007925.
[39] Tong, Y., Tennant, A., "Simultaneous control of sidelobe level and harmonic beam steering in time-modulated linear arrays" in *Electronics Letters*, vol. 46, pp. 201 – 202, 2010, doi: 10.1049/el.2010.2629.
[40] A. Tennant, "Experimental Two-Element Time-Modulated Direction Finding Array," in *IEEE Transactions on Antennas and Propagation*, vol. 58, no. 3, pp. 986-988, March 2010, doi: 10.1109/TAP.2009.2039301.
[41] C. He *et al.*, "Direction Finding by Time-Modulated Linear Array," in *IEEE Transactions on Antennas and Propagation*, vol. 66, no. 7, pp. 3642-3652, July 2018, doi: 10.1109/TAP.2018.2835164.
[42] D. Masotti, A. Costanzo, M. Del Prete and V. Rizzoli, "Time-Modulation of Linear Arrays for Real-Time Reconfigurable Wireless Power Transmission," in *IEEE Transactions on Microwave Theory and Techniques*, vol. 64, no. 2, pp. 331-342, Feb. 2016, doi: 10.1109/TMTT.2015.2512275.
[43] R. González Ayestarán, M. R. Pino, P. Nepa and B. Imaz-Lueje, "Multi-User Near-Field Focusing Through Time-Modulated Arrays," in *IEEE Transactions on Antennas and Propagation*, vol. 70, no. 5, pp. 3374-3384, May 2022, doi: 10.1109/TAP.2022.3142267.
[44] B. Clark and J. A. Flint, "A Method for Forming Distributed Beams in Time-Modulated Planar Arrays," in *IEEE Transactions on Antennas and Propagation*, vol. 66, no. 12, pp. 6958-6964, Dec. 2018, doi: 10.1109/TAP.2018.2871878.
[45] R. Marchukov, D. Masotti and A. Costanzo, "Dynamic wireless power transfer by time-modulated arrays," in *2015 IEEE Int. Symp. on Antennas and Propagation & USNC/URSI Nat. Radio Science Meeting*, Vancouver, BC, Canada, 2015, pp. 808-809, doi: 10.1109/APS.2015.7304791.
[46] F. Mani, D. Masotti and A. Costanzo, "Nonlinear Design of Time-Modulated Array for Medium Power Multisine Wireless Power Transfer," in *2019 IEEE Topical Conf. on Wireless Sensors and Sensor Networks (WiSNet)*, Orlando, FL, USA, 2019, pp. 1-4, doi: 10.1109/WISNET.2019.8711800.
[47] D. Masotti, V. Rizzoli and A. Costanzo, "On the use of time-modulated arrays for smart wireless power transmission," in *2015 Int. Conf. on Electromagnetics in Advanced Applications (ICEAA)*, Turin, Italy, 2015, pp. 549-552, doi: 10.1109/ICEAA.2015.7297176.
[48] D. Masotti, R. Marchukov, V. Rizzoli and A. Costanzo, "Far-field power transmission by exploiting time-modulation in linear arrays," in *2015 IEEE Wireless Power Transfer Conf. (WPTC)*, Boulder, CO, USA, 2015, pp. 1-4, doi: 10.1109/WPT.2015.7140156.
[49] P. Rocca, L. Poli, E. T. Bekele and A. Massa, "Time-modulation for MIMO systems — Potentials and trends," in *2012 6th European Conference on Antennas and*

Propagation (EUCAP), Prague, Czech Republic, 2012, pp. 3285-3286, doi: 10.1109/EuCAP.2012.6206055.

[50] E. T. Bekele *et al*., "Advances on time-modulated arrays for cognitive radio," in *2013 7th European Conf. on Antennas and Propagation (EuCAP)*, Gothenburg, Sweden, 2013, pp. 344-346.

[51] G. Bogdan, K. Godziszewski, Y. Yashchyshyn and S. Kozłowski, "Single RF Chain MIMO Receiver Using Beam-Steering Time Modulated Antenna Array," in *2019 13th European Conf. on Antennas and Propagation (EuCAP)*, Krakow, Poland, 2019, pp. 1-4.

[52] R. Maneiro-Catoira, J. Brégains, J. A. García-Naya and L. Castedo, "Time-modulated arrays for Digital Communications in multipath scenarios," in *2015 IEEE Int. Symp. on Antennas and Propagation & USNC/URSI Nat. Radio Science Meeting*, Vancouver, BC, Canada, 2015, pp. 816-817, doi: 10.1109/APS.2015.7304795.

[53] R. Maneiro-Catoira, J. C. Brégains, J. A. García-Naya, L. Castedo, P. Rocca and L. Poli, "Performance Analysis of Time-Modulated Arrays for the Angle Diversity Reception of Digital Linear Modulated Signals," in *IEEE Journal of Selected Topics in Signal Processing*, vol. 11, no. 2, pp. 247-258, March 2017, doi: 10.1109/JSTSP.2016.2609852.

[54] Q. Zeng, P. Yang, L. Yin, Y. Gan and F. Yang, "Performance Analysis of Time-modulated Array in Digital Communication System," in *2019 IEEE Int. Symp. on Antennas and Propagation and USNC-URSI Radio Science Meeting*, Atlanta, GA, USA, 2019, pp. 1271-1272, doi: 10.1109/APUSNCURSINRSM.2019.8888696.

[55] J. Guo, L. Poli, M. A. Hannan, P. Rocca, S. Yang and A. Massa, "Time-Modulated Arrays for Physical Layer Secure Communications: Optimization-Based Synthesis and Experimental Assessment," in *IEEE Transactions on Antennas and Propagation*, vol. 66, no. 12, pp. 6939-6949, Dec. 2018, doi: 10.1109/TAP.2018.2870381.

[56] C. He, X. Liang, B. Zhou, J. Geng and R. Jin, "Space-Division Multiple Access Based on Time-Modulated Array," in *IEEE Antennas and Wireless Propagation Letters*, vol. 14, pp. 610-613, 2015, doi: 10.1109/LAWP.2014.2373431.

[57] G. Ni, Y. Song, J. Chen, C. He and R. Jin, "Single-Channel LCMV-Based Adaptive Beamforming With Time-Modulated Array," in *IEEE Antennas and Wireless Propagation Letters*, vol. 19, no. 11, pp. 1881-1885, Nov. 2020, doi: 10.1109/LAWP.2020.2997382.

[58] P. Rocca, Q. Zhu, E. T. Bekele, S. Yang and A. Massa, "4-D Arrays as Enabling Technology for Cognitive Radio Systems," in *IEEE Transactions on Antennas and Propagation*, vol. 62, no. 3, pp. 1102-1116, March 2014, doi: 10.1109/TAP.2013.2288109.

[59] M. H. Mazheri, M. Fakharzadeh and M. Akbari, "Efficiency improvement in TMA using complementary mode switching," in *2017 IEEE Int. Symp. on Antennas and Propagation & USNC/URSI Nat. Radio Science Meeting*, San Diego, CA, USA, 2017, pp. 1601-1602, doi: 10.1109/APUSNCURSINRSM.2017.8072843.

[60] S. Yang, Y. Beng Gan, and A. Qing, “Sideband suppression in timemodulated linear arrays by the differential evolution algorithm,” in *IEEE Antennas Wireless Propag. Lett.*, vol. 1, pp. 173–175, 2002.

[61] J. Fondevila, J. C. Bregains, F. Ares, and E. Moreno, “Optimizing uniformly excited linear arrays through time modulation,” in *IEEE Antennas Wireless Propag. Lett.*, vol. 3, pp. 298–301, 2004.
[62] S. Yang, Y. Beng Gan, A. Qing, and P. Khiang Tan, “Design of a uniform amplitude time modulated linear array with optimized time sequences,” in *IEEE Trans. Antennas Propag.*, vol. 53, no. 7, pp. 2337–2339, Jul. 2005.
[63] L. Poli, P. Rocca, L. Manica, and A.Massa, “Handling sideband radiations in time-modulated arrays through particle swarm optimization,” in *IEEE Trans. Antennas Propag.*, vol. 58, no. 4, pp. 1408–1411, Apr. 2010.
[64] C. Viana, “Technological development and system integration of VCSELs and SiGe HPT receivers for 60 GHz low cost Radio-over-Fiber applications,” Ph.D. dissertation, MSTIC, Univ. Paris-Est, Champs-sur-Marne, France, 2014.
[65] Zerihun Gedeb Tegegne, “SiGe/Si Microwave Photonic Phototransistors and Interconnects towards Silicon-based full Optical Links,” Ph.D. dissertation, MSTIC, Univ. Paris-Est, Champs-sur-Marne, France, 2016.
[66] C. Viana, J. L. Polleux and C. Algani, "VCSEL characterizations at the circuit- and system-levels for low-cost RoF applications," in *2013 13th Mediterranean Microwave Symp. (MMS)*, Saida, Lebanon, 2013, pp. 1-4, doi: 10.1109/MMS.2013.6663080.
[67] C. Viana, J. L. Polleux, “Radio-over-Fibre Techniques within Home Networks. Focus on VCSELs and Photoreceivers (SiGe HPT and Commercial ROSA),” Workshop at European Microwave Week, Nuremberg, 2013.
[68] A. Bdeoui, A. L. Billabert, J. L. Polleux, C. Algani and C. Rumelhard, “Definition of Both Opto-microwave S-parameters and Noise Figures for the Elements of an IMDD Microwave Photonic Link,” in *12th Microcoll Conf.*, Budapest, 2007.
[69] C. Rumelhard, C. Algani, A. L. Billabert, “Microwave Photonics Links’ Components and Circuits,” John Wiley & Sons, ISBN 978-1-84821-226-8, 2011.
[70] J. L. Polleux, “Contribution à l’étude et à la modélisation de phototransistors bipolaires à hétérojonction SiGe/Si pour les applications opto-microondes,” Ph.D. dissertation, CNAM, Paris, Oct. 2001.
[71] J. L. Polleux, L. Paszkiewicz, A. L. Billabert, J. Salset and C. Rumelhard, "Optimization of InP-InGaAs HPT gain: design of an opto-microwave monolithic amplifier," in *IEEE Transactions on Microwave Theory and Techniques*, vol. 52, no. 3, pp. 871-881, March 2004, doi: 10.1109/TMTT.2004.823555.
[72] J. L. Polleux, F. Moutier, A. L. Billabert, C. Rumelhard, E. Sonmez and H. Schumacher, "A strained SiGe layer heterojunction bipolar phototransistor for short-range opto-microwave applications," in *MWP 2003 Proceedings. Int. Topical Meeting on Microwave Photonics*, Budapest, Hungary, 2003, pp. 113-116, doi: 10.1109/MWP.2003.1422840.
[73] J. L. Polleux, F. Moutier, A. L. Billabert, C. Rumelhard, E. Sonmez and H. Schumacher, “An Heterojunction SiGe/Si Phototransistor for Opto-Microwave Applications: Modeling and first Experimental Results,” in *GAAS Conf. of the European Microwave Week 2003*, pp.231-234, Munich, Germany, 2003.
[74] A. Bdeoui, “Etude des éléments d’une liaison optique en microonde,” Ph.D. Dissertation, CNAM, Paris, 2006.

[75] Julien Schiellein, “Etude des Phototransistors bipolaires à hétérojonction InP/InGaAs pour applications d’oscillateur photoinjectés très faible bruit de phase,” Ph.D. dissertation, MSTIC, Univ. Paris-Est, Champs-sur-Marne, France, 2012.
[76] VI Systems GmbH, “Up to 56 GBaud/s VCSEL (850nm),” in 2021, doi: 160215-Rev2.1.
[77] E. Haglund *et al.*, “30 GHz bandwidth 850 nm VCSEL with sub-100 fJ/bit energy dissipation at 25-50 Gbit/s,” in *Electronics Letters 51,* 2015, pp. 1096-1098, doi: 10.1049/el.2015.0785.
[78] S. T. M. Fryslie, M. P. T. Siriani, D. F. Siriani, M. T. Johnson and K. D. Choquette, "37-GHz Modulation via Resonance Tuning in Single-Mode Coherent Vertical-Cavity Laser Arrays," in *IEEE Photonics Technology Letters*, vol. 27, no. 4, pp. 415-418, 15 Feb.15, 2015, doi: 10.1109/LPT.2014.2376959.
[79] M. Müller, W. Hofmann, M. Horn, G. Böhm and M.C. Amann, "Low-parasitics 1.55 µm VCSELs with modulation bandwidths beyond 17 GHz," in *CLEO/QELS: 2010 Laser Science to Photonic Applications*, San Jose, CA, USA, 2010, pp. 1-2.
[80] M. Muller, W. Hofmann, G. Bohm and M. C. Amann, "Short-Cavity Long-Wavelength VCSELs With Modulation Bandwidths in Excess of 15 GHz," in *IEEE Photonics Technology Letters*, vol. 21, no. 21, pp. 1615-1617, Nov.1, 2009, doi: 10.1109/LPT.2009.2030781.
[81] Kenichi Iga, “Vertical-Cavity Surface-Emitting Laser: Its Conception and Evolution,” in *Japanese Journal of Applied Physics 47.1R (2008)*, pp. 1-10, doi: 10.1143/JJAP.47.1.
[82] H. Zimmerman, “SiGe Photodetectors. In: Silicon Optoelectronic Integrated Circuits,” in *Springer Series in Advanced Microelectronics (2018)*, doi: 10.1007/978-3-030-05822-7_4.
[83] J. Osmond, G. Isella, D. Chrastina, R. Kaufmann and H. von Kanel, "High speed Ge photodetector integrated on silicon-on-insulator operating at very low bias voltage," in *2008 5th IEEE Int. Conf. on Group IV Photonics*, 2008, pp. 164-166, doi: 10.1109/GROUP4.2008.4638132.
[84] L. Vivien *et al.*, "40Gbit/s germanium waveguide photodiode," in *2013 Optical Fiber Communication Conf. and Expo. and the Nat. Fiber Optic Engineers Conf. (OFC/NFOEC)*, 2013, pp. 1-3, doi: 10.1364/OFC.2013.OM2J.3.
[85] D. Ali, P. Thompson, J. Goldhar, J. DiPasquale and C. J. K. Richardson, "High-speed SiGe p-i-n W-structure photodetectors at telecommunication wavelengths grown directly on Si," in *2008 Conf. on Lasers and Electro-Optics and 2008 Conf. on Quantum Electronics and Laser Science*, 2008, pp. 1-2, doi: 10.1109/CLEO.2008.4551463.
[86] S. Malyshev and A. Chizh, "State of the art high-speed photodetectors for microwave photonics application," in *15th Int. Conf. on Microwaves, Radar and Wireless Communications (IEEE Cat. No.04EX824)*, 2004, pp. 765-775 Vol.3, doi: 10.1109/MIKON.2004.1358469.
[87] G. Dehlinger, S. J. Koester, J. D. Schaub, J. O. Chu, Q. C. Ouyang and A. Grill, "High-speed Germanium-on-SOI lateral PIN photodiodes," in *IEEE Photonics Technology Letters*, vol. 16, no. 11, pp. 2547-2549, Nov. 2004, doi: 10.1109/LPT.2004.835631.
[88] S. M. Csutak, J. D. Schaub, W. E. Wu, R. Shimer and J. C. Campbell, "CMOS-compatible high-speed planar silicon photodiodes fabricated on SOI substrates," in

IEEE Journal of Quantum Electronics, vol. 38, no. 2, pp. 193-196, Feb. 2002, doi: 10.1109/3.980272.

[89] M. Ghioni, F. Zappa, V. P. Kesan and J. Warnock, "A VLSI-compatible high-speed silicon photodetector for optical data link applications," in *IEEE Transactions on Electron Devices*, vol. 43, no. 7, pp. 1054-1060, July 1996, doi: 10.1109/16.502414.

[90] John Wiley and Sons, "Physics of semiconductor Devices," in 1981, doi: 10.23919/URSIRSB.2004.7909635

[91] H. Kamitsuna, T. Shibata, K. Kurishima and M. Ida, "Direct optical injection locking of InP/InGaAs HPT oscillator ICs for microwave photonics and 40-Gbit/s-class, optoelectronic clock recovery," in *IEEE Transactions on Microwave Theory and Techniques*, vol. 50, no. 12, pp. 3002-3008, Dec. 2002, doi: 10.1109/TMTT.2002.805168.

[92] P. Freeman, Xiangkun Zhang, I. Vurgaftman, J. Singh and P. Bhattacharya, "Optical control of 14 GHz MMIC oscillators based on InAlAs/InGaAs HBTs with monolithically integrated optical waveguides," in *IEEE Transactions on Electron Devices*, vol. 43, no. 3, pp. 373-379, March 1996, doi: 10.1109/16.485649.

[93] H. A. Khan and A. A. Rezazadeh, "Analytical Modeling of the Spectral Response of Heterojunction Phototransistors," in *IEEE Electron Device Letters*, vol. 30, no. 11, pp. 1158-1160, Nov. 2009, doi: 10.1109/LED.2009.2030376.

[94] S. W. Tan, H. R. Chen, W. T. Chen, M. K. Hsu, A. H. Lin and W. S. Lour, "Characterization and modeling of three-terminal heterojunction phototransistors using an InGaP layer for passivation," in *IEEE Transactions on Electron Devices*, vol. 52, no. 2, pp. 204-210, Feb. 2005, doi: 10.1109/TED.2004.842537.

[95] J. Thuret, C. Gonzalez, J. L. Benchimol, M. Riet and P. Berdaguer, "High-speed InP/InGaAs heterojunction phototransistor for millimetre-wave fibre radio communications," in *Conf. Proceedings. 11th Int. Conf. on Indium Phosphide and Related Materials (IPRM'99) (Cat. No.99CH36362)*, 1999, pp. 389-392, doi: 10.1109/ICIPRM.1999.773715.

[96] P. Kostov *et al.*, "PNP PIN bipolar phototransistors for high-speed applications built in a 180 nm CMOS process," in *Solid State Electronics 72 (2012)*, doi: 10.1016/j.sse.2012.04.011.

[97] J. L. Polleux *et al.* "An SiGe/Si Heterojunction Phototransistor for Microwave-Photonics Applications: Modeling and first Experimental Results," in *11th GAAS Symp.*, 2003, Munich, Germany.

[98] Z. G. Tegegne *et al.*, "SiGe Microwave Phototransistors for Microwave-Photonics Applications," in *2020 IEEE BiCMOS and Compound Semiconductor Integrated Circuits and Technology Symp. (BCICTS)*, 2020, pp. 1-7, doi: 10.1109/BCICTS48439.2020.9392985.

[99] Z. G. Tegegne, C. Viana, J. L. Polleux, M. Grzeskowiak and E. Richalot, "Study of Lateral Scaling Impact on the Frequency Performance of SiGe Heterojunction Bipolar Phototransistor," in *IEEE Journal of Quantum Electronics*, vol. 54, no. 3, pp. 1-9, June 2018, Art no. 4600109, doi: 10.1109/JQE.2018.2822179.

[100] J. Nanni, Z. G. Tegegne, C. Viana, G. Tartarini, C. Algani and J. L. Polleux, "SiGe Photo-Transistor for Low-Cost SSMF-Based Radio-Over-Fiber Applications at 850nm," in *IEEE Journal of Quantum Electronics*, vol. 55, no. 4, pp. 1-9, Aug. 2019, Art no. 4600109, doi: 10.1109/JQE.2019.2917209.

[101] Z. Pei *et al.*, "Bandwidth enhancement in an integratable SiGe phototransistor by removal of excess carriers," in *IEEE Electron Device Letters*, vol. 25, no. 5, pp. 286-288, May 2004, doi: 10.1109/LED.2004.826975.
[102] Z. Pei *et al.*, "Integratable SiGe phototransistor with high speed (BW=3 GHz) and extremely-high avalanche responsivity," in *Int. Semiconductor Device Research Symp.*, 2003, pp. 18-19, doi: 10.1109/ISDRS.2003.1271975.
[103] Z. Pei *et al.*, "A high-performance SiGe-Si multiple-quantum-well heterojunction phototransistor," in *IEEE Electron Device Letters*, vol. 24, no. 10, pp. 643-645, Oct. 2003, doi: 10.1109/LED.2003.817870.
[104] F. Yuan, J. W. Shi, Z. Pei and C. W. Liu, "MEXTRAM modeling of Si-SiGe HPTs," in *IEEE Transactions on Electron Devices*, vol. 51, no. 6, pp. 870-876, June 2004, doi: 10.1109/TED.2004.829622.
[105] T. Yin, A. M. Pappu and A. B. Apsel, "Low-cost, high-efficiency, and high-speed SiGe phototransistors in commercial BiCMOS," in *IEEE Photonics Technology Letters*, vol. 18, no. 1, pp. 55-57, Jan. 1, 2006, doi: 10.1109/LPT.2005.860060.
[106] H. Rucker *et al.*, "A 0.13µm SiGe BiCMOS technology featuring fT/fmax of 240/330 GHz and gate delays below 3 ps," in *2009 IEEE Bipolar/BiCMOS Circuits and Technology Meeting*, 2009, pp. 166-169, doi: 10.1109/BIPOL.2009.5314251.
[107] T. Lacave *et al.*, "Influence of the selectively implanted collector integration on +400 GHz fMAX Si/SiGe:C HBTs," in *Conf.: 4th SiGe, Ge, and Related Compounds – Materials, Processing and Devices 33 (2010)*, pp. 331-335, doi: 10.1149/1.3487563.
[108] H. Rucker and B. Heinemann, "Silicon-Germanium Heterojunction Bipolar Transistors for mm-Wave Systems: Technology, Modeling and Circuit Applications," in *River publishers (2018)*, doi: 10.13052/rp-9788793519602
[109] J. L. Polleux and C. Rumelhard, "Optical absorption coefficient determination and physical modelling of strained SiGe/Si photodetectors," in *8th IEEE Int. Symp. on High Performance Electron Devices for Microwave and Optoelectronic Applications (Cat. No.00TH8534)*, 2000, pp. 167-172, doi: 10.1109/EDMO.2000.919052.
[110] C. Rumelhard and J. L. Polleux "Model and Definitions for the Analysis of HPTs: Application to InP and SiGe Phototransistors," in *Nefertiti Workshop on Microwave Phototransistors (2003)*.
[111] A. Bennour, F. Moutier, J. L. Polleux, C. Algani and S. Mazer, "A Distributed Extended Ebers–Moll Model Topology for SiGe Heterojunction Bipolar Phototransistors Based on Drift–Diffusion Hydrodynamic Behavior," in *IEEE Transactions on Electron Devices*, vol. 64, no. 5, pp. 2267-2274, May 2017, doi: 10.1109/TED.2017.2675912.
[112] A. Bennour, J. L. Polleux, C. Algani, Z. G. Tegegne and S. Mazer, "Electrical Compact Modeling of SiGe Phototransistor: Impact of the Distributed Nature on Dynamic Behavior," in *IEEE Transactions on Electron Devices*, vol. 67, no. 3, pp. 1034-1040, March 2020, doi: 10.1109/TED.2020.2966057.ù
[113] M. H. Mazaheri, M. Fakharzadeh and M. Akbari, "Efficiency Enhancement of Time-Modulated Arrays With Optimized Switching Sequences," in *IEEE Transactions on Antennas and Propagation*, vol. 66, no. 7, pp. 3411-3420, July 2018, doi: 10.1109/TAP.2018.2829801.
[114] U. Yesilyurt, I. Kanbaz, S. Kuzu and E. Aksoy, "Harmonic Beam Steering through Dual-Phase Variable Pulse Amplitude Switching Strategy in Time Modulated Linear

Arrays," in *2019 27th Telecommunications Forum (TELFOR)*, Belgrade, Serbia, 2019, pp. 1-4, doi: 10.1109/TELFOR48224.2019.8971060.

[115] R. Maneiro-Catoira, J. Brégains, J. A. García-Naya and L. Castedo, "Time-Modulated Phased Array Controlled With Nonideal Bipolar Squared Periodic Sequences," in *IEEE Antennas and Wireless Propagation Letters*, vol. 18, no. 2, pp. 407-411, Feb. 2019, doi: 10.1109/LAWP.2019.2892657.

[116] Y. Wang, F. Lin and A. Tennant, "Increasing the energy efficiency of time-modulated reflector-arrays using double layer designs," in *2016 10th European Conf. on Antennas and Propagation (EuCAP)*, Davos, 2016, pp. 1-5, doi: 10.1109/EuCAP.2016.7481629.

[117] A. Giovannini *et al.*, "Radio over Fiber–driven Time Modulated Array Antennas for Efficient Beamforming within In-Building Environments," in *2020 European Conf. on Optical Communications (ECOC)*, Brussels, Belgium, 2020, pp. 1-4, doi: 10.1109/ECOC48923.2020.9333311.

[118] A. Giovannini *et al.*, "Beam-Steering Features of Radio-over-Fiber Systems via Antenna Array Time Modulation," in *2020 Int. Topical Meeting on Microwave Photonics (MWP)*, Matsue, Japan, 2020, pp. 140-143, doi: 10.23919/MWP48676.2020.9314581.

[119] A. Giovannini *et al.*, "Phase Shift Impact on the Performance of Time Modulated Antenna Arrays Driven by Radio Over Fiber," in *Journal of Lightwave Technology*, vol. 39, no. 24, pp. 7761-7770, 15 Dec.15, 2021, doi: 10.1109/JLT.2021.3098232.

[120] J. Fondevila, J. C. Brégains, F. Ares, and E. Moreno, “Optimizing uni-formly excited linear arrays through time modulation,” in *IEEE AntennasWireless Propag. Lett.*, vol. 3, no. 1, pp. 298–301, 2004.

[121] L. Poli, P. Rocca, G. Oliveri, and A. Massa, “Harmonic beamforming in time-modulated linear arrays through particle swarm optimization,” in *IEEE Trans. Antennas Propag.*, vol. 59, no. 7, pp. 2538–2545, Jul.2011.

[122] L. Poli, P. Rocca, L. Manica, and A. Massa, “Pattern synthesis intime-modulated linear arrays through pulse shifting,” in *IET Microw.,Antennas Propag.*, vol. 4, no. 9, pp. 1157–1164, Sep. 2010.

[123] L. Poli, D. Masotti, M. A. Hannan, A. Costanzo and P. Rocca, "Codesign of Switching Sequence and Diode Parameters for Multiple Pattern Optimization in Time-Modulated Arrays," in *IEEE Antennas and Wireless Propagation Letters*, vol. 19, no. 11, pp. 1852-1856, Nov. 2020, doi: 10.1109/LAWP.2020.3010824.

[124] Q. Zhu, S. Yang, L. Zheng, and Z. Nie, “Design of a low sidelobe timemodulated linear array with uniform amplitude and sub-sectional opti-mized time steps,” in *IEEE Trans. Antennas Propag.*, vol. 60, no. 9, pp.4436–4439, Sep. 2012

[125] J. Blank and K. Deb, "Pymoo: Multi-Objective Optimization in Python," in *IEEE Access*, vol. 8, pp. 89497-89509, 2020, doi: 10.1109/ACCESS.2020.2990567.

[126] G. Plantier, C. Bes, and T. Bosch, “Behavioral model of a self-mixing laser diode sensor,” in *IEEE J. Quantum Electron.*, vol. 41, no. 9, pp. 1157–1167, Sep. 2005.

[127] N. J. Gomes, P. P. Monteiro, and A. Gameiro, “Compensation of impairments in the radio over fiber infrastructure,” in Next Generation Wireless Communications Using Radio over Fiber. Wiley, 2012, pp. 211–245, doi: 10.1002/9781118306017.ch10.
[128] K. L. Chi *et al.*, “Single-mode 850 nm VCSELs for 54 Gbit/sec on-off keying transmission over 1km multi-mode fiber,” in *IEEE Photon. Technol. Lett.*, vol. 28, no. 12, pp. 1367–1370, Jun. 2016.
[129] J. Estaran *et al.*, “Quad 14 Gbps L-band VCSEL-based system for WDM migration of 4-lanes 56 Gbps optical data links,” in *Opt. Exp.*, vol. 20, no. 27, pp. 28524–28531, Dec. 2012.
[130] C. Crespo-Cadenas, J. Reina-Tosina, and M. J. Madero-Ayora, “Volterra behavioral model for wideband RF amplifiers,” in *IEEE Trans. Microw. Theory Techn.*, vol. 55, no. 3, pp. 449–457, Mar. 2007.
[131] A. Zhu and T. J. Brazil, “Behavioral modeling of RF power amplifiers based on pruned Volterra series,” in *IEEE Microw. Wireless Compon. Lett.*, vol. 14, no. 12, pp. 563–565, Dec. 2004.
[132] D. Mirri, G. Luculano, F. Filicori, G. Pasini, G. Vannini, and G. P. Gabriella, “A modified volterra series approach for nonlinear dynamic systems modeling,” in *IEEE Trans. Circuits Syst. I: Fundam. Theory Appl.*, vol. 49, no. 8, pp. 1118–1128, Aug. 2002.
[133] A. Zhu, J. C. Pedro, and T. J. Brazil, “Dynamic deviation reduction-based volterra behavioural modeling of RF power amplifiers,” in *IEEE Trans. Microw. Theory Techn.*, vol. 54, no. 12, pp. 4323–4332, Dec. 2006.
[134] M. Isaksson and D. Ronnow, “A Kautz-Volterra behavioral model for RF power amplifiers,” in *Proc. IEEE MTT-S Int. Microw. Symp. Dig.*, 2006, pp. 485–488.
[135] A. Zhu and T. J. Brazil, “RF power amplifier behavioral modeling using volterra expansion with laguerre functions,” in *Proc. IEEE MTT-S Int. Microw. Symp. Dig.*, 2005, pp. 963–966.
[136] H. Ku, M. D. McKinley, and J. S. Kenney, “Extraction of accurate behavioral models for power amplifiers with memory effects using two-tone measurements,” in *Proc. IEEE MTT-S Int. Microw. Symp. Dig.*, 2002, vol. 1, pp. 139–142.
[137] P. M. Cabral, J. Pedro, and N. B. Carvalho, “Modeling nonlinear memory effects on the AM/AM, AM/PM and two-tone IMD in microwave PA circuits,” in *Int. J. RF Microw. Comput.-Aided Eng.*, vol. 16, no. 1, pp. 13–23, 2006.
[138] H. Wang and P. Liu, “Behavioral models for power amplifiers using a difference-frequency dual-signal injection method,” in *Proc. PIERS*, Mar. 2010, pp. 950–953.
[139] A. Giovannini *et al.*, "Improved Nonlinear Model Implementation for VCSEL Behavioral Modeling in Radio-Over-Fiber Links," in *Journal of Lightwave Technology*, vol. 40, no. 20, pp. 6778-6784, 15 Oct.15, 2022, doi: 10.1109/JLT.2022.3195048.
[140] C. Viana, Z. G. Tegegne, J. Polleux, and C. Algani, “Flexible new optomicrowave design approach for radio-over-fiber applications: A case study of low cost 60 GHz VCSEL-based IF-RoF link,” in *IEEE Trans. Microw. Theory Techn.*, vol. 66, no. 9, pp. 4293–4305, Sep. 2018.
[141] A. J. Cann, “Improved nonlinearity model with variable knee sharpness,” in *IEEE Trans. Aerosp. Electron. Syst.*, vol. 48, no. 4, pp. 3637–3646, Oct. 2012.

[142] A. J. Cann, “Nonlinearity model with variable knee sharpness,” in *IEEE Trans. Aerosp. Electron. Syst.*, vol. AES-16, no. 6, pp. 874–877, Nov. 1980.
[143] A. Giovannini *et al.*, “Commuted Mode SiGe Phototransistors for Time Modulated Array Applications,” in *Italian Conference on Optics and Photonics (ICOP)*, Trento, Italy, 2022.
[144] A. Giovannini *et al.*, “Phototransistors SiGe en mode commuté pour les réseaux d’antennes à modulation temporelle (TMA),” in *Journées Nationales Microondes (JNM)*, Limoges, France, 2022.
[145] A. Giovannini *et al.*, “Phototransistors SiGe/Si pour les réseaux d’antennes commutés TMA,” in *Journée du Club Optique Microondes (JCOM)*, Besançon, France, 2022.

[146] J. L. Polleux, F. Moutier, A. L. Billabert, C. Rumelhard, E. Snmez, H. Schumacher, “A Strained SiGe layer Heterojunction BipolarPhototransistor for Short-Range Opto-Microwave Applications,” in *IEEE- MWP*, Budapest, Hungary, pp113-116, September 2003.
[147] J. L. Polleux, F. Moutier, A. L. Billabert, C. Rumelhard, E. Snmez, H. Schumacher, “An SiGe/Si Heterojunction Phototransistor for Opto-Microwave Applications: Modeling and first Experimental Results,” in *GAAS Conference of the European Microwave Week*, Munich, Germany, october 2003.
[148] Z. Pei *et al.*, “Bandwidth Enhancement in an Integratable SiGe Phototransistor by Removal of Excess Carriers”, in *IEEE Electron Device Letters*, Vol. 25, N5, pp286-288, May 2004.
[149] Egels, M. *et al.*: “Design of an optically frequency or phase-controlled oscillator for hybrid fiber-radio LAN at 5.2 GHz”. In *Microwave Opt. Technol. Lett.*, 45 (2) (2005), 104–107.
[150] Yin T. *et al.*: “Low-cost, high efficiency and high-speed SiGe phototransistors in commercial BiCMOS, ”in *IEEE Photonics Technol. Lett.*, 18 (1) (2006).
[151] K. S. Lai *et al*., “High-Responsivity Photodetector in Standard SiGeBiCMOS Technology, ” in *IEEE Electron Device Letters*, Vol. 28, Iss. 9, pp. 800-802, Sept. 2007.
[152] F. Peressutti, “Development of optically fed RF & millimeter-wave beamforming antennas: improving routes for the optoelectronics integration for higher frequency and compacity,” Ph.D dissertation, Univ. Gustave Eiffel, Champs-sur-Marne, France, 2021.
[153] M. D. Rosales, J. L. Polleux and C. Algani, “Design and Implementation of SiGe HPTs using an 80GHz SiGe Bipolar Process Technology,“ in *8th IEEE Int. Conf. on Group IV Photonics*, 14-16 september 2011.